

NON-PREMIXED CONDITIONS IN THE FLAMEHOLDING RECIRCULATION
REGION BEHIND A STEP IN SUPERSONIC FLOW

By

AMIT THAKUR

A DISSERTATION PRESENTED TO THE GRADUATE SCHOOL
OF THE UNIVERSITY OF FLORIDA IN PARTIAL FULFILLMENT
OF THE REQUIREMENTS FOR THE DEGREE OF
DOCTOR OF PHILOSOPHY

UNIVERSITY OF FLORIDA

2006

Copyright 2006

by

AMIT THAKUR

ACKNOWLEDGMENTS

I am grateful to my advisor, Dr. Corin Segal, for guiding me through the research work and for driving me to finish the Ph.D. program in a relatively short time. Working at the combustion laboratory helped me learn about scramjet engines, and provided valuable practical experience ranging from setting up, performing and analyzing scientific experiments to writing technical papers and delivering presentations at international conferences. Beyond academics, interaction with fellow lab mates having diverse backgrounds from different countries made for an enjoyable and educational experience in itself. Finally, I thank my mother and father for being typical Indian parents, encouraging their child to pursue higher education.

This work was performed with support from NASA grant NCC3-994, with Claudia Meyer as the Program Manager.

TABLE OF CONTENTS

	<u>page</u>
ACKNOWLEDGMENTS	iii
LIST OF TABLES	vi
LIST OF FIGURES	vii
ABSTRACT	ix
CHAPTER	
1. INTRODUCTION	1
Hypersonic Air-Breathing Vehicle	1
Air-breathing Engine Classification	2
Turbojet Engine	2
Ramjet Engine	3
Scramjet Engine	4
Flameholding in Supersonic Flow	5
Cavity Flameholder	8
Strut Flameholder	11
Free Shear Layer Fluid Dynamics	13
Flame Stability Limits	16
Flame Stability in High-Speed Subsonic Flow	16
Non-Premixed Flame Stability in Supersonic Flow	19
Species Distribution in Non-Premixed Flameholding Region in Supersonic Flow ...	23
Experiments	23
Computations	27
Mass Sampling for Species Concentration Measurement in Supersonic Flow	27
Optical Diagnostics for Species Concentration Measurement in Supersonic Flow ...	29
Planar Laser-Induced Fluorescence (PLIF)	29
Raman Scattering	33
Scope of Study	34
2. EXPERIMENTAL SETUP	39
Supersonic Wind Tunnel	39
Mass Sampling and Analysis	40
Hardware	40

Data Processing	43
Optical Diagnostics.....	44
Hardware	44
Image Acquisition and Processing	46
3. RESULTS: NON-REACTING FLOW	57
Mass Spectrometry (MS).....	57
Base Injection: Helium.....	57
Base Injection: Argon.....	59
Upstream Injection: Helium	61
Upstream Injection: Argon.....	62
Planar Laser Induced Fluorescence (PLIF).....	63
Base Injection: Helium.....	63
Base Injection: Argon.....	64
Upstream Injection	65
Comparison between MS and PLIF data	65
4. RESULTS: REACTING FLOW	78
Base Injection: Hydrogen	78
Upstream Injection: Hydrogen	80
5. CONCLUSIONS	88
APPENDIX	
A. LABVIEW PROGRAM FOR MASS SAMPLING SEQUENCING	92
B. MATLAB PROGRAM FOR PLIF IMAGE PROCESSING	99
LIST OF REFERENCES.....	109
BIOGRAPHICAL SKETCH	115

LIST OF TABLES

<u>Table</u>	<u>page</u>
2-1. Mass spectrometer calibration factors for various gases.....	50
3-1. Base fuel injection: global and local X_{He}	67
3-2. Base fuel injection: global and local X_{Ar}	67
3-3. Upstream fuel injection: global and local X_{He}	67
3-4. Upstream fuel injection: global and local X_{Ar}	67
4-1. Base fuel injection: global and local Φ_{H_2}	82

LIST OF FIGURES

<u>Figure</u>	<u>page</u>
1-1. Comparison between (a) Rocket-powered vehicle [Source: www.isro.org] and (b) Scramjet-powered hypersonic vehicle [Source: www.nasa.gov].	36
1-2. Schematic diagram of (a) turbojet engine (b) ramjet engine (c) scramjet engine.	37
1-3. Various flameholder geometries for supersonic flow: (a) rearward step (b) cavity (c) strut.	38
1-4. Schematic diagram of supersonic flow over a rearward step.....	38
2-1. Description of the test section showing fuel injection and mass sampling locations: (a) image and (b) schematic diagram.....	51
2-2. Mass sampling from the recirculation region behind the step for analysis by the mass spectrometer: (a) schematic diagram (b) image.	52
2-3. MS measurements of species mole fraction distribution in the recirculation region as the solenoid valves switch sequentially from one sampling port to another under steady experimental conditions (a) non-reacting flow with helium as the simulant fuel (b) reacting flow with hydrogen combustion.	53
2-4. Schematic diagram of planar laser-induced fluorescence (PLIF) setup.....	54
2-5. Sample PLIF image for (a) background (b) laser sheet.	55
2-6. Temporal variation of laser sheet profile at $y/H = 1.1$	56
3-1. Wall pressure distribution for non-reacting flow. $P_{0air} = 4.8$ atm, $M_{air} = 1.6$. The axial origin is placed at the step.	68
3-2. Base fuel injection: MS measurement of helium mole fraction distribution in the recirculation region for (a) wall sampling (b) inflow sampling. $P_{0air} = 4.8$ atm, $M_{air} = 1.6$	69
3-3. Base fuel injection: MS measurement of argon mole fraction distribution in the recirculation region for (a) wall sampling (b) inflow sampling. $P_{0air} = 4.8$ atm, $M_{air} = 1.6$	70

3-4. Upstream fuel injection: MS measurement of helium mole fraction distribution in the recirculation region for (a) wall sampling (b) inflow sampling. $P_{0\text{air}} = 4.8$ atm, $M_{\text{air}} = 1.6$.	71
3-5. Upstream fuel injection: MS measurement of argon mole fraction distribution in the recirculation region for (a) wall sampling (b) inflow sampling. $P_{0\text{air}} = 4.8$ atm, $M_{\text{air}} = 1.6$.	72
3-6. PLIF measurement for base injection of helium (a) image (b) X_{He} distribution (%). $P_{0\text{He}} = 5.4$ atm, $P_{0\text{air}} = 4.8$ atm, $M_{\text{air}} = 1.6$.	73
3-7. PLIF measurement for base injection of helium (a) image (b) X_{He} distribution (%). $P_{0\text{He}} = 12.0$ atm, $P_{0\text{air}} = 4.8$ atm, $M_{\text{air}} = 1.6$.	74
3-8. PLIF measurement for base injection of argon (a) image (b) X_{Ar} distribution (%). $P_{0\text{Ar}} = 5.4$ atm, $P_{0\text{air}} = 4.8$ atm, $M_{\text{air}} = 1.6$.	75
3-9. PLIF measurement for base injection of argon (a) image (b) X_{Ar} distribution (%). $P_{0\text{Ar}} = 12.0$ atm, $P_{0\text{air}} = 4.8$ atm, $M_{\text{air}} = 1.6$.	76
3-10. Comparison between MS and PLIF data for base fuel injection of (a) helium (b) argon.	77
4-1. Wall pressure distribution for hydrogen combustion tests. $P_{0\text{air}} = 4.5$ atm, $M_{\text{air}} = 1.6$.	83
4-2. Base fuel injection: Wall sampling results for (a) hydrogen equivalence ratio distribution in the recirculation region (b) combustion species mole fraction distribution. $P_{0\text{H}_2} = 4.5$ atm, $P_{0\text{air}} = 4.5$ atm, $M_{\text{air}} = 1.6$.	84
4-3. Base fuel injection: Wall sampling results for (a) hydrogen equivalence ratio distribution in the recirculation region (b) combustion species mole fraction distribution. $P_{0\text{H}_2} = 8.2$ atm, $P_{0\text{air}} = 4.5$ atm, $M_{\text{air}} = 1.6$.	85
4-4. Base fuel injection: Inflow sampling results for (a) hydrogen equivalence ratio distribution in the recirculation region (b) combustion species mole fraction distribution. $P_{0\text{H}_2} = 4.5$ atm, $P_{0\text{air}} = 4.5$ atm, $M_{\text{air}} = 1.6$.	86
4-5. Base fuel injection: Inflow sampling results for (a) hydrogen equivalence ratio distribution in the recirculation region (b) combustion species mole fraction distribution. $P_{0\text{H}_2} = 8.2$ atm, $P_{0\text{air}} = 4.5$ atm, $M_{\text{air}} = 1.6$.	87

Abstract of Dissertation Presented to the Graduate School
of the University of Florida in Partial Fulfillment of the
Requirements for the Degree of Doctor of Philosophy

NON-PREMIXED CONDITIONS IN THE FLAMEHOLDING RECIRCULATION
REGION BEHIND A STEP IN SUPERSONIC FLOW

By

Amit Thakur

May 2006

Chair: Corin Segal

Major Department: Mechanical and Aerospace Engineering

Flameholding in supersonic flow depends on local conditions in the recirculation region, and on mass transfer into and out of this region. Large gradients in local gas composition and temperature exist in the recirculation region. Hence, stability parameter correlations developed for premixed flames cannot be used to determine blowout stability limits for non-premixed flames encountered in practical devices. In the present study, mixture samples were extracted at different locations in the recirculation region and the shear layer formed behind a rearward-facing step in supersonic flow, and analyzed by mass spectrometry to determine the species concentration distribution in the region. The point-wise mass spectrometer measurements were complemented by acetone planar laser-induced fluorescence (PLIF) measurements to get a planar distribution of fuel mole fraction in the recirculation region. Non-reacting flow tests and combustion experiments were performed by varying various fuel related parameters such as injection location, injection pressure and fuel type. Fuel injection upstream of the step was not effective in

supplying enough fuel to the recirculation region and did not sustain the flame in combustion experiments. Fuel injection at the step base was effective in sustaining the flame. For base injection, the local fuel mole fraction in the recirculation region determined from experiments was an order of magnitude higher than the global fuel mole fraction based on total moles of air flowing through the test section and total fuel injected in the test section. This suggests substantial difference in flame stability curve for non-premixed conditions in the scramjet engine compared to premixed flow. For base injection, fuel remained in the recirculation region even at higher injection pressure. Due to slower diffusion rate, the heavier fuel had higher local mole fraction in the recirculation region compared to lighter fuel for a unit global fuel mole fraction injected in the test section. Hence fuel molecular weight will affect the non-premixed flame stability limits in scramjet engine; the heavier fuel will have better fuel-lean and worse fuel-rich stability limit compared to lighter fuel. This is in addition to the fact that a lighter fuel such as hydrogen has a much wider flame stability limit than a heavier fuel such as propane. The data obtained in the study can help develop a stability parameter for non-premixed flames and validate computational models.

CHAPTER 1 INTRODUCTION

Hypersonic Air-Breathing Vehicle

Hypersonic air-breathing vehicles for launching payloads in space are an area of active interest in aerospace communities around the world. Such a vehicle could be used as the first stage of a two-stage-to-orbit launch vehicle with rocket-powered second stage required to reach orbit. In an optimistic scenario, the hypersonic air-breathing vehicle could also be used as a single-stage-to-orbit launcher. The existing rocket-based launch vehicles [Figure 1-1 (a)] carry fuel and oxidizer along with them, and the latter contributes substantially to the launch vehicle total weight. The oxidizer weight can be as high as 65% of the total weight while the useful payload is only about 2-3% of the total weight. This results in high launch costs and limits frequent access to space. An airbreathing launch vehicle [Figure 1-1 (b)] that propels itself by using oxygen from the atmosphere instead of carrying it onboard would free up a substantial portion of its weight that could potentially be utilized to significantly increase the useful payload weight as a fraction of total vehicle weight and reduce launch costs.

However, there are several challenges in realizing such a hypersonic air-breathing vehicle. It will fly in the atmosphere at high Mach numbers for a much longer time than a rocket, and thus will encounter significant drag heating on its airframe. Hence the airframe should be made of materials that can withstand extremely high temperatures; it also needs to be actively cooled by cryogenic fuel circulating under the vehicle skin. The air-breathing engine required to propel the vehicle at such high speeds is a significant

challenge in itself. It is instructive to note that the maximum speed attained by an air-breathing engine powered aircraft is Mach 3.2; hence no air-breathing engine exists today for propelling an aircraft at hypersonic speeds.

Air-breathing Engine Classification

Propulsion for an air-breathing launch vehicle would involve combined-cycle engines that utilize different forms of air-breathing engines most suited for different stages of the flight envelope. The vehicle may take off from a runway like a conventional airplane using a turbo-machinery based air-breathing engine. As the flight Mach number increases in the supersonic regime and the operating limit for turbine-based engine is reached, the engine shifts to a ramjet mode of operation. At even higher flight Mach numbers approaching hypersonic speeds, the engine operation shifts to a scramjet mode.

Turbojet Engine

A schematic diagram of turbojet engine is shown in Figure 1-2 (a). Subsonic air entering the engine inlet is slowed down to low subsonic speed by a diffuser. Its stagnation pressure is increased by a compressor. Heat is added to the high pressure air by burning fuel in the combustor and its stagnation temperature is raised further. Fuel and air are mixed before ignition for uniform heat addition to the airflow; the flame in the combustor is anchored by a bluff body flameholder. The high pressure, high temperature air is expanded through the turbine; the work done on the turbine is used to drive the compressor. The air exiting the turbine still has high temperature; this thermal energy is converted to kinetic energy by accelerating the air through a converging nozzle. The net increase in momentum of air passing through the engine produces the thrust needed to propel the aircraft.

A turbojet engine can also be used to power a supersonic aircraft by a suitably modified inlet. Oblique shocks at the inlet along with the diffuser slow down supersonic airflow to subsonic speed suitable for turbojet engine operation. As the airflow speed at the inlet increases and more compression is achieved by the shock waves, less pressure rise is achieved at the compressor. Slowing down increasingly higher speed air at the inlet converts more of kinetic energy to thermal energy and makes it hotter. Increasing its temperature further by adding heat in the combustor causes air to approach the heat tolerance limit of the downstream turbine blades. Hence as supersonic speed of the aircraft increases to about Mach 2.5, the turbojet engine approaches its operational limit. A ramjet engine is suitable for higher Mach numbers.

Ramjet Engine

A ramjet engine operates only when the vehicle has been accelerated up to supersonic speed. It has a simple configuration and differs significantly from a turbine-based engine in the fact that it has no moving parts. A schematic diagram of ramjet engine is shown in Figure 1-2 (b). A series of oblique shocks at the inlet followed by a normal shock at the diffuser throat slows the air down to subsonic speed. Sufficient pressure rise is achieved by the shocks such that the need for a compressor to raise the airflow pressure and an associated turbine to drive the compressor is eliminated. Heat is added to the air flowing through the combustor at subsonic speed. The high temperature achieved due to slowing down of high-speed air helps combustion progress faster in the engine. A converging-diverging nozzle accelerates the increased enthalpy flow exiting the combustor and exhausts it out of the engine at supersonic Mach number.

Scramjet Engine

As the flight Mach number increases further in the supersonic regime to about Mach 5, the operation of a ramjet engine becomes increasingly inefficient. The stagnation enthalpy of air, comprising kinetic and thermal energy, increases with increasing Mach number. Shocking such a high energy flow down to subsonic speed converts the kinetic energy into thermal energy and substantially raises its static temperature. At such high temperatures, heat addition would only dissociate products into ions and would not add enthalpy to the flow. Also, a normal shock causes a significant stagnation pressure loss at high Mach number that is not desirable.

Due to the above mentioned constraints, the high enthalpy airflow cannot be slowed down significantly by the engine inlet and diffuser, and it enters the combustor at supersonic speed. So heat is added to the airflow as it flows through the combustor at supersonic speed, and such an engine is called a supersonic combustion ramjet or scramjet engine. A schematic diagram of the scramjet engine is shown in Figure 1-2 (c). The hypersonic Mach number airflow is slowed down to supersonic speed by oblique shocks at the inlet and then by the diffuser. An isolator is placed before the combustor to prevent interactions propagating upstream from the combustor to the inlet. In the combustor, heat is added to air flowing at supersonic Mach number. Typically, the flow speed entering the combustion chamber of a scramjet engine is about $1/2 - 1/3$ of the vehicle flight Mach number. The high enthalpy flow exiting the combustor is then accelerated out of the engine by the converging-diverging nozzle.

There are many challenges in achieving supersonic combustion in a scramjet engine^{1, 2, 3, 4, 5}. Heat needs to be added to supersonic flow in a stable and efficient manner without causing significant stagnation pressure losses in the process. Efficient fuel-air

mixing and rapid heat release is desirable so that a short combustor length with favorable thrust to drag ratio can be realized. However, the high-speed air has an extremely short residence time in the combustor, of the order of a few *ms*. Hence the fuel gets a very short time to mix efficiently with air, ignite, undergo complete combustion and add enthalpy to the incoming flow. Since the airflow entering the combustor is supersonic, the static pressure and temperature in the combustion chamber is quite low and unfavorable for rapid chemical reaction. The high-speed airflow is compressible, which has an adverse effect on the mixing process. Stagnation pressure loss due to heat addition to supersonic airflow is unavoidable.

If the airflow in the combustor is slowed down to Mach 1 due to heat addition, it results in thermal choking of the engine. In that case, the disturbances in the combustor propagate upstream and affect the air intake at the inlet. The static pressure in the combustor increases significantly and can even lead to blowing up of the engine. Hence particular care should be taken to avoid thermal choking. This can be achieved by having a diverging cross-section in downstream part of the combustor, and by limiting the fuel supply to an acceptable threshold.

The scramjet engine has a lower pressure rise of air entering the inlet, less efficient heat addition in the combustor, and higher stagnation pressure losses compared to a turbojet engine. Hence it has a lower thrust to weight ratio than turbojet engine. To overcome this limitation, bigger scramjet engines are required on a hypersonic aircraft. This increases the total weight of the aircraft.

Flameholding in Supersonic Flow

Flameholding is an important area of concern in a scramjet engine. A parameter relevant to flameholding is the Damkohler number (*Da*) and is defined as the ratio of

flow residence time in the combustor and the fuel reaction time; the reaction time is the time it takes for fuel-air mixture to mix, ignite and release heat by chemical reaction.

$$Da = \frac{\tau_{residence}}{\tau_{reaction}} \quad (1-1)$$

Flameholding is possible only when the residence time available is more than the fuel reaction time ($Da > 1$). As mentioned earlier, the flow has a very short residence time in the combustion chamber and is of the order of only a few *ms*. In comparison, the chemical reaction time scales for hydrogen are similar to the scramjet combustor flow residence time scales, while the chemical reaction time scales for hydrocarbons are much higher; hence not enough time is available for flameholding in a supersonic combustor. The short residence time of the flow needs to be increased; hence a solution is to create a slower, subsonic recirculation region in part of the flow. Flow speed in this region is favorable to anchoring the flame, and the recirculation flow in this region serves to mix fuel and air together. The static temperature rise in the recirculation region due to slowing down of high enthalpy flow reduces the chemical reaction time scale. Hence $Da > 1$ in the flameholding recirculation region. The flameholding region thus formed serves as a reservoir of hot pool of radicals that sustains the flame in the scramjet combustor, and also as a supplier of radicals helping to propagate combustion in the main supersonic flow.

The flameholding region discussed above can be created in various ways. In turbojet engines, a bluff body placed in the combustor main flow is used as a flameholder. Such an approach is not appropriate in a scramjet combustor since the bluff body would cause significant stagnation pressure losses in supersonic flow. Various flameholding geometries suitable for supersonic flow are shown in Figure 1-3. One way

of anchoring the flame in a scramjet engine is to create a recess in the combustor wall in the form of a rearward step [Figure 1-3 (a)] or a cavity [Figure 1-3 (b)]. A subsonic recirculation region forms behind the step or in the cavity and acts as the flame anchor. The main advantage of recess flameholders is that they do not physically obstruct the supersonic flow and hence avoid stagnation pressure loss. However, they create a very hot region at the combustor wall that needs active cooling. Since recess flameholders are located at the wall, they may not be able to extend the heat release deep into the main airflow thus resulting in heat addition only to part of the airflow. Another flameholder is a slender strut placed in the main flow [Figure 1-3 (c)] and with an appropriate geometry designed to minimize stagnation pressure losses. The flow separates behind the strut and forms a recirculation region at the base that anchors the flame. The oblique shocks generated by the presence of the strut in supersonic flow raise the flow static pressure and temperature thus assisting in flameholding. However, a drawback is that the strut experiences very high temperatures since it physically obstructs the high enthalpy supersonic flow, and hence needs to be actively cooled.

All the geometries discussed above have a common flameholding mechanism, which is described for a rearward step in Figure 1-4. The approaching boundary layer of the main airflow separates at the step and forms a shear layer between the supersonic flow and the subsonic recirculation region. The shear layer is pushed towards the wall due to the supersonic flow expansion at the step base. An oblique shock is formed at the shear layer reattachment point. The mass flow rate of air supplied from the main flow into the recirculation region is governed by the shear layer, as is the supply of hot combustion radicals from the recirculation region out into the main flow. Fuel is usually

injected in the recirculation region where it mixes with the ambient air through the shear layer formed at the fuel jet. The flow pattern behind the step is complex in nature with smaller recirculation zones formed at the corners besides the primary recirculation region. Further, the figure depicts only the 2-D flow pattern; secondary recirculation regions exist at the side walls and the flow pattern is 3-D in nature. Hence combustion occurring in the flameholding region is non-premixed in nature.

Cavity Flameholder

Ben-Yakar and Hanson⁶ reviewed the flow field characteristics of supersonic flow over a cavity. Based on the L / D ratio of the cavity, the flow can be characterized as open or closed. Flow over cavity with $L / D < 7-10$ is characterized as open flow; the free shear layer separated at the cavity front wall reattaches at the back wall. For small aspect ratio cavity with $L / D < 2-3$, transverse acoustic waves oscillate along the cavity depth. For larger aspect ratio cavity, the waves oscillate along the cavity length. Cavity flow with $L / D > 10-13$ is characterized as closed flow; the free shear layer reattaches at the cavity floor. Closed flow cavity experiences much higher drag than open flow cavity, the drag force increases with increasing L / D ratio. The flow residence time in a cavity increases with cavity depth and the mass entrainment rate increases with cavity length.

The longitudinal oscillations in the cavity are caused due to shear layer impingement on the back wall. This unsteadiness in flow field is attractive for promoting fuel-air mixing; however it is undesirable for flameholding. The oscillations can be passively controlled by angled back wall that prevents reflected acoustic waves. Active flow control over the cavity can be achieved by upstream injection to enhance the shear layer growth rate and alter its instability characteristics.

Gruber et al.⁷ experimentally and computationally evaluated the flow field properties of various cavity geometries in supersonic flow. Reducing the back wall angle, defined with respect to horizontal, increased the drag coefficient and shortened the flow residence time within the cavity. The increase in drag is due to higher pressures acting over a larger fraction of back wall area. The reduction in residence time is explained by the structure of recirculating flow within the cavity. Simulations showed that a primary recirculation region and a secondary embedded vortex exist within the cavity. As the back wall angle is reduced, the primary recirculation region increases in size and the secondary recirculation zone is diminished. For such a cavity, the mass exchange takes place between the primary recirculation zone and the high speed mainstream flow. For a cavity with higher back wall angle, the mass exchange is slower since part of the exchange takes place between the low speed recirculation regions. Hence the residence time reduces with reducing the cavity back wall angle due to higher mass exchange rate.

Ali and Kurian⁸ used fuel injection into a cavity in supersonic flow as an active control mechanism for enhancing the air entrainment rate into the cavity due to interaction between the fuel jet and free shear layer. Fuel injected at different locations from the cavity floor and front/back wall increased the cavity pressure for all cases. The pressure fluctuations were suppressed for some of the fuel injection locations.

Mathur et al.⁹ performed supersonic combustion experiments with cavity flameholder; fuel was injected upstream of the cavity and from the cavity floor. The freestream conditions were varied to simulate different stages of hypersonic flight, and fuel was injected over a range of equivalence ratios. Stable flame anchored in the cavity

and extending out into the main airflow was observed for all experimental conditions. The engine thrust increased with increasing fuel equivalence ratio.

Yu et al.¹⁰ performed supersonic combustion experiments with various cavity flameholder geometries. Cavity length, back wall angle were varied and cavities in tandem were used. All cases showed a substantial increase in combustor pressure and temperature in comparison to the baseline case without cavity. This suggests enhanced volumetric heat release in the combustor aided by the presence of cavities. Some cavity configurations such as the inclined cavity and the one with two cavities in tandem showed a better performance in comparison with other configurations.

Yu et al.¹¹ performed supersonic combustion experiments with cavity flameholder; kerosene was injected upstream of the cavity and piloted by hydrogen. Barbotaged atomization of liquid kerosene using hydrogen increased the combustion efficiency substantially compared to pure liquid atomization. The combustion efficiency for fuel injection perpendicular to the airflow was higher than angled injection due to deeper penetration into the airflow; however it was achieved at the cost of higher stagnation pressure loss. Combustion performance improved with increasing cavity depth, which increased the flow residence time, but did not vary much with further increase beyond a certain depth. Tandem cavities performed better than a single cavity.

Owens et al.¹² performed supersonic combustion experiments to examine the flame stability characteristics of cavity flameholder. Kerosene was injected upstream in the flow boundary layer and piloted by hydrogen injected in the cavity. Temperature measurements in the recirculation region indicated that cavities were regions of rich mixtures and their flame stability was strongly affected by air stagnation temperature via

changes in the local equivalence ratio. At high air stagnation temperature, rich mixtures existed in the cavity and injection of kerosene resulted in flame extinction, except for large hydrogen flow rates that enlarged the recirculation region and entrained additional air from the main flow. At low air stagnation temperature, the flame held even for large kerosene flow rates.

Davis and Bowersox¹³ accessed flameholding properties of cavity in supersonic flow using a simplified, perfectly stirred reactor analysis. Self-ignition of hydrogen was achieved at a lower temperature than hydrocarbons; hydrogen had shorter ignition delay time than hydrocarbons at the same temperature. Heat loss from the cavity reduced the flammability limits. Once the lower residence time t_r is calculated using the model, the cavity depth D required for flameholding can be estimated as $D = t_r U / 40$, where U is the main airflow velocity.

Strut Flameholder

Brandstetter et al.¹⁴ established flameholding in supersonic flow in the recirculation region between a strut and a cylinder placed downstream of the strut. The cylinder surface temperature needed to be above a threshold temperature for flameholding to be sustained after the ignition source was switched off.

Northam et al.¹⁵ evaluated the performance of various strut geometries in supersonic flow. The strut incorporating the deepest step with perpendicular fuel injection downstream of the step exhibited the best combustion efficiency. The strut configuration with staged perpendicular fuel injection exhibited the lowest auto-ignition and flameholding limit. Hence an optimum strut configuration should incorporate a deep step with staged perpendicular fuel injection for best mixing and flameholding performance.

Lyubar et al.¹⁶ decelerated a small fraction of supersonic airflow in a scramjet combustor to subsonic conditions to provide a stable ignition and flameholding zone. This was achieved by an injector with its inner surface shaped like a supersonic diffuser, combustor and nozzle. Hydrogen was injected perpendicular to the decelerated airflow in the injector and the main airflow. The strong temperature rise caused due to deceleration of the airflow in the injector resulted in auto-ignition and a sustained supply of radicals to the main airflow. The normal shock causing auto-ignition in the injector was prevented from moving upstream during combustion by providing an orifice to allow for pressure release from inside the injector to the main airflow. The mass flow from the orifice also enhanced fuel-air mixing in the main airflow.

Gerlinger and Bruggermann¹⁷ performed numerical simulations for strut flameholder in supersonic flow with hydrogen injected in the flow direction at the base of the strut; the effect of varying the lip thickness at the injector end was investigated. The mixing efficiency was nearly independent of lip thickness variation. Changes caused within the shock wave/expansion pattern at the injector exit due to lip thickness variation had a moderate influence on the stagnation pressure loss.

Tabejamaat et al.¹⁸ performed numerical simulations and experiments to investigate the effect of geometry variation of a strut in supersonic flow. Hydrogen was injected parallel to the airflow and into the recirculation region formed at the base of the strut. Increasing the base height increased the recirculation region size, improved the mixing efficiency and hence increased the maximum combustion temperature in the recirculation region. Increasing the slit width of injector exit increased the recirculation region size, but did not appreciably affect the mixing efficiency and maximum

combustion temperature in the recirculation region. The double slit injection changed the flow field compared to single slit injection; increasing the distance between the two slits beyond a certain limit changed the flow field substantially and caused flame extinction.

Gruenig et al.^{19, 20} performed experiments to investigate flame stabilization and mixing by pylons in supersonic flow. Pylons can be considered as short-length struts. Mixing efficiency and combustion performance of various pylon geometries were investigated. The best combustion performance was exhibited by the pylon with fuel injected inclined to the airflow and through ramps designed to create stream-wise vortices that promote mixing. Flame stabilization was achieved by oblique shocks generated by the pylon; the shocks increased the flow temperature and pressure and caused auto-ignition of fuel-air mixture after they had mixed downstream of the pylon. A wedge appropriately positioned downstream of the pylon was used to modify the shock structure and induce auto-ignition at a shorter combustor length. The shock train was in turn influenced and pushed upstream by heat release in the combustor.

Oblique shocks are often formed within a scramjet combustor. Huh and Driscoll²¹ investigated the beneficial effects of shock waves on a supersonic jet flame. Shock waves optimally positioned with respect to the jet flame altered the flame size and significantly improved the blowout limits. The shock waves enhance mixing by directing the airflow radially inwards towards the fuel and thus increase the air entrainment rate. They create an adverse pressure gradient which increases the recirculation region size. They also improve the chemical reaction rates by increasing the static temperature and pressure.

Free Shear Layer Fluid Dynamics

The free shear layer plays a crucial role in bringing air from the main flow into the flameholding recirculation region and in transporting combustion radicals out of the

recirculation region into the main airflow. Hence the free shear layer fluid dynamics is discussed here. Dimotakis²² reviewed experimental data on turbulent free shear layer growth, mixing and chemical reactions formed between two uniform gas streams. The local Reynolds number is given by

$$\begin{aligned} \text{Re} &= \delta \Delta U / \nu > 10^4 \\ \Delta U &= U_1 - U_2 \end{aligned} \quad (1-2)$$

where U_1, U_2 are the velocities of the two streams.

The chemical product formation at a station x can be expressed as

$$\delta_p / x = (\delta / x) * (\delta_m / \delta) * (\delta_p / \delta_m) \quad (1-3)$$

where the first factor measures the shear layer growth, the second shows mixing within the shear layer, and the third indicates the chemical products formed within the molecularly mixed layer.

Shear layer growth: It depends on several flow parameters like velocity ratio (r), density ratio (s), convective Mach numbers of the two streams (M_{c1}, M_{c2}), relative mean density reduction attributed to heat release for combusting flow (q), and pressure gradient.

$$\begin{aligned} r &= U_2 / U_1 \\ s &= \rho_2 / \rho_1 \\ M_{c1} &= (U_1 - U_c) / a_1, M_{c2} = (U_c - U_2) / a_2 \\ q &= (\rho_0 - \bar{\rho}) / \rho_0 \end{aligned} \quad (1-4)$$

where U_c is the velocity of the large-scale turbulent structures in the shear layer. The incompressible shear layer growth rate increases with an increase in density ratio. The incompressible shear layer growth rate as a function of velocity and density ratio is expressed as follows.

$$\frac{\delta}{x}(r, s) = C_\delta \frac{(1-r)(1+s^{1/2})}{2(1+s^{1/2}r)} \left[1 - \frac{(1-s^{1/2})/(1+s^{1/2})}{1+2.9(1+r)/(1-r)} \right] \quad (1-5)$$

Compressibility has an adverse effect on shear layer growth. For compressible flow, the growth rate decreases with increasing convective Mach number as shown in the relation below.

$$\frac{\frac{\delta}{x}[r, s; M_{c1}]}{\frac{\delta}{x}[r, s; M_{c1} = 0]} = f(M_{c1}) = (1 - f_\infty)e^{-3M_{c1}^2} + f_\infty \quad (1-6)$$

$$f_\infty = 0.2$$

Heat release in subsonic flow results in a moderate decrease in shear layer growth. The outward displacement velocity due to heat release impedes the entrainment process and offsets the dilatation effect. The density reduction approaches a limiting value with higher heat release due a substantially unmixed fluid at high Reynolds number. Pressure gradient results in an increase or decrease in shear layer growth depending on velocity and density ratio.

Mixing: Enhanced mixing of the two free streams is obtained when shear layer instability causes a transition from large, two-dimensional vortices to three dimensional, fully developed, turbulent flow in the shear layer. However, at high Reynolds numbers, a substantial fraction of fluid in the shear layer is not molecularly mixed.

The shear layer entrains fluid from the two free streams in an asymmetric way. The molar entrainment ratio E_n for compressible shear layer is expressed as follows.

$$E_n = \frac{M_2}{M_1} \left[1 + C_l \frac{1-r}{1+r} f(M_{c1}) \right] \left(\frac{1}{s^{1/2}} \right) \quad (1-7)$$

$$C_l = 0.68$$

where M_1, M_2 are molecular weights of the two streams.

The probability density function (PDF) of concentration measurements across the width of a shear layer shows that away from the boundaries of the two free streams, the high-speed fluid fraction distribution in the mixed shear layer tends to a most probable value of ξ_E defined as follows.

$$\xi_E = \frac{E_n}{E_n + 1} \quad (1-8)$$

Pitz and Daily²³ made 3-D velocity measurements in the free shear layer formed behind a rearward step in subsonic flow. The shear layer growth rate was higher compared to other measurements for parallel streams; this was attributed to reverse flow in the recirculation region behind the step. The shear layer growth rate was same for non-reacting and reacting flow.

Flame Stability Limits

Flame Stability in High-Speed Subsonic Flow

Ozawa²⁴ compiled experimental results on wake stabilized flames in high-speed combustion systems. The limitation of the compiled results is that they are applicable to premixed, subsonic flows while the combustion process inside a scramjet engine is non-premixed and supersonic.

A bluff body placed in a combustion chamber stabilizes the flame in its wake. They are axisymmetric in shape (cone, hemisphere, disc) and also two-dimensional (V-gutter, cylinder, flat plate) with varying degree of bluffness. Flame stabilization depends on aerodynamics of the flow in the wake of the flameholder. The mass entrainment rate from the main flow into the recirculation region formed behind the body increases and the flow residence time in the region decreases with an increase in the degree of bluffness. However, a compromise has to be made between improved flameholding characteristics

and higher pressure losses of a more bluff body. A 2-D body has a higher mass entrainment rate in its wake and a longer residence time than a corresponding axisymmetric body, and hence has a better flameholding performance. Combustion reduces the mass exchange rate and increases the residence time in the recirculation region.

Various parameters of the inlet flow affect the flame blowout velocity: pressure, temperature, turbulence, water vapor contamination. An increase in inlet flow pressure and temperature has a favorable effect on the blowout velocity, with temperature having a stronger influence. Higher free-stream turbulence intensity increases the mass exchange rate behind the flameholder and the resulting quenching effect decreases the blowout velocity. Higher water vapor content of the inlet flow increases the ignition delay time of the fuel and hence decreases the blowout velocity. A stability parameter was formulated consisting of inlet flow velocity, pressure, temperature, and the flameholder type. The flameholder parameter is the maximum width of the recirculation region formed behind it. A plot of equivalence ratio vs. stability parameter gives the flame stability curve for a given fuel. The correlation between stability parameter (SP) and equivalence ratio is shown below.

$$SP = \left(\frac{T_0}{300K}\right)^{1.5} \left(\frac{P}{1atm}\right) \left(\frac{d}{U}\right) \left(\frac{d_0}{d}\right) = f(\phi) \quad (1-9)$$

where ϕ : premixed equivalence ratio

T_0 : free stream stagnation temperature

P : free stream static pressure

U : free stream velocity

d_0 / d : flameholder shape parameter

The mixing intensity in the recirculation region behind 2-D flameholders is about 30% higher than axisymmetric flameholders. However, the highest mixing intensity achieved in stirred reactors is two to three times higher than bluff body flameholders.

Huellmantel et al.²⁵ performed experiments for stabilizing premixed, subsonic, propane-air flames using a cavity recess in the combustor wall as the flameholder. Flameholding performances of various cavity geometries were studied. The flame stabilization curve was generated for each cavity by obtaining the flow velocity at which flame blow out occurred as a function of both fuel-lean and fuel-rich equivalence ratios. A long cavity had a wider flame stability range than a short cavity, and a deep cavity performed better than a shallow cavity. It indicates the necessity of having sufficient recirculation volume for achieving good stability and shows that increasing the size of the flameholder increases its performance. The degree of slope of the downstream end of the cavity did not affect flame stabilization appreciably.

The cavity flameholder had a superior blowout performance when compared to a 90° V-gutter, which is a standard bluff body flameholder. Also, the cavity caused much less pressure loss in the main flow since it did not physically obstruct the flow. However, a cause for concern in using a cavity flameholder is the excessive heating of engine wall in its vicinity.

Baxter and Lefebvre²⁶ determined the fuel-lean flame blowout limits for high-speed subsonic afterburner combustor systems by varying a range of parameters such as the V-shaped flameholder geometry, injector-flameholder spacing, airflow Mach number and stagnation temperature. The effects of changing some of these parameters were at variance with homogenous results²⁷. The heterogeneous flame blowout equivalence ratios

were leaner than the homogenous values due to richer local fuel-concentration in the flameholding region. An approximate analysis was developed to model heterogeneous effects such as transport and vaporization of liquid fuel droplets from the injection location to the flameholder, droplet capture and vaporization at the flameholder surface, and gas entrainment into the recirculation region. The effective equivalence ratio in the recirculation region determined from the above analysis and the lean blowout equivalence ratio for homogenous flame obtained from correlation of experimental data²⁷ were in good agreement with each other.

Non-Premixed Flame Stability in Supersonic Flow

Niioka et al.²⁸ performed flame stabilization tests in supersonic flow using a strut divided stream-wise into two parts, with hydrogen injected in the spacing between them. For different spacing distances between the strut components (L), flame stability plots were generated by determining the blowout fuel flow rates as a function of airflow stagnation temperature. The flameholding performance of the strut system was found to depend greatly on the distance L . The shock/expansion waves formed around to the struts were not observed to vary much with variation in L . Hence the variation in flameholding performance was due to the competition between flow residence time and chemical reaction time in the recirculation region formed in the intermediate region between the parts. For short and long distances L , the recirculation region was too fuel rich and fuel lean respectively resulting in large reaction times ($Da = \tau_{\text{residence}} / \tau_{\text{reaction}} < 1$), and hence did not give good flame stability. For moderate distances L , air entrainment from supersonic airflow into the recirculation region was adequate and reasonably well mixed.

The reaction time was less than residence time ($Da > 1$), hence flame stability was achieved.

Zakkay et al.²⁹ measured the residence time of a gas introduced in the recirculation region behind an axisymmetric body in supersonic flow for various experimental conditions. The molar concentration of the gas in the recirculation region decayed exponentially with time. The dissipation of gas from the recirculation region was due to diffusion process. The residence time in the recirculation region was of the order of a few *ms* and $t U / D \sim 75$ for laminar and 40 for turbulent flow, where t - residence time in the recirculation region, U – freestream velocity, D – bluff body base diameter. The residence time is lower for turbulent flow than laminar flow due to higher diffusion rate for turbulent flow compared to laminar flow. The residence time was independent of the concentration of gas in the recirculation region; higher concentration gas dissipated faster than lower concentration gas thus resulting in the same residence time for both cases.

Driscoll and Rasmussen³⁰ performed an analysis to develop a correlation for non-premixed flame stability limits in supersonic flow. The analysis is based on the idea that the flame base is sustained in the shear layer and not in the recirculation region. Flame propagation speed along the stoichiometric contour in the shear layer is matched by the velocity of the incoming gas. Hot products in the recirculation zone preheat the shear layer gases and increase the flame propagation speed. Flame blowout is governed by the imbalance between flame propagation speed and gas velocity. Some additional parameters governing blowout appeared in the non-premixed flame correlation compared to the premixed flame correlation: fuel injection location relative to the recirculation

region, fuel injection temperature, and stoichiometric fuel mixture fraction. Also, a global equivalence ratio appeared in the correlation that is different from the local equivalence ratio in the flameholding recirculation region. The correlation was applied to previously measured data covering supersonic and subsonic flows; cavities, bluff bodies and struts as flameholders; hydrogen, ethylene, methane and propane as fuels; and had an average uncertainty of 55%.

Rasmussen et al.³¹ examined the stability of hydrocarbon flames in supersonic flow using cavity flameholders. The effect of the different parameters on lean and rich flame blowout limits was investigated: fuel type (ethylene, methane), cavity geometry (rectangular, aft wall ramp cavity), fuel injection location (cavity floor, cavity aft wall), and airflow Mach number. The blowout limits showed strong dependence on fuel injection location. For lean blowout limit, the aft wall ramp injection performed better than floor injection. This is because ramp injection puts fuel directly into the main recirculation region formed in the cavity, and hence gets distributed throughout the cavity. Whereas floor injection puts fuel only in the shear layer, hence fuel is unable to reach much of the cavity. For rich blowout limit, the floor injection performed better than aft wall ramp injection. The reason is the same as explained above. For floor injection much of fuel bypasses the cavity and remains concentrated in the shear layer, while ramp injection floods the cavity with fuel by injecting directly into the recirculation region. Hence the fuel injection location relative to the recirculation region is an important parameter in determining flame stability limits. Ethylene had better flame stability than methane for lean as well as rich limits, since it has a much shorter ignition delay time and faster flame propagation speed. The airflow Mach number had little effect on lean

stability limit, however Mach 2 flow showed better flame stability than Mach 3 flow for rich limit. Increase in Mach number reduces the flow pressure, temperature and time scale, and its effect on flame stability can be better understood by computer simulation.

Winterfeld³² performed flame blowout experiments in supersonic flow using a contoured cylindrical flameholder and a cone-cylinder flameholder. A recirculation region formed behind the flameholder. Hydrogen was injected into the recirculation zone at different angles relative to the airflow (θ). The measured recirculation region size was bigger for $\theta = 0^\circ$ fuel injection angle than for $\theta = 90^\circ$. This is because more fuel was injected directly into the recirculation region for $\theta = 0^\circ$ while part of the fuel was blown into the supersonic airflow for $\theta = 90^\circ$. The flame blowout curve plotting normalized fuel flow rate as a function of blowout airflow Mach number was also sensitive to the fuel injection angle. For fuel rich limit, better flame stability was achieved for higher injection angles. It is again explained by the fact that fuel injection at low angle θ floods the recirculation with fuel, while at high angle θ part of fuel escapes into the supersonic airflow.

Rasmussen et al.³³ investigated the effect of fuel injection pressure on flame location within a cavity in supersonic flow. Fuel was injected from the cavity floor and from the cavity aft wall; the flame chemiluminescence was captured using a digital camera. For moderate fuel flow rates with both injection locations, the flame was anchored in the shear layer and also extended to the recirculation region. For lean and rich blowout with floor injection, the flame structure was similar to the moderate fueling case. For lean and rich blowout with aft wall injection, the flame structure showed a marked departure from moderate fueling case; the flame was not anchored in the shear

layer and was restricted to a region close to the aft wall. The change in flame stabilization mechanism for aft injection may be attributed to a change in the cavity flow field with heat release.

Species Distribution in Non-Premixed Flameholding Region in Supersonic Flow

Experiments

Hsu et al.³⁴ used Raman scattering to make fuel distribution measurements inside a cavity in Mach 2 non-reacting flow. Ethylene was injected at a low angle upstream of the cavity. The effect of fuel injection pressure, cavity size, and imposed back-pressure on fuel transport in the cavity was studied. Fuel-rich pockets were observed in the cavity. For upstream fuel injection, mass transport through the shear layer and its interaction with the cavity aft wall controls the amount of fuel entering into the cavity. The amount of fuel entering the cavity decreased as the fuel pressure was increased from moderate to high values. Higher fuel injection pressure with an increased jet momentum penetrates into the main airflow and less fuel gets entrained into the shear layer and reaches the cavity. An increase in cavity size captured more fuel at the cavity back wall, but the drag penalty also increased. Increase in back pressure, which simulates combustion conditions, caused the boundary layer upstream of the cavity to separate thus changing the shear layer interaction with the cavity. The fuel jet penetrated into the main flow due to reduced momentum of the boundary layer and less of it reached the cavity.

As a follow up of the experiments described above, Gruber et al.³⁵ examined the effect of fuel injection location, fuel flow rate, and induced back-pressure on the cavity flameholder performance in supersonic flow. NO-PLIF was used to visualize fuel distribution in the cavity for non-reacting flow, and OH-PLIF was used in combustion experiments. From non-reacting flow PLIF visualizations, it was concluded that upstream

fuel injection with passive entrainment of fuel from main airflow into the cavity is less desirable than direct fuel injection into the cavity. Unlike upstream fuel injection, direct injection from the cavity aft ramp into the main recirculation region provided a spatially uniform fuel-air mixture in the cavity. Also, the cavity fuel distribution for direct injection remained relatively insensitive to changes in the main airflow as simulated by induced back-pressure. In combustion experiments, as the fuel flow rate from cavity aft ramp was increased, the cavity was flooded with fuel and adversely affected combustion in the region. However, when a shock train was imposed for the high fuel flow rate, it significantly improved cavity combustion by causing the cavity shear layer to separate which effectively increased air entrainment in the cavity. The shock train could also enhance fuel-air mixing in the cavity.

Uchiumi et al.³⁶ followed up on the investigation by Niioka et al.²⁸ discussed earlier and conducted experiments to improve the flameholding performance of a strut divided into two parts in supersonic flow. Previous non-reacting flow measurements of local equivalence ratio along the distance between the strut parts showed that for short distance L , the intervening region was largely fuel rich in composition. Such a mixture required a long chemical reaction time compared to the short residence time available, and hence flameholding could not be established. As the distance L was increased, the measured local equivalence ratios were reduced since more air from the main flow was entrained into the recirculation region. However, for a certain range of moderate distance L , the chemical reaction time was more than the flow residence time and hence flameholding could not be established. Modifications in the fuel-injecting strut were made in the present experiment. For short distance L between the struts, slits incorporated in the

injection strut brought air from main flow into the recirculation region and diluted its fuel rich composition. For moderate distance L , a recess was provided around the fuel injector to prevent excess air from entering the intervening space. The strut modifications resulted in $Da > 1$ and hence flameholding was established in both cases.

Zamma et al.³⁷ measured pressure and gas composition for non-reacting supersonic flow over a step with fuel injected downstream of the step and transverse to the airflow. Species in the recirculation region behind the step were extracted at the wall and analyzed by gas chromatography. Fuel was entrained from the jet into the recirculation region behind the step. The fuel volume fraction in the recirculation region decreased with increasing fuel-air dynamic pressure ratio. Higher fuel volume fraction was observed in the recirculation region for lighter fuel compared to heavier fuel injected at the same dynamic pressure ratio. The gas composition measurements were used to estimate the ignition characteristics of the flameholder^{38, 39}.

Thayer and Corlett⁴⁰ measured pressure, temperature and gas composition in the separated recirculation region upstream of a fuel jet injected transverse to non-reacting supersonic airflow. The species extracted at the wall were analyzed by gas chromatography. A large part of the recirculation region had a nearly uniform fuel distribution; the region was fuel-rich in composition. The fuel concentration in the recirculation region decreased with decreasing fuel mass flow rate. It was estimated that approximately 5 % of the injected fuel was entrained in the recirculation region.

McDaniel et al.⁴¹ made 3-D measurements of flow variables for a flow field with staged transverse fuel injection downstream of a step in non-reacting supersonic flow. Pressure, temperature, velocity and fuel mole fraction were measured using LIF. Fuel

was entrained into the recirculation region behind the step from the jet closer to the step base; fuel concentration close to stoichiometry was observed in the recirculation region.

Strokin and Grachev⁴² obtained experimental data on ignition and flameholding in supersonic flow using a cavity flameholder for a variety of experimental conditions; the results were also reported by Ogorodnikov et al.⁴³. The data was correlated to obtain a flame stability curve using the air/fuel equivalence ratio in the cavity recirculation zone and a flameholding parameter based on the airflow velocity, airflow stagnation temperature, recirculation region static pressure and cavity length. The equivalence ratio in the recirculation region was empirically estimated using air and fuel stagnation temperature, recirculation region static temperature, approaching airflow boundary layer thickness, spacing between fuel injection holes, and overall air/fuel equivalence ratio.

Morrison et al.⁴⁴ performed experimental and analytical studies on a dual-mode propane-fueled ramjet/scramjet combustor to determine the conditions necessary to establish flameholding in the engine. The effects of non-premixed fuel-air mixture and combustion-induced shock train on flameholding were investigated. Hydrogen was injected near the exit to raise the back-pressure and establish a shock train that resulted in subsonic flow over the step flameholder and simulated ramjet conditions. Propane was injected at a low velocity at the step base to prevent it from penetrating through the recirculation region. The air entrainment rate into the recirculation region was estimated analytically from the step base pressure measurements. Premixed conditions were assumed to exist in the recirculation region and the local equivalence ratio in the region was calculated from the known fuel flow rate and estimated air entrainment rate. Lean blowout at a local equivalence ratio close to unity indicated poor fuel-air mixing in the

recirculation region; the mixing efficiency was estimated as 30%. The experiments were repeated for different levels of back-pressure to determine both fuel-lean and fuel-rich blowout points and construct a flame stability curve. The curve was similar in shape to the Ozawa stability loop for premixed subsonic flow²⁴, but it had reduced blowout limits.

Computations

Kim et al.⁴⁵ reported 2-D numerical simulation of fuel injection over a cavity in non-reacting supersonic flow. When fuel was injected upstream of the cavity, it drastically suppressed flow oscillations in the incoming boundary layer leading to a more stable free shear layer over the cavity. For downstream injection, the interaction between flow oscillations near the aft cavity wall and the injected jet amplified the cavity pressure oscillations as compared to the case without injection. Fuel mass fraction contours showed that large vortices occurred that pulled the fuel upstream into the cavity.

Correa and Warren⁴⁶ performed 2-D numerical simulations and experiments for non-reacting supersonic flow over a backward-facing step. Fuel was injected downstream of the step and transverse to the airflow. The computed fuel mixture fraction showed that the fuel was confined to the wake of the step. In reality, a 3-D horse shoe vortex forms around the fuel jet and it penetrates further into the main airflow.

Glawe et al.⁴⁷ performed 2-D numerical simulations for helium injected at the base of a strut in non-reacting supersonic flow. CFD contours showed a high helium mole fraction distribution in the recirculation region formed at the base of the strut.

Mass Sampling for Species Concentration Measurement in Supersonic Flow

Mitani et al.⁴⁸ performed experiments and computations to analyze and select a suitable mass sampling probe for a hydrogen supersonic combustor. The extracted samples were analyzed for species composition using gas chromatography. Different

types of gas sampling probes were examined: a reaction-oriented probe having a uniform cross-section with no water cooling; a reaction-freezing oriented water cooled probe with a short cross-section expanding to a larger cross-section to facilitate expansion cooling of the sampled gas; and a static pressure-type probe to grasp the external flow across the boundary layer on probe surface. The effectiveness of freezing-oriented probe was examined by comparison with reaction-oriented probe. Combustion efficiency as a function of stagnation temperature T_0 was estimated from gas sampling by each of the probes. The reaction-oriented probe allowed reactions to continue ahead of and inside it and showed complete combustion for $T_0 > 910$ K. It gave high but false values for combustion efficiency. The freezing-oriented probe indicated that combustion was initiated when $T_0 > 1200$ K and gave lower combustion efficiency, which were in line with static-type probe measurements. The validated gas sampling was applied to scramjet testing under flight Mach numbers up to 8. They clarified distortions of air and hydrogen in the swept-back, side-compression type engines.

Chinzei et al.⁴⁹, Masuya et al.⁵⁰, Ciezki et al.⁵¹, Rogers⁵² used mass sampling and subsequent analysis by gas chromatography to determine species distribution at different cross-sections in a supersonic combustor for non-reacting and reacting flow. The mixing effectiveness of various fuel injection configurations such as step injection, strut injection, and wall injection normal to the airflow were examined.

Ng et al.⁵³ developed an aspirating hot-film mass sampling probe and used it to measure local gas composition in a helium-air supersonic shear layer. The probe consisted of a diverging section followed by a constant area section and a choked orifice, and was connected to a vacuum pump at the back. The configuration allowed the sampled

flow to expand and form a normal shock in the diverging section of the probe, thus avoiding a normal shock and flow spillage at the probe tip. The hot-film sensor was placed in the constant area section of the probe and was connected to an anemometer. The voltage response of the anemometer is a function of the sampled gas composition, total pressure and total temperature experienced by the sensor. The total pressure and temperature at the sensor were measured separately, which allowed for the determination of sampled gas composition using calibration curves. Cox et al.⁵⁴ used the probe to study mixing efficiency of an aerodynamic ramp in supersonic flow.

Optical Diagnostics for Species Concentration Measurement in Supersonic Flow Planar Laser-Induced Fluorescence (PLIF)

Hanson et al.⁵⁵, Schulz and Sick⁵⁶ provided an overview of planar laser-induced fluorescence (PLIF) as a diagnostics tool for measuring species concentration, temperature, pressure and velocity in the flow field. The fluorescence signal S_f can be expressed as follows.

$$S_f = \eta_{optics} \frac{E}{hc/\lambda} dV_c \frac{\chi P}{kT} \sigma_{abs} \frac{A}{A+Q} \quad (1-10)$$

- where η_{optics} : efficiency of the collection optics
 E : laser fluence (J/cm²)
 hc/λ : energy of a photon
 dV_c : collection volume (cm³)
 χ : mole fraction of absorbing molecule
 σ_{abs} : molecular absorption cross section (cm²)
 A : spontaneous emission rate (s⁻¹)
 Q : collisional quenching rate (s⁻¹)

The ratio $A / (A + Q)$ gives the fluorescence yield ϕ , which is the fraction of absorbed photons re-emitted as fluorescence photons. ϕ depends on composition, temperature and pressure of the gas mixture, and excitation wavelength. σ_{abs} depends on gas temperature and excitation wavelength. Hence the fluorescence signal is a function of species mole fraction, temperature, pressure and excitation wavelength. Mole fraction imaging is straightforward for a flow with relatively constant temperature and pressure. For a relatively constant pressure flow with temperature variation, the mole fraction can be determined by selecting a suitable excitation wavelength that minimizes the signal's overall temperature dependence in the temperature range of experiment. Another approach is to take two almost simultaneous images with excitation at two different wavelengths. The ratio of the two image signals is a function of temperature only. The flow field temperature variation thus obtained can be used to determine the mole fraction distribution from either of the images.

Fox et al.⁵⁷ used NO PLIF to determine the fuel mole fraction distribution and evaluate the mixing performance of various fuel injectors in supersonic flow. The temperature dependence of the signal was minimized by tuning the laser to excitation wavelengths for which fluorescence is relatively independent of temperature. The pressure dependence of the signal was minimized by canceling the implicit pressure dependence of fluorescence yield with explicit pressure dependence of number density; this was achieved by increasing the quenching cross section to an order of magnitude higher than the fluorescence cross section.

Hartfield et al.⁵⁸, Abbitt et al.⁵⁹, Hollo et al.⁶⁰, Hartfield et al.⁶¹ used iodine PLIF to measure injectant mole fraction distribution in non-reacting supersonic combustor and evaluate mixing rates for different injection configurations. The fluorescence intensity was a function of injectant concentration as well as the local thermodynamic pressure and temperature. The ratio of the fluorescence signal collected with only the injectant jets seeded to the signal collected with both the jets and the main flow seeded was taken to cancel the thermodynamic dependence of fluorescence, and the injectant mole fraction was obtained as follows.

$$X_{injectant} = \frac{N_{jet}}{N_{total}} = C' \frac{S_{f-jet}}{S_{f-total}} \quad (1-11)$$

where X : mole fraction, N : number density, S_f : signal intensity.

Lozano et al.⁶² explored the use of acetone ($\text{CH}_3\text{-CO-CH}_3$) as a suitable tracer for PLIF concentration measurements in gaseous flows. Acetone has a fairly high vapor pressure (180 torr) at room temperature (293 K) and hence allows a good seeding density, which can be increased further by increasing the temperature. It absorbs over a broadband of wavelengths (225-320 nm) with a maximum between 270-280 nm (absorption cross-section $\sigma = 4.7 \times 10^{-20} \text{ cm}^2$). The fluorescence emission is broadband in blue (350-550 nm) with peaks at 445 and 480 nm, quantum efficiency $\phi = 0.2 \%$, and a short lifetime of less than 4 ns. The fluorescence quantum yield is dominated by intersystem crossing; collision quenching is negligible and hence the yield is independent of local gas composition. For the experimental conditions investigated, the signal showed no dependence on temperature and hence was only sensitive to the species concentration. Acetone phosphoresces in the blue, with a similar emission spectrum as fluorescence

(350-600 nm) and a long decay time (200 μ s for 313 nm excitation). However, it is greatly quenched by trace amounts of oxygen and also depends on temperature.

Bryant et al.⁶³ conducted experiments to determine the temperature and pressure dependence of acetone LIF signal. The pressure and temperature range investigated were 0.1 - 1.0 atm and 240 - 300 K respectively, conditions akin to that in a supersonic wind tunnel. For laser excitation wavelength of 266 nm, the LIF signal showed no dependence on pressure and varied by 5% over the temperature range. Hence the signal can be used to directly obtain species concentration in an acetone-seeded flow.

Thurber et al.⁶⁴ investigated the temperature and excitation wavelength dependence of acetone LIF signal; the temperature range was 300 - 1000 K and the wavelength range was 248 - 320 nm. The signal varied with temperature and wavelength for the range investigated. At 266 nm, the signal per molecule was constant for 300 - 350 K and decreased for higher temperatures.

VanLerberghe et al.⁶⁵ used acetone PLIF to investigate mixing of an under-expanded sonic jet injected transversely in a supersonic crossflow. Instantaneous, mean, standard deviation images and image intensity probability density functions (PDF) were used to study the mixing process. For the given flow conditions, PLIF signal intensity was proportional to the acetone mixture fraction; temperature and pressure were estimated to not play a significant role.

Hartfield et al.⁶⁶ measured pressure, temperature and velocity in supersonic flow using iodine PLIF. The uncertainty in measurements due to possible condensation of iodine in the low temperature supersonic airflow was investigated. Minor condensation was observed on the test section walls. The signal intensity from the condensed droplets

would be much higher than that from vapor. However, the measured signals were comparable with the calculated theoretical values. Hence no direct evidence of significant iodine condensation in the airflow was observed.

Raman Scattering

O'Byrne et al.⁶⁷ used dual-pump coherent anti-Stokes Raman spectroscopy (CARS) to measure temperature and mole fraction distribution of N₂, O₂ and H₂ in a supersonic combustor. A parallel CFD study was done by Cutler et al.⁶⁸. CARS has the advantage of producing a coherent signal beam in a particular direction. This increases the signal-to-noise ratio, and also allows measurements where optical access to the flow is limited. Three lasers were used in the experiments. The 532 nm beam output from a Nd:YAG laser was split three ways. The first beam was used as the green pump beam for N₂ CARS. The second beam was used to pump a dye laser operating at 554 nm that provided the yellow pump beam for O₂ CARS. The third beam was used to pump another dye laser operating at 607 nm that provided the red stokes beam for both N₂ and O₂ CARS. The frequency difference between blue pump beam and red stokes beam equals a vibration Raman shift of N₂, while the frequency difference between yellow pump beam and red stokes beam resonates with a vibration Raman shift of O₂. The resulting blue CARS spectrum contains both N₂ and O₂ spectra. Coincidentally, several pure-rotational Raman transitions of H₂ are also present in this spectral region. The relative intensities of N₂, O₂ and H₂ spectra provided a measure of mole fractions of these species.

Kasal et al.⁶⁹ evaluated mixing of hydrogen injected from planar and lobed struts in supersonic non-reacting flow. 1D Raman spectroscopy was used to measure species composition at different cross-sections along the combustor. A 532 nm, 400mJ Nd:YAG

laser was used as the exciting source. The resulting Raman spectrum was used to obtain mole fractions of H₂, O₂ and N₂ in the flow.

Scope of Study

The aim of this study is to investigate the non-premixed conditions in the recirculation region formed behind a rearward step in supersonic flow; such a study is of practical importance in understanding the flameholding mechanism in a scramjet engine combustor. The step is selected as the flameholder geometry since it is the simplest and most widely used configuration in a supersonic combustor. The literature review section discussed earlier shows that only a few investigations have been conducted to determine the local species distribution in the flameholder recirculation region for non-reacting supersonic flow. As per the author's knowledge, no such data has been reported for combustion tests.

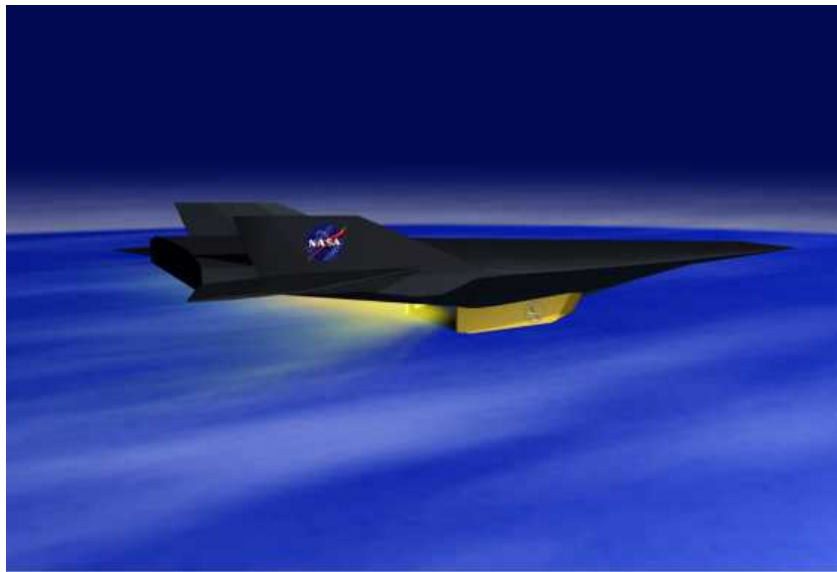
This study creates a database of local species mole fraction and fuel equivalence ratio distribution in the recirculation region formed behind a step in supersonic flow. Such a database also helps in providing useful input data for complementary computational fluid dynamics (CFD) efforts. Both non-reacting and combustion cases were investigated. The airflow parameters such as Mach number, stagnation pressure and stagnation temperature were held constant. For a given flow condition, the influence of the following fuel related parameters on the species distribution and combustion in the flameholding recirculation region were investigated:

- Fuel injection location relative to the recirculation region
- Fuel injection pressure
- Fuel type

The tools used in the investigation were a combination of mass sampling and composition analysis using mass spectrometry (MS) and acetone planar laser induced fluorescence (PLIF) for visualizing species concentration distribution in non-reacting flow.



(a)



(b)

Figure 1-1. Comparison between (a) Rocket-powered vehicle [Source: www.isro.org] and (b) Scramjet-powered hypersonic vehicle [Source: www.nasa.gov].

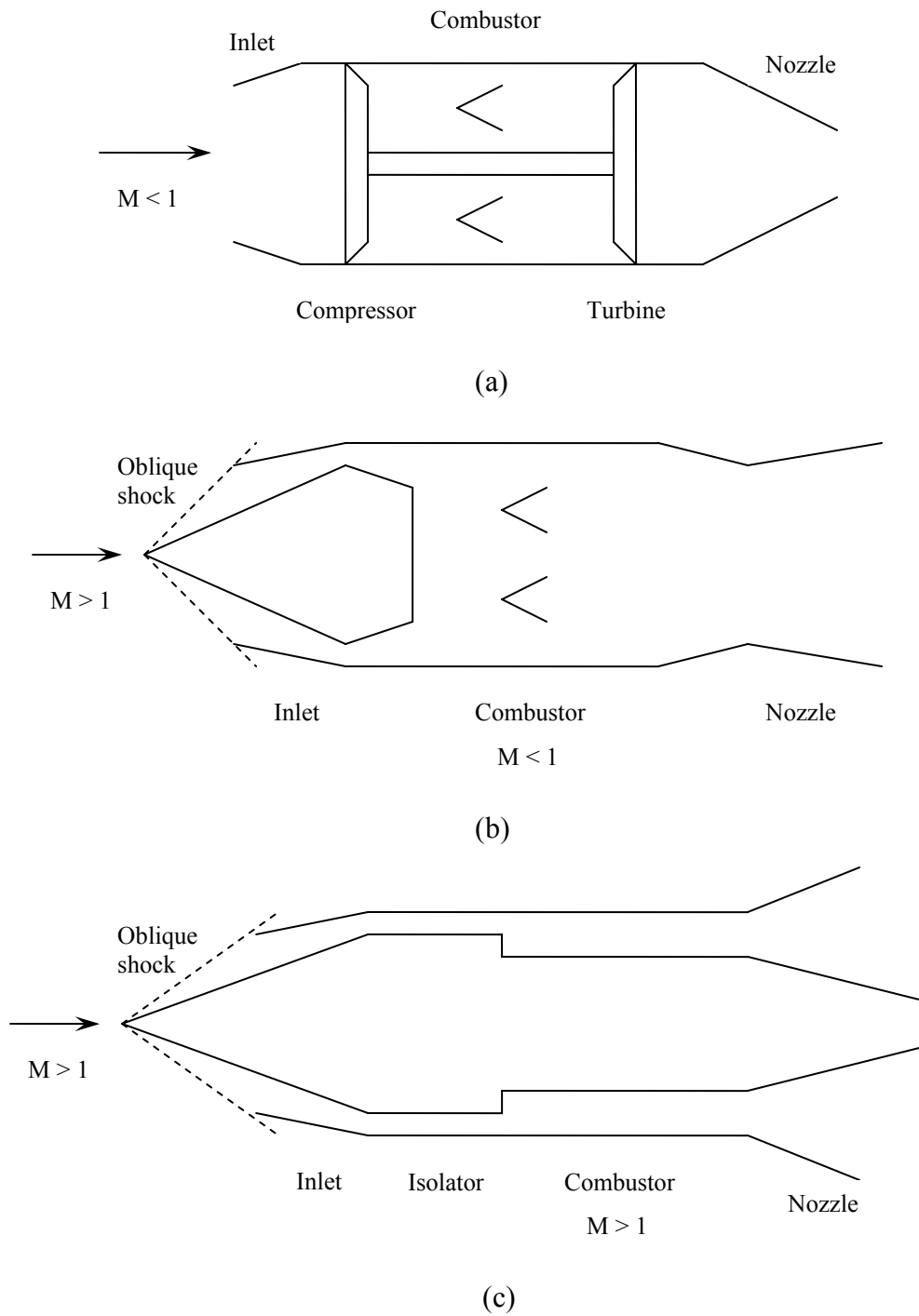


Figure 1-2. Schematic diagram of (a) turbojet engine (b) ramjet engine (c) scramjet engine.

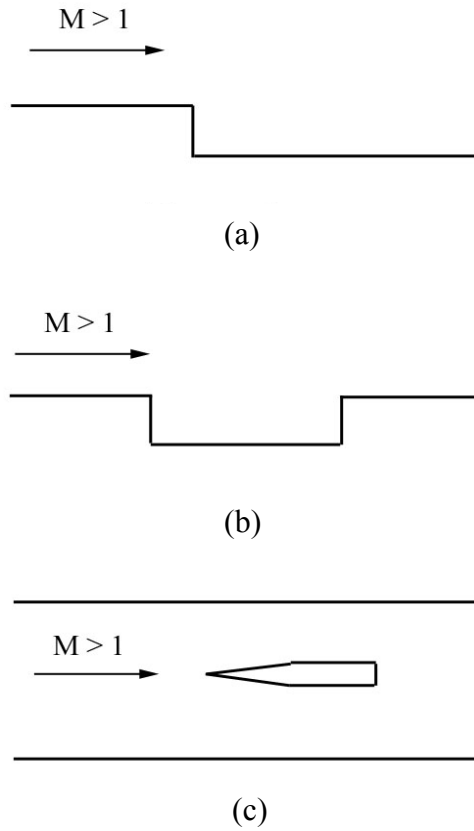


Figure 1-3. Various flameholder geometries for supersonic flow: (a) rearward step (b) cavity (c) strut.

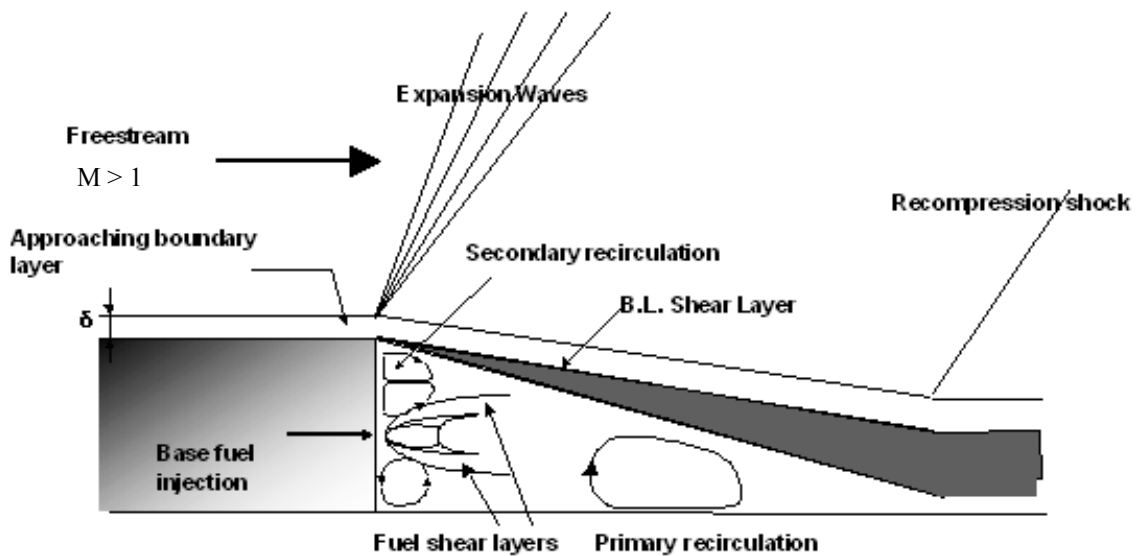


Figure 1-4. Schematic diagram of supersonic flow over a rearward step.

CHAPTER 2 EXPERIMENTAL SETUP

Supersonic Wind Tunnel

The supersonic wind tunnel facility used in the experiments, and shown in Figure 2-1 (a), provides direct connect tests with a variable combustion chamber entrance Mach number of 1.6 - 3.6 and stagnation temperatures corresponding to Mach 3.0 - 4.8 flight. The flight Mach numbers correspond to the transition phase from ramjet to scramjet engine. The wind tunnel is a continuously operating facility using a vitiated heater based on hydrogen combustion with oxygen replenishment, electronically controlled by a fuzzy logic controller⁷⁰ to maintain a constant 0.21 oxygen mole fraction at all conditions, and to maintain at the heater exit the constant stagnation temperature profile required for the experiment. A bell mouth with four-side contraction leads to the supersonic nozzle with compression on two sides and interchangeable nozzle blocks that cover the range of Mach 1.6 - 3.6. All the experiments discussed here were performed with combustion chamber entrance Mach 1.6 and cold air ($T_{0\text{air}} = 300 \text{ K}$). A constant area isolator is placed between the nozzles and the combustor section to protect the nozzle from upstream pressure rise due to combustion in the test section. Optical access is available to the isolator's flow from three sides. The isolator cross-section is $2.5 \times 2.5 \text{ cm}^2$ upstream of a rectangular, rearward facing step having step height $H = 12.7 \text{ mm}$, and follows with a constant cross-section area test section $26H$ in length. The test section is symmetric and has the option of optical access through covering windows. It was water-cooled for combustion tests.

Fuel was injected transverse to the airflow and into the recirculation region $0.2H$ from the base of the step, or transverse to the airflow and at a distance $4H$ upstream of the step; a schematic diagram is shown in Figure 2-1 (b). For base injection, five 0.5-mm dia. holes equally spaced on each side of the test section wall were used. For upstream injection, two 1.0-mm dia. holes equally spaced on each side of the isolator wall were used. Helium - having molecular weight close to hydrogen, and argon – having molecular weight close to propane, were injected as simulated fuel in non-reacting flow tests. Hydrogen was injected in combustion tests.

A LabView program and associated National Instruments hardware was used to monitor experimental conditions such as airflow stagnation pressure, temperature and Mach number at the nozzle exit, fuel stagnation pressure and temperature, test section wall static pressure and temperature distribution along the airflow direction. Mass spectrometry (MS) and planar laser induced fluorescence (PLIF) were used to determine the species mole fraction distribution in the recirculation region as described below.

Mass Sampling and Analysis

Hardware

The physical location of mass sampling ports in the recirculation region behind the step is shown in Figure 2-1 (b). The coordinate system is also shown in the figure. The test section window wall covering the step has five mass sampling ports in the recirculation region along the axial x -direction equally spaced from $x/H = 0.5$ to 3.5 and along $y/H = 0.3$. These ports are 0.6 mm inner diameter steel tubes that end at the test section window wall and do not physically intrude into the recirculation region ($z = 0$). In separate tests, other tubes are inserted from the window wall to verify the two-dimensionality of species distribution in the recirculation region. For non-reacting flow

tests, three stainless steel tubes are placed at $x/H = 2.0$, $y/H = 0.3$, the location of port #3 in wall sampling; they penetrate into the test section to sample species at three different depths, equally spaced in the inflow z -direction from $z/W = 0.33$ to 1.0. Here $W = 12.7$ mm is the test section half-width. For combustion tests, five 0.8 mm inner diameter ceramic tubes are inserted to $z/W = 0.5$ from the wall at the same axial locations as the wall sampling ports. Exposure to high temperatures of hydrogen combustion flow field in the flameholding region can cause metals to melt or oxidize. Hence the inflow sampling tubes for combustion tests were made of ceramics to withstand the high temperatures; inspection of these tubes after experiments showed that they remained intact during the tests.

A schematic diagram of mass sampling from the recirculation region and subsequent, real-time analysis by a mass spectrometer is shown in Figure 2-2 (a). In combustion tests, the extracted species passed through a water-cooled jacket on their way to the mass spectrometer to quench the reactions and freeze the species composition coming out of the combustion chamber. The jacket was supplied with cold water coming out of a chiller at 283 K. The temperature drop of the sampled mixture while passing through the cooling jacket resulted in condensation of water vapor and much of it could not reach the mass spectrometer. Hence the corrected X_{H_2O} was deduced from the oxygen deficit in the product mixture.

The sampling tubes coming out of the recirculation region were connected to a manifold having six 0.6-mm diameter input tubes and a single 1.8-mm diameter outlet tube connected to the mass spectrometer. The input of species to the manifold was regulated by a series of computer-controlled miniature solenoid valves that supply gas

mixture from one sampling port at a time for analysis. Sampling from each port was preceded by injection of nitrogen in the manifold to purge the line and flush the species from the previous port, hence preventing mixing of samples from two adjacent ports. A LabView program and associated National Instruments hardware was used to send analog signals to operate the miniature solenoid valves in the desired sequence. The sampling time at each port and the purge time before each sampling were input to the software. The software is attached in Appendix A. Due to small volume of the sampling system, only a small mass of species was extracted from the recirculation region, which in turn facilitated quenching of the reacting species and also helped the mass spectrometer attain steady state measurements almost instantaneously while switching from one port to another.

The species were analyzed by Stanford Research Systems RGA-300 mass spectrometer, shown in Figure 2-2 (b), that uses electron ionization to ionize the sampled gas, RF quadrupole filter to sort species according to their mass-to-charge ratio, and Faraday cup to detect ion currents. The instrument is controlled and operated by software and associated electronics. The ionizer, filter and detector are enclosed in a clean vacuum chamber and require an operating pressure range of 10^{-4} torr (1.3×10^{-7} atm) to ultra high vacuum. Such low pressure is attained in two stages. In first stage, a rotary pump brings the inlet pressure down to about 60 mtorr (7.9×10^{-5} atm). In second stage, a diffusion pump and a rotary pump operate in series to bring the pressure further down to vacuum conditions. The spectrometer can detect species up to a mass-to-charge ratio of 300 and has a resolution of 0.5 AMU @ 10% peak height. The sensitivity factor of the instrument, defined as the signal detected per unit partial pressure of a given species (Amp / torr),

varies for different gases. Hence calibration of the instrument was performed for the following gases: helium, nitrogen, oxygen and argon. The sensitivity factor of nitrogen is used as the baseline and sensitivity factors of other gases are normalized with this baseline. The relative sensitivity factor ($S_{\text{gas}} / S_{\text{N}_2}$), also referred as the calibration factor, is shown in Table 2-1 for different gases.

Data Processing

The composition of gas in the recirculation region was analyzed by the mass spectrometer in partial pressure of species vs. time mode. The species scanned were nitrogen ($m/z=28,14$), oxygen ($m/z=32,16$), helium ($m/z=4$), argon ($m/z=40,20$) for non-reacting experiments, and nitrogen ($m/z=28,14$), oxygen ($m/z=32,16$), hydrogen ($m/z=2,1$), water ($m/z=18,17$) for combustion experiments. Sampling was done sequentially for 5 sec at the purge port and for 20 sec at each of the sampling ports. The spectrometer had a fast response time of about 2-3 sec to the change in composition of gas while switching from one port to another. The local mole fraction of a given species in the sample was determined from the partial pressures of all the component species recorded by the mass spectrometer. The time-averaged fuel mole fraction at a port was obtained by averaging the mole fractions obtained over the sampling time period. The species mole fractions were corrected using calibration factors for individual gases. The background level of argon in the incoming airflow for non-reacting experiments, and the background levels of hydrogen and water for combustion experiments were subtracted to determine the actual mole fractions of these species. Figure 2-3 shows the species mole fraction distribution in the recirculation region as the solenoid valves switch sequentially from one sampling port to another under steady experimental conditions; a non-reacting

flow case with helium as the simulant fuel is shown in Figure 2-3 (a) and a reacting flow case with hydrogen combustion is shown in Figure 2-3 (b).

The global mole fraction/equivalence ratio of fuel was determined from the total mole of fuel injected and the total mole of air traveling through the test section. Both local and global mole fractions/equivalence ratios are indicated in the results.

Optical Diagnostics

Hardware

Since mass spectrometry was limited to point-wise measurements in the flow, it was complemented by acetone planar laser induced fluorescence (PLIF) to obtain fuel distribution in a 2D plane in the recirculation region for non-reacting flow. The plane of measurement was along $z/W = 0.9$. The PLIF measurements overlap with MS data at the point $x/H = 2.0$, $y/H = 0.3$, $z/W = 0.9$; Figure 2-1 (b) shows the laser sheet in the test section and the common point between MS and PLIF where measurements from the two techniques are compared in Chapter 3.

A schematic diagram of PLIF setup is shown in Figure 2-4. The test section used in PLIF measurements had step on only one side, unlike on both sides for the test section used in mass spectrometer measurements. However, since the airflow arriving at the step base is supersonic, the flow field in the recirculation region is the same for both test sections. The test section side wall window was made of glass for laser sheet delivery in the recirculation region. The test section front windows next to the step were also made of glass to provide visual access of the measurement plane via a camera. Before being injected in the test section, the fuel was seeded with acetone vapor by bubbling it into a chamber partially filled with liquid acetone at room temperature (295 K).

A pulsed Nd:YAG Spectra-Physics laser was used for LIF excitation of acetone. The laser pulses at a frequency of 10 Hz and can have wavelength outputs of 1064, 532, 355 and 266 nm. The fourth harmonic 266 nm beam was used for acetone PLIF. At 266 nm wavelength, the laser pulse had 70 mJ energy and a pulse width of 4-5 ns. The beam diameter coming out of the laser was 7 mm. It was converted into a sheet of light and delivered in the test section using a range of optics suited for UV range of laser light. The beam was first oriented towards the region of interest in the test section using three 25.4 mm diameter mirrors. Then the beam diameter was increased and collimated using spherical lenses. Two 25.4 mm diameter spherical lenses, a concave lens with $f = -30$ mm and a convex lens with $f = 50$ mm were placed next to each other with an effective focal length of $f = -75$ mm. The effective concave lens diverged the beam and increased its diameter. A 50.8 mm diameter spherical convex lens with $f = 300$ mm was placed 205 mm ahead of them. This resulted in a collimated beam with an increased diameter of 40 mm. This beam was then converted to a sheet of light using cylindrical lenses. Two 50.8 x 50.8 mm cylindrical lenses were used, a convex lens with $f = 300$ mm and a concave lens with $f = -300$ mm. The concave lens was placed 75 mm ahead of the convex lens, and together they formed an effective convex lens, with the step placed 865 mm away at the focal point. The effective cylindrical lens converged the beam in the horizontal direction while leaving it unchanged in the vertical direction. The beam thus progressively converged into an ellipse with diminishing minor axis and unchanged major axis, and it formed a sheet 40 mm wide and less than 0.5 mm thick at the step. The sheet thickness did not change appreciably in the recirculation region due to high effective focal length of the lenses.

For image acquisition of acetone fluorescence in the visible spectrum, a Cooke corporation intensified CCD camera and its associated software was used. The camera has a resolution of 1280 x 1024 pixels, 12-bit dynamic range and shutter speed down to 3 ns. The software was used to set the camera parameters before taking images and also to save the captured images on the computer. The images were captured with an exposure time of 300 ms and a gain of 65%, with 100% representing the maximum gain achievable. A 2 x 2 binning was performed on the image in horizontal and vertical direction, that is, the average intensity of a square comprising 4 pixels was represented as the value for one pixel that replaced the 4 pixels. The camera resolution was 12 pixels/mm.

Image Acquisition and Processing

For each image acquisition, a total of 20 images were captured to get a time-averaged image over 2 s. Three set of images were required for analyzing each experimental condition: the background image [Figure 2-5 (a)], the laser sheet profile image [Figure 2-5 (b)], and the actual experiment image. To obtain the laser sheet profile, the test section was closed and filled uniformly with acetone vapor, and then excited by laser sheet. Since the acetone concentration was uniform, the acquired image captured the spatial intensity variation in the laser sheet due to its Gaussian profile.

The nature of the experiment created challenges in getting a low background image. The air arrived at the step base with $M = 1.6$ and had a low static temperature of $T = 200$ K. However, it slowed down in the recirculation region to low subsonic Mach numbers and the static temperature recovered close to the stagnation temperature of 300 K. Hence a temperature gradient existed in the shear layer separating the recirculation region and the main airflow. This low air temperature caused the acetone vapor injected

in the test section to condense in the shear layer. The liquid acetone sprayed onto the glass window and created a high background for the camera. This issue was overcome by using a heat gun to heat the glass window up to 365 K just before starting airflow through the test section. Even as the heat gun was in operation during the operation of the wind tunnel, the glass window temperature dropped rapidly due to contact with cold airflow. Hence fuel seeded with acetone was injected in the test section and images were acquired within the first few minutes of starting the wind tunnel so that the glass window temperature would not drop below 329 K, the boiling temperature for acetone. This procedure reduced the background quite substantially. The background image set was acquired just after the experiment was over and the airflow and heat gun were turned off.

The post processing of images was performed using a program written in Matlab. The software is attached in Appendix B. An image is handled by Matlab as a 2D matrix containing light intensity at each pixel, hence image processing is essentially an operation with matrices. Each set of laser sheet profile, background and actual experiment images was averaged to get a time-averaged image. Then the background image was subtracted from the experiment image. The ultraviolet signal from Rayleigh scattering by acetone or from Mie scattering by condensed acetone droplets was filtered by the camera lens since it transmits only the visible spectrum of light. The laser sheet profile image was used to correct the experiment image for spatial non-uniformity in laser intensity using the following formula.

$$I_{corrected}(m, n) = I_{uncorrected}(m, n) * \frac{\max[I_{laser}(m, p)]}{I_{laser}(m, p)} \quad (2-1)$$

where I : pixel intensity

m, n : arbitrary row and column location of a pixel in the image

p : a fixed column in the laser sheet image

With the exception of airflow shear layer and sonic fuel jet injected in the test section, the temperature distribution in the recirculation region is rather uniform. Further, the acetone LIF signal does not vary with temperature for low temperature range of 200-300 K^{63, 64, 65}. The pressure distribution in the recirculation region is rather uniform. The acetone signal does not get quenched by oxygen⁶². Hence the LIF signal intensity variation in the corrected image is independent of pressure, temperature and oxygen concentration; it varies only with the concentration of acetone. With the assumption that acetone distribution in the flow is the same as that for the fuel, the fuel mole fraction distribution in the flow was determined quantitatively. The acetone LIF signal at the fuel injection location, where fuel mole fraction is 100 %, was taken as the reference point for other pixels in the image. The fuel mole fraction at a given pixel was then determined by the ratio of LIF intensity at that pixel to the LIF intensity at the reference point.

$$X_{fuel}(\%) = \frac{I}{I_{reference}} * 100 \quad (2-2)$$

For each experimental condition, image averaging was performed for 3 repeatability experiments. The fuel mole fraction distribution image, which does not depend on the laser intensity variation, was used to determine the average PLIF image and standard deviation for repeatability tests. The temporal variation in laser sheet profile was quantified for the 60 min duration over which repeatability experiments were performed. The image processing software is attached in Appendix B. Figure 2-6 shows the laser sheet profile at $y/H = 1.1$ for three time intervals after the laser was started. Also included is the profile when the laser was shut down and restarted. The figure shows only a marginal change in laser profile over 85 min, the average standard deviation was 4%.

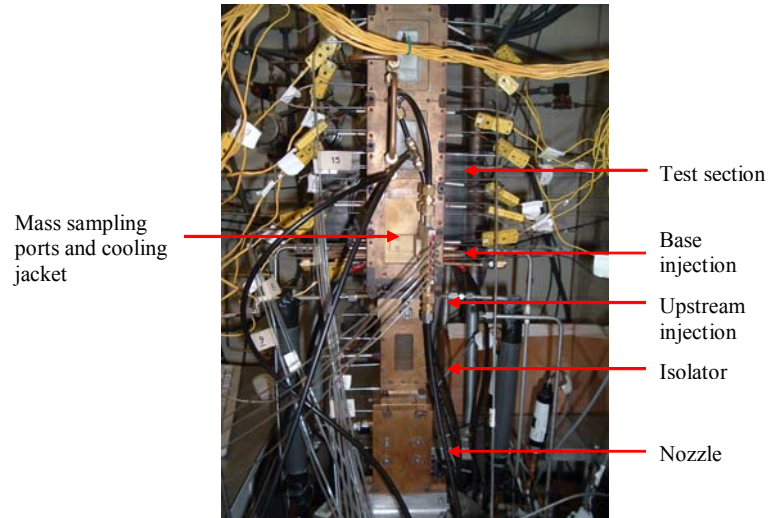
Restarting the laser did not affect the profile. The spikes in the profile reflect the quality of the beam coming out of the laser.

Convolution filtering was applied on the average PLIF image to smoothen the gradients due to noise. A 3 x 3 filter was applied to the image, that is, the signal intensity at a given pixel was replaced by the average intensity in a 3 x 3 pixel square with the given pixel at its center. The fuel mole fraction distribution was obtained from the filtered image.

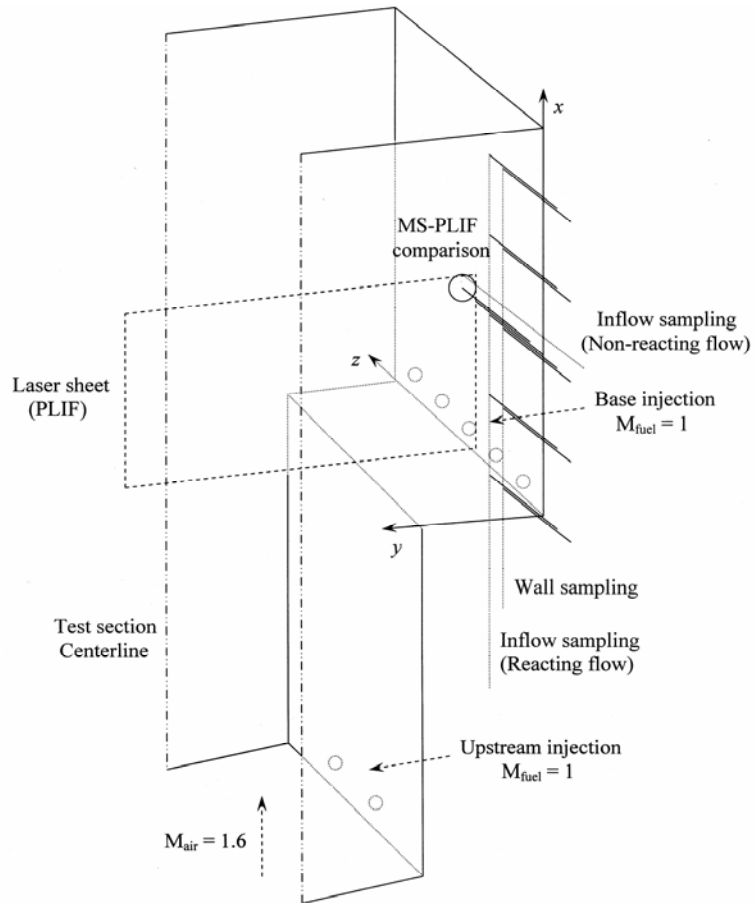
The binary diffusion coefficient of a gas in air is inversely proportional to the square root of its molecular weight; it indicates that helium diffuses about 4 times faster in air compared to acetone and argon diffuses at about the same rate as acetone. Hence acetone will not be able to trace helium accurately while it will still trace argon reasonably well. It suggests that the fuel mole fraction measurements determined from acetone PLIF may be more accurate for argon as the injectant than helium. Condensation of acetone vapor into droplets may also affect the PLIF signal intensity.

Table 2-1. Mass spectrometer calibration factors for various gases

$S_{\text{gas}} / S_{\text{N}_2}$			
Helium	Nitrogen	Oxygen	Argon
0.6	1.0	0.9	1.2

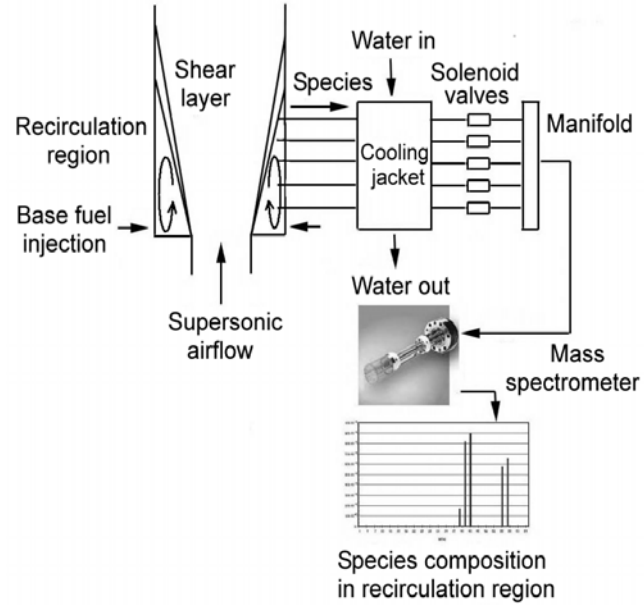


(a)

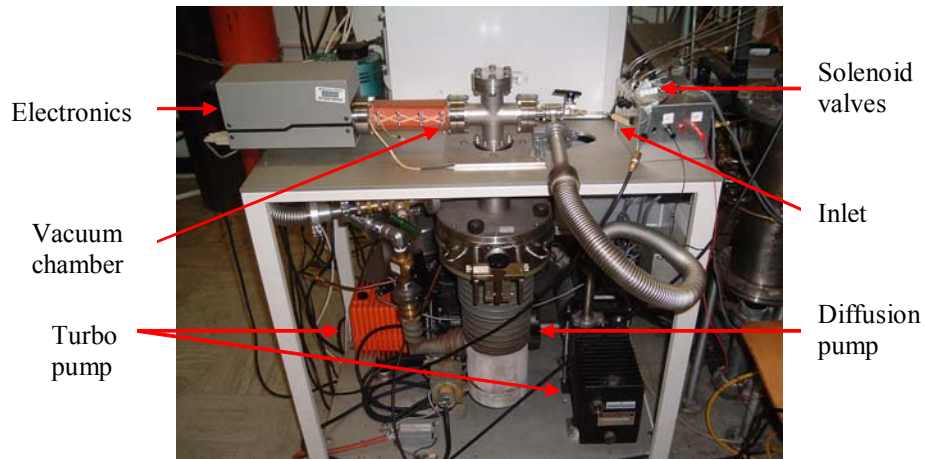


(b)

Figure 2-1. Description of the test section showing fuel injection and mass sampling locations: (a) image and (b) schematic diagram.



(a)



(b)

Figure 2-2. Mass sampling from the recirculation region behind the step for analysis by the mass spectrometer: (a) schematic diagram (b) image.

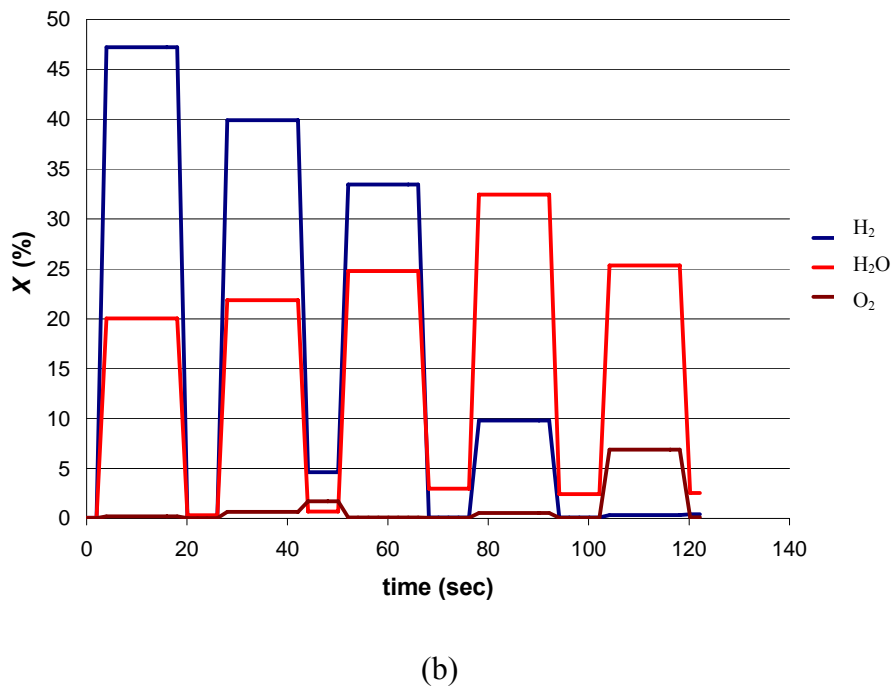
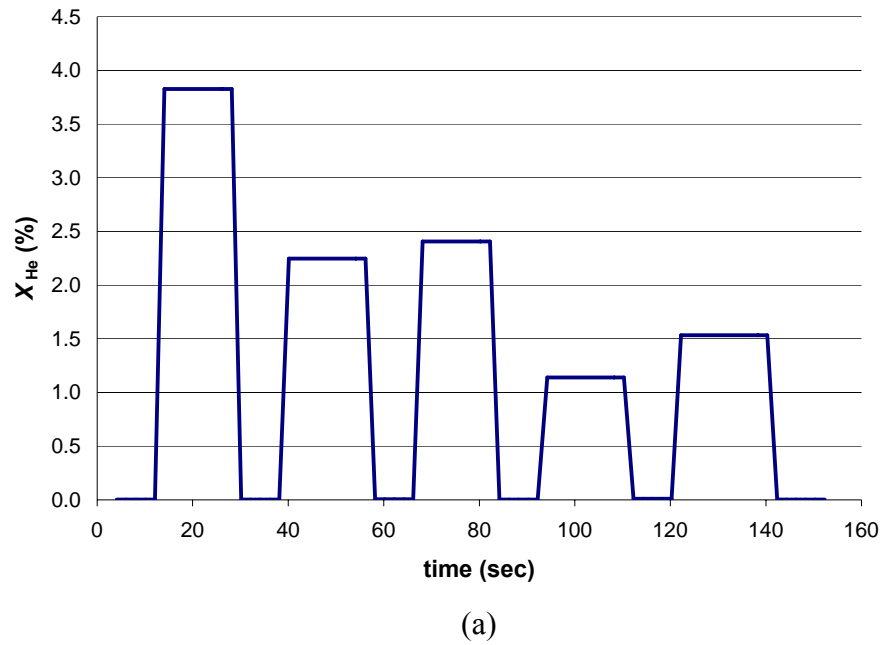


Figure 2-3. MS measurements of species mole fraction distribution in the recirculation region as the solenoid valves switch sequentially from one sampling port to another under steady experimental conditions (a) non-reacting flow with helium as the simulant fuel (b) reacting flow with hydrogen combustion.

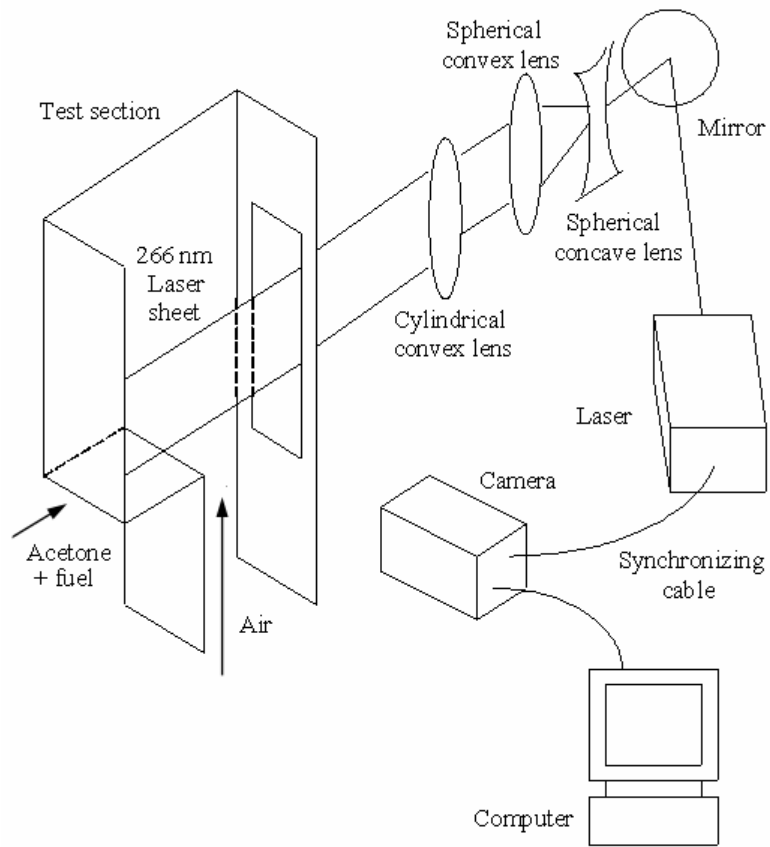
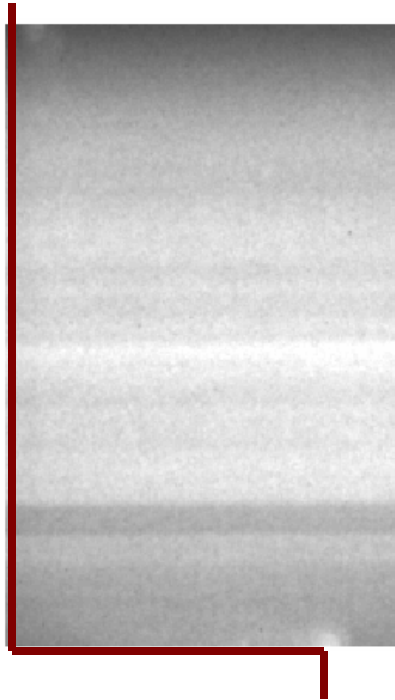


Figure 2-4. Schematic diagram of planar laser-induced fluorescence (PLIF) setup.



(a)



(b)

Figure 2-5. Sample PLIF image for (a) background (b) laser sheet.

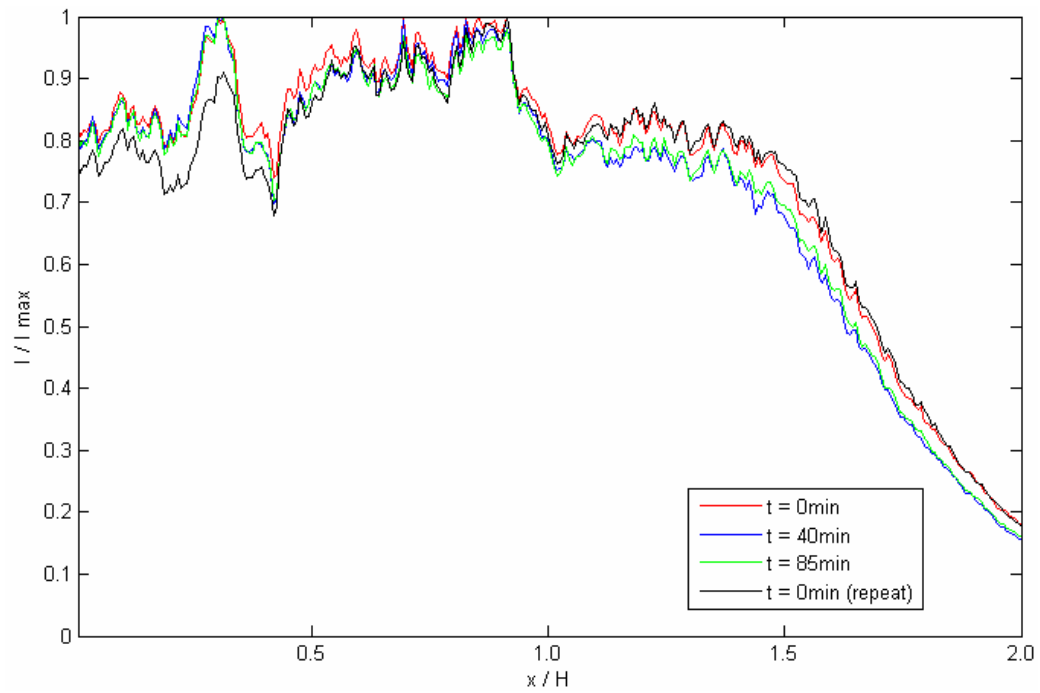


Figure 2-6. Temporal variation of laser sheet profile at $y/H = 1.1$.

CHAPTER 3

RESULTS: NON-REACTING FLOW

The study included non-reacting cases with the air conditions maintained at $M = 1.6$, $T_{0\text{air}} = 300 \text{ K}$, $P_{0\text{air}} = 4.8 \text{ atm}$. Helium and argon were injected as fuel simulants at two different pressures from the base of the step and from a location upstream of the step; the configuration is described in Chapter 2. The molecular weight of helium is close to hydrogen, while argon has molecular weight close to propane. The data obtained from non-reacting flow tests is limited since combustion of fuel-air mixture does not take place. However, it gives the fuel distribution in the flameholding region just before ignition of fuel-air mixture. Based on this information from non-reacting flow, the effect of various parameters, such as fuel injection pressure and location, on flameholding characteristics in actual combustion can be estimated. The mass exchange rate across the main airflow shear layer is higher for non-reacting flow compared to reacting flow²⁴. For non-reacting flow, this will bring more air into the recirculation region, hence the flameholding region may be leaner in fuel compared to reacting flow.

Mass Spectrometry (MS)

Base Injection: Helium

Non-reacting flow experiments were performed with helium as the fuel simulant. Each experiment was performed three times for repeatability. The average standard deviation in X_{He} was 4 %. Mass sampling of the recirculation region species was done along the wall in the x -direction with helium injected at the base of the step in $P_{0\text{air}} = 4.8 \text{ atm}$ airflow. The wall pressure distribution for airflow without fuel injection is shown in

Figure 3-1. The supersonic airflow expands at the step base, as indicated by the sharp drop in pressure at that location. The shear layer formed due to separation of the airflow boundary layer at the step base is pushed towards the wall and it reattaches downstream of the step. An oblique shock is formed at the reattachment point, causing a pressure rise at that location. Based on the pressure rise in the plot, the shear layer reattachment point is estimated to be 1.5-2.0 H. Oblique shocks result in a pressure rise towards the end of test section to match the ambient atmospheric pressure. The pressure distribution in the recirculation region remained unaffected due to fuel injection in the non-reacting flow tests. It indicates that fuel injection did not cause a substantial increase in the mass flow rate in the recirculation region.

Helium was injected at two pressures, a moderate stagnation pressure $P_{0\text{He}} = 5.4$ atm and a high stagnation pressure $P_{0\text{He}} = 12.0$ atm. The wall distribution of X_{He} in the recirculation region for the two $P_{0\text{He}}$ is shown in Figure 3-2 (a). The standard deviation bars are shown along with the average mole fractions for the repeated experiments. The fuel injection location is indicated on the horizontal axis. It is observed that the fuel mole fraction decreases in the x -direction and away from the fuel injection location, especially for lower $P_{0\text{He}}$. Increasing $P_{0\text{He}}$ substantially results in a corresponding increase in X_{He} in the recirculation region. The X_{He} distribution shows more non-uniformity at higher $P_{0\text{He}}$.

Mass sampling of the recirculation region species was done in the inflow z -direction for the same airflow and fuel injection conditions as in wall sampling. The inflow sampling was done at $x/H = 2.0$, $y/H = 0.3$. The inflow distribution of X_{He} in the recirculation region is shown in Figure 3-2 (b) for the two $P_{0\text{He}}$. At both pressures, the inflow X_{He} are much higher than the wall measured X_{He} , specifically, up to 4-5 times.

However, X_{He} distribution away from the wall is rather uniform, indicating a well mixed fuel-air mixture at the axial location probed.

Table 3-1 indicates the locally measured and the global X_{He} for wall and inflow sampling. The global X_{He} , defined in the earlier chapters, is obtained from the total moles of helium injected in the test section and the total moles of air flowing through the test section. For both $P_{0\text{He}}$, the locally measured X_{He} is up to 3 times more than the global estimate for wall sampling and about 10 times more than the global estimate for inflow sampling. It shows that even as the global X_{He} suggests a fuel-lean mixture, a fuel rich mixture can exist in the recirculation region.

Helium has a molecular weight close to hydrogen, hence the X_{He} distribution obtained from wall and inflow sampling is approximated to be similar to that of hydrogen injected under identical test conditions. Using this assumption, if hydrogen had been injected, the local equivalence ratios of hydrogen (ϕ_{H_2}) could be determined from the local mole fraction measurements. For $P_{0\text{H}_2} = 5.4$ atm, the local ϕ_{H_2} is estimated in the range of 0.04 – 0.4 for global $\phi_{\text{H}_2} = 0.04$. For $P_{0\text{H}_2} = 12.0$ atm, the local ϕ_{H_2} is estimated in the range of 0.1 – 0.7 for global $\phi_{\text{H}_2} = 0.1$. This confirms that a richer fuel composition mixture exists in the recirculation region even as the global ϕ_{H_2} suggests a relatively fuel-lean mixture. It is expected since only a fraction of the main airflow is entrained into the recirculation region. Hence the global ϕ_{H_2} does not capture the actual non-premixed conditions existing in the flameholding recirculation region.

Base Injection: Argon

Argon was injected at the base of the step for identical airflow and fuel injection conditions as in the case of helium injection. The average standard deviation in X_{Ar} was 3 %. Mass sampling of the recirculation region species was done along the wall in the x -

direction. The wall distribution of X_{Ar} in the recirculation region for the two P_{0Ar} is shown in Figure 3-3 (a). The X_{Ar} distribution pattern is similar to that for helium injection, especially for low injection pressure.

Mass sampling of the recirculation region species was done in the inflow z -direction for the same airflow and fuel injection conditions as in wall sampling. The inflow distribution of X_{Ar} in the recirculation region for the two P_{0Ar} is shown in Figure 3-3 (b). As in wall sampling, the inflow X_{Ar} distribution has a pattern similar to that for helium injection [Figure 3-2 (b)], especially for low injection pressure. The inflow X_{Ar} measurements are up to 2-3 times higher than the wall measured X_{Ar} .

The locally measured and the global X_{Ar} for wall and inflow sampling are shown in Table 3-2. The local to global X_{fuel} ratio can be interpreted as the fuel mole fraction in the recirculation region for a unit mole fraction of fuel injected in the test section. A comparison of data in Table 3-2 with Table 3-1 shows that the local to global X_{fuel} ratio is higher for argon than helium, that is, higher concentration of argon is found in the recirculation region than helium for a unit mole fraction of fuel injected in the test section. This could be attributed to diffusion; the binary diffusion coefficient of a gas in air is inversely proportional to the square root of its molecular weight, hence argon diffuses about 3 times slower in air compared to helium.

Argon has a molecular weight close to propane, hence the X_{Ar} distribution obtained from wall and inflow sampling is approximated to be same as that of propane injected under identical test conditions. For $P_{0C3H8} = 5.4$ atm, the local ϕ_{C3H8} is estimated in the range of 0.5 – 2.5 for global $\phi_{C3H8} = 0.1$. For $P_{0C3H8} = 12.0$ atm, the local ϕ_{C3H8} is estimated in the range of 1.0 – 4.3 for global $\phi_{C3H8} = 0.2$. This shows that a fuel-rich

mixture exists in the recirculation region even as the global $\phi_{C_3H_8}$ suggests a fuel-lean mixture.

Upstream Injection: Helium

Helium was injected upstream of the step in identical airflow conditions as the base injection experiments. The average standard deviation in X_{He} was 6 %. Helium was injected at two pressures, $P_{0He} = 2.4$ atm and 5.1 atm. The corresponding dynamic pressure ratios [$P_{dynamic} = \rho_{He}V_{He}^2 / \rho_{air}V_{air}^2$] are 0.5 and 1.0 respectively. Mass sampling of the recirculation region species was done along the wall in x -direction and in the inflow z -direction. The wall distribution of X_{He} in the recirculation region for the two P_{0He} is shown in Figure 3-4 (a) and the inflow distribution is shown in Figure 3-4 (b). The inflow sampling shows an almost proportional increase in X_{He} with P_{0He} . Table 3-3 summarizes the local and global X_{He} for wall and inflow sampling. The plots and the table show quite low levels of X_{He} in the recirculation region, hence indicating that upstream injection of helium is not effective in supplying fuel to the recirculation region. In fact, the local X_{He} is lesser than global X_{He} , indicating that the light gas penetrates through the main airflow shear layer and only a small quantity reaches the recirculation region.

The X_{He} distribution obtained in the experiments is approximated to be the same as that of hydrogen injected under identical test conditions. For $P_{0H_2} = 2.4$ atm, the local ϕ_{H_2} is estimated in the range of 0.01 – 0.02 for global $\phi_{H_2} = 0.02$. For $P_{0H_2} = 5.1$ atm, the local ϕ_{H_2} is estimated in the range of 0.01 – 0.03 for global $\phi_{H_2} = 0.05$. The fuel-lean conditions for upstream injection mode suggest difficulty in flameholding in a combustion experiment with hydrogen as the fuel.

Upstream Injection: Argon

Argon was injected upstream of the step for identical airflow and fuel injection conditions as in case of helium injection. Hence, argon was injected at the same dynamic pressure ratios as helium. The average standard deviation in X_{Ar} was 3 %. Mass sampling of the recirculation region species was done along the wall in x -direction and in the inflow z -direction. The wall distribution of X_{Ar} in the recirculation region for the two P_{0Ar} is shown in Figure 3-5 (a) and the inflow distribution is shown in Figure 3-5 (b). Table 3-4 summarizes the local and global X_{Ar} for wall and inflow sampling. Unlike the case of helium, the heavier gas argon reaches the recirculation region in quantities larger than the global X_{Ar} . It can be seen from the plots and from the local to global X_{Ar} ratios in the table that an increase in the upstream P_{0Ar} does not result in a corresponding increase in the amount of fuel reaching the recirculation region. If fuel is injected upstream at a low dynamic pressure ratio, it seeps into the boundary layer of the incoming airflow which carries it into the recirculation region. If the upstream fuel injection dynamic pressure ratio is increased, part of the fuel penetrates through the airflow boundary layer and escapes into the core airflow; hence less fuel reaches the recirculation region.

The X_{Ar} distribution obtained in the experiments is approximated to be the same as that of propane injected under identical test conditions. For $P_{0C_3H_8} = 2.4$ atm, the local $\phi_{C_3H_8}$ is estimated in the range of 0.2 – 0.3 for global $\phi_{C_3H_8} = 0.06$. For $P_{0C_3H_8} = 5.1$ atm, the local $\phi_{C_3H_8}$ is estimated in the range of 0.2 – 0.3 for global $\phi_{C_3H_8} = 0.1$. The fuel-lean conditions in the recirculation region for upstream injection mode, along with much lower flameholding limits for hydrocarbons as compared to hydrogen suggest difficulty in flameholding in a combustion experiment with propane as the fuel.

Planar Laser Induced Fluorescence (PLIF)

Base Injection: Helium

PLIF imaging of the recirculation region fuel distribution in the $z/W = 0.9$ plane was performed for identical airflow and fuel injection conditions as the mass sampling experiments. Each experiment was performed 3 times for repeatability. The average standard deviation in X_{He} , after deducting the X_{He} deviation due to the temporal variation in laser sheet profile discussed in Chapter 2, was 8 %. The results for helium injection are shown in Figures 3-6 and 3-7 for $P_{0\text{He}} = 5.4$ atm and 12.0 atm respectively. The PLIF image for $P_{0\text{He}} = 5.4$ atm is shown in Figure 3-6 (a) and the X_{He} distribution is shown in Figure 3-6 (b). The expansion of airflow at the step pushes the shear layer towards the test section wall. The fuel injection holes are inclined relative to the step base. This is clearly visible in the figures as the fuel jet impinges on the step base and forms a plume above it. This fuel injection configuration helps the fuel remain and mix within the recirculation region. The PLIF image for $P_{0\text{He}} = 12.0$ atm is shown in Figure 3-7 (a) and the X_{He} distribution is shown in Figure 3-7 (b). In agreement with the mass spectrometer measurements, the fuel remains in the recirculation region even as the injection pressure is increased. The X_{He} distribution shows more non uniformity for higher injection pressure.

The global X_{He} for $P_{0\text{He}} = 5.4$ atm and 12.0 atm are 1.1 % and 2.5 % respectively. As in mass spectrometer measurements, the local X_{He} in the recirculation region and shear layer [Figure 3-6 (b) and 3-7 (b)] are an order of magnitude higher than the corresponding global X_{He} values. The X_{He} distribution obtained in the experiments is approximated to be the same as that of hydrogen injected under identical test conditions. For $P_{0\text{H}_2} = 5.4$ atm, the global $\phi_{\text{H}_2} = 0.04$ and for $P_{0\text{H}_2} = 12.0$ atm, the global $\phi_{\text{H}_2} = 0.1$.

The global ϕ_{H_2} values suggest a fuel lean mixture for both injection pressures. With the observation that $\phi_{H_2} = 1$ corresponds to 30 % X_{H_2} in a hydrogen-air mixture, it is seen in Figure 3-6 (b) that for $P_{0H_2} = 5.4$ atm, part of the recirculation region has a fuel-rich mixture with $\phi_{H_2} > 1$. Figure 3-7 (b) shows that for $P_{0H_2} = 12.0$ atm, the entire recirculation region, excluding the main airflow shear layer, has $\phi_{H_2} > 1$.

Base Injection: Argon

Argon was injected at the base of the step for identical airflow and fuel injection conditions as in the case of helium injection. The average standard deviation in X_{Ar} , after deducting the X_{Ar} deviation due to the temporal variation in laser sheet profile, was 8 %. The results for argon injection are shown in Figures 3-8 and 3-9 for $P_{0Ar} = 5.4$ atm and 12.0 atm respectively. The PLIF image for $P_{0Ar} = 5.4$ atm is shown in Figure 3-8 (a) and the X_{Ar} distribution is shown in Figure 3-8 (b). The PLIF image for $P_{0Ar} = 12.0$ atm is shown in Figure 3-9 (a) and the X_{Ar} distribution is shown in Figure 3-9 (b). As in the case of helium injection, the fuel remains within the recirculation region for both injection pressures. By comparing fuel mole fraction distribution in Figure 3-8 (b) with Figure 3-6 (b) for low injection pressure and Figure 3-9 (b) with Figure 3-7 (b) for high injection pressure, it is observed that argon distribution in the recirculation region is similar to helium, especially for low injection pressure. This is in agreement with the mass spectrometer measurements.

The global X_{Ar} for $P_{0Ar} = 5.4$ atm and 12.0 atm are 0.4 % and 0.8 % respectively. As in helium injection, a much richer fuel composition exists in the recirculation region [Figure 3-8 (b) and 3-9 (b)] than suggested by global X_{Ar} values. The X_{Ar} distribution obtained in the experiments is approximated to be the same as that of propane injected under identical test conditions. For $P_{0C_3H_8} = 5.4$ atm, the global $\phi_{C_3H_8} = 0.1$ and for $P_{0C_3H_8}$

= 12.0 atm, the global $\phi_{C_3H_8} = 0.2$. The global $\phi_{C_3H_8}$ values suggest a fuel lean mixture for both injection pressures. With the observation that $\phi_{C_3H_8} = 1$ corresponds to 4 % $X_{C_3H_8}$ in a propane-air mixture, it is seen in Figures 3-8 (b) and 3-9 (b) that for both injection pressures, the entire recirculation region and the main airflow shear layer is fuel-rich in composition, with $\phi_{C_3H_8} > 2$.

Upstream Injection

PLIF imaging of the recirculation region fuel distribution was performed for identical airflow and fuel injection conditions as the mass sampling experiments. For all test conditions, the PLIF signal was barely noticeable above the background. It is in agreement with mass spectrometer measurements and shows that hardly any fuel reaches the recirculation region for upstream injection.

Comparison between MS and PLIF data

The fuel mole fraction measurements at $x/H = 2.0$, $y/H = 0.3$, $z/W = 0.9$ obtained from PLIF and MS are compared in Figure 3-10 for base fuel injection of helium [Figure 3-10 (a)] and argon [Figure 3-10 (b)]. For PLIF, the fuel mole fractions obtained from unfiltered image and averaged over the mass sampling tube cross-section are reported. Filtering increased the fuel mole fraction by 10 % for helium and 2 % for argon injection, hence unfiltered data was used for comparison.

The PLIF and MS data do not overlap with each other for all test conditions. One of the reasons for the difference between PLIF and MS measurements is the intrusive nature of mass sampling for MS measurements. The outer diameter of the 3 inflow sampling tubes was 0.9 mm; the small diameter tubes were selected to minimize disturbances to the flow field. However, changes in the local flow field due to the presence of sampling tubes cannot be eliminated completely. A more significant disturbance in the local flow field

was caused by suction applied at the sampling port tip to extract gas mixture from the recirculation region into the mass spectrometer; the pressure gradient was high, with about 0.5 atm in the flow field behind the step and near vacuum at the entrance of the mass spectrometer. Hence, a difference between MS and PLIF data is expected due to different local flow fields in the two measurements.

As discussed in Chapter 2, the limitation of PLIF measurements is that acetone is expected to trace argon better than helium due to the difference in diffusion rates. Acetone diffuses about 4 times slower than helium and about the same rate as argon. Hence acetone PLIF measurements will over-estimate helium mole fraction in the flow. This is observed in the MS-PLIF data comparison; the difference between acetone PLIF fuel mole fraction measurements and corresponding MS measurements is higher for helium compared to argon.

The difference could also be due to a slight misalignment of the measurement point between the two techniques due to shaking of the test section as air flowed through it. The point at which PLIF and MS data are compared lies in the airflow shear layer. In this region, sharp gradients exist in the x - y plane, even though the flow is rather uniform in the z direction as seen in inflow MS measurements. The lateral test section movement observed by the camera during PLIF tests was 3 pixels ($\Delta y / H = 0.02$). For $P_{\text{OHe}} = 5.4$ atm and 12.0 atm test conditions, a lateral shift in measurement location from the reference point at $y/H = 0.3$ by $\Delta y / H = 0.02$ results in a 3 % change in fuel mole fraction. Hence shaking of the test section is not a significant reason for the difference between MS and PLIF data.

Table 3-1. Base fuel injection: global and local X_{He} .

$P_{0 He}$ (atm)	local X_{He} (%)	global X_{He} (%)	local / global X_{He}
Wall sampling			
5.4	1.1-3.8	1.1	0.9-3.4
12.0	2.6-8.3	2.5	1.0-3.4
Inflow sampling			
5.4	2.2-11.8	1.1	1.9-10.4
12.0	5.7-21.5	2.5	2.3-8.7

Table 3-2. Base fuel injection: global and local X_{Ar} .

$P_{0 Ar}$ (atm)	local X_{Ar} (%)	global X_{Ar} (%)	local / global X_{Ar}
Wall sampling			
5.4	2.0-5.0	0.4	5.5-13.9
12.0	3.8-9.9	0.8	4.9-12.7
Inflow sampling			
5.4	2.9-9.9	0.4	7.9-27.4
12.0	5.2-17.1	0.8	6.6-21.9

Table 3-3. Upstream fuel injection: global and local X_{He} .

$P_{0 He}$ (atm)	local X_{He} (%)	global X_{He} (%)	local / global X_{He}
Wall sampling			
2.4	0.2-0.3	0.7	0.3-0.5
5.1	0.3-0.4	1.5	0.2-0.3
Inflow sampling			
2.4	0.3-0.6	0.7	0.4-0.9
5.1	0.4-1.0	1.5	0.2-0.7

Table 3-4. Upstream fuel injection: global and local X_{Ar} .

$P_{0 Ar}$ (atm)	local X_{Ar} (%)	global X_{Ar} (%)	local / global X_{Ar}
Wall sampling			
2.4	0.7-0.9	0.2	3.3-4.0
5.1	0.8-1.0	0.5	1.7-2.0
Inflow sampling			
2.4	0.7-1.0	0.2	3.3-4.5
5.1	0.9-1.3	0.5	1.9-2.8

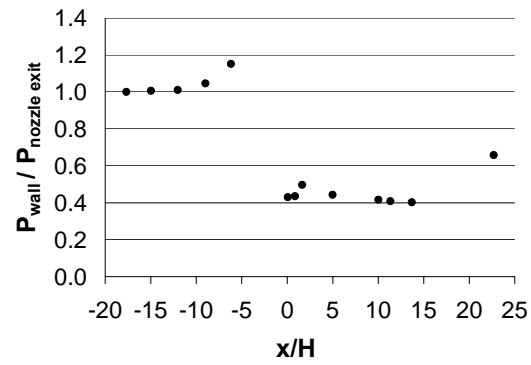


Figure 3-1. Wall pressure distribution for non-reacting flow. $P_{0\text{air}} = 4.8 \text{ atm}$, $M_{\text{air}} = 1.6$. The axial origin is placed at the step.

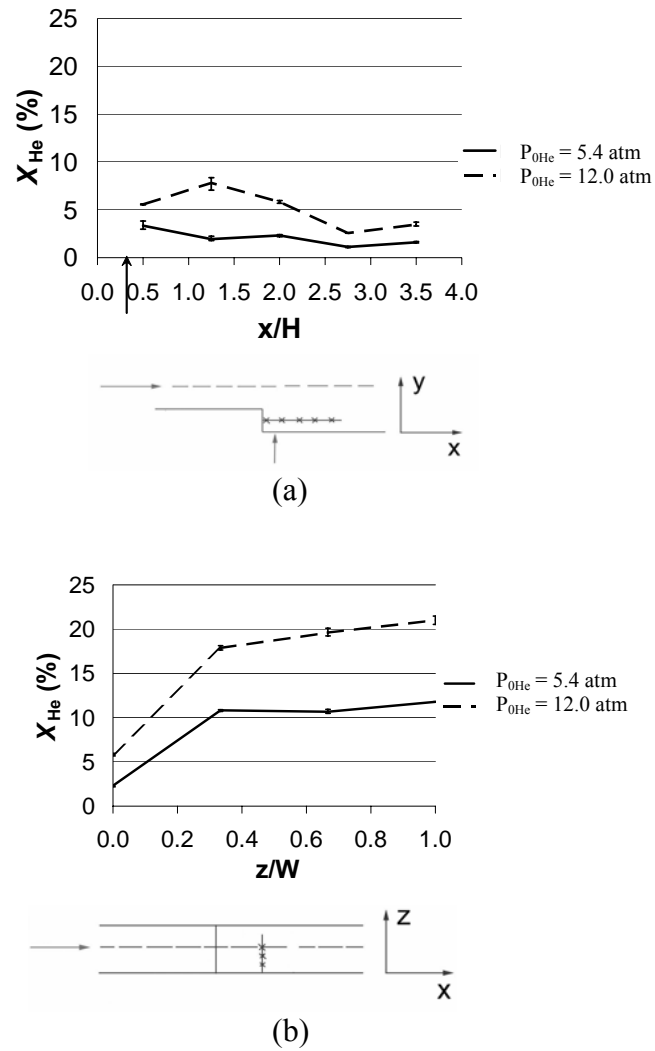


Figure 3-2. Base fuel injection: MS measurement of helium mole fraction distribution in the recirculation region for (a) wall sampling (b) inflow sampling. $P_{0air} = 4.8$ atm, $M_{air} = 1.6$.

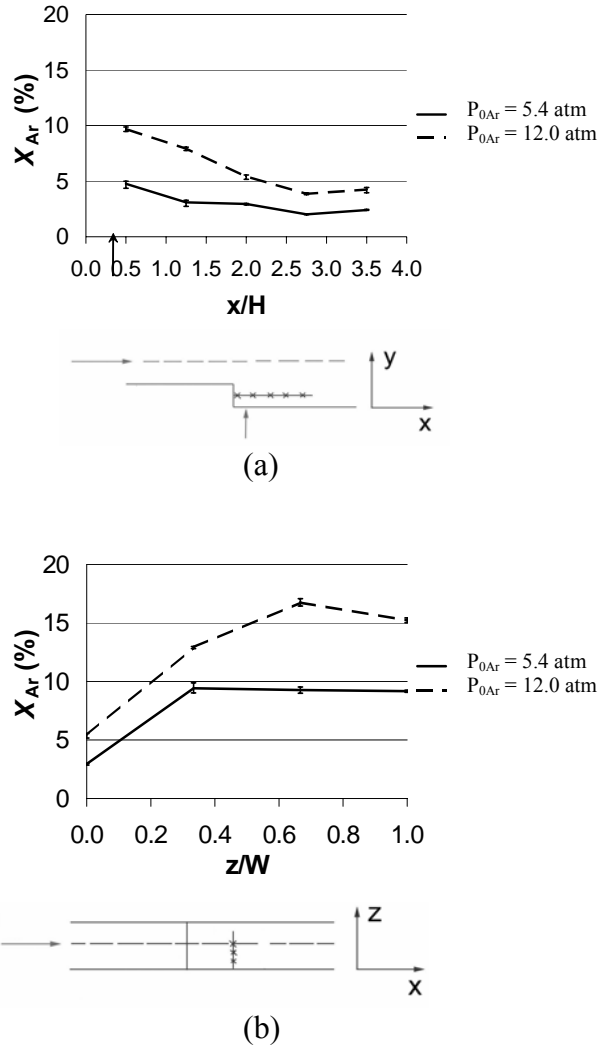


Figure 3-3. Base fuel injection: MS measurement of argon mole fraction distribution in the recirculation region for (a) wall sampling (b) inflow sampling. $P_{0air} = 4.8$ atm, $M_{air} = 1.6$.

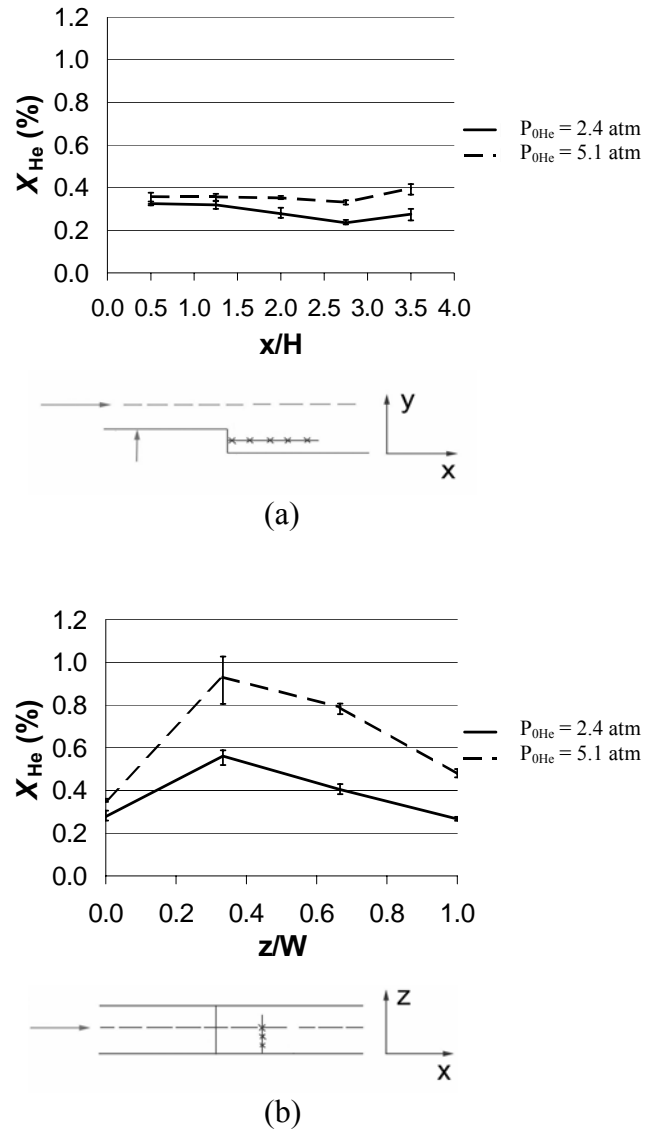
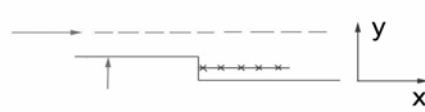
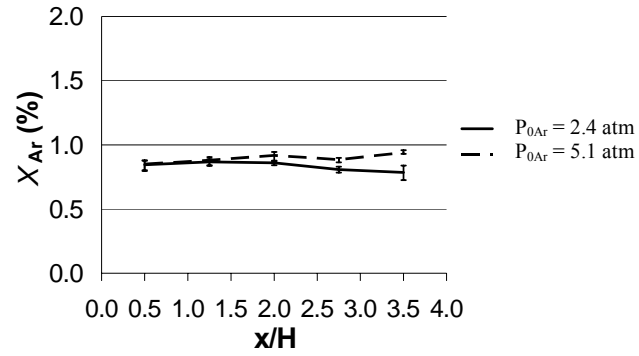
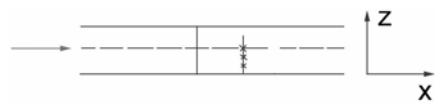
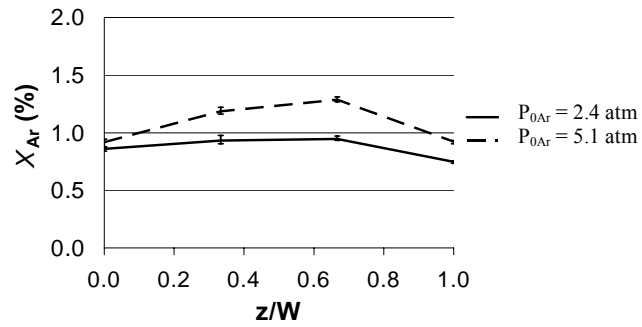


Figure 3-4. Upstream fuel injection: MS measurement of helium mole fraction distribution in the recirculation region for (a) wall sampling (b) inflow sampling. $P_{\text{Oair}} = 4.8$ atm, $M_{\text{air}} = 1.6$.



(a)



(b)

Figure 3-5. Upstream fuel injection: MS measurement of argon mole fraction distribution in the recirculation region for (a) wall sampling (b) inflow sampling. $P_{0air} = 4.8$ atm, $M_{air} = 1.6$.

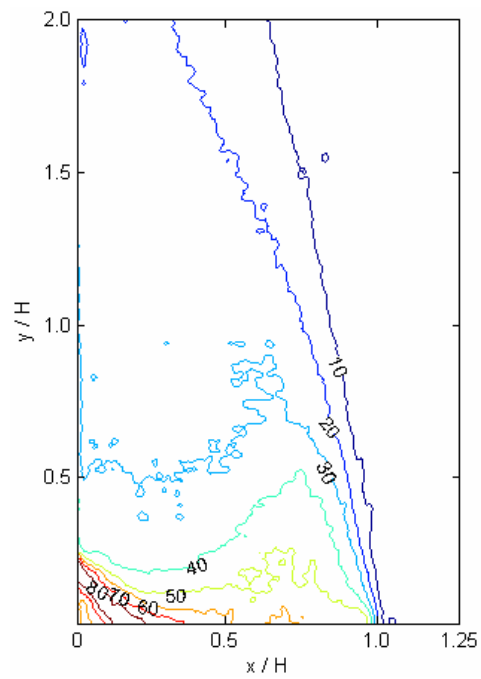
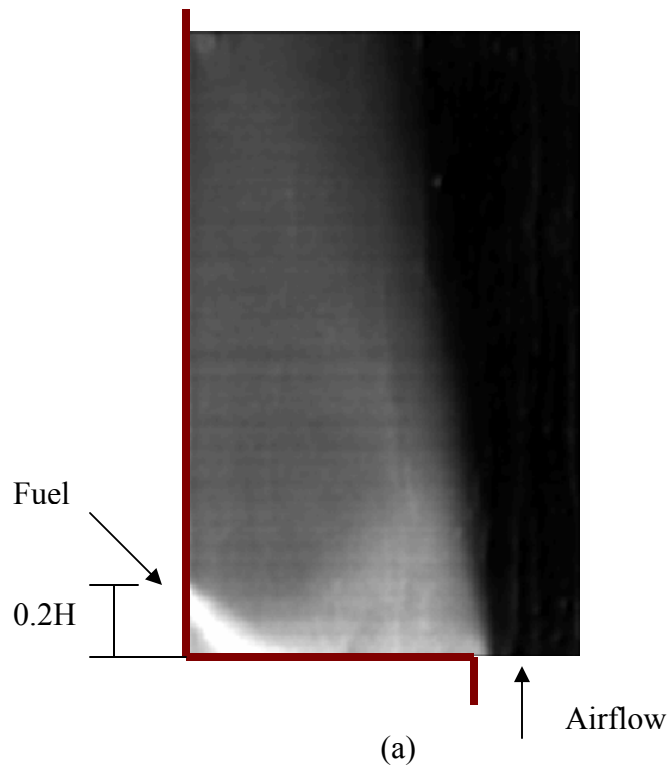


Figure 3-6. PLIF measurement for base injection of helium (a) image (b) X_{He} distribution (%). $P_{0He} = 5.4$ atm, $P_{0air} = 4.8$ atm, $M_{air} = 1.6$.

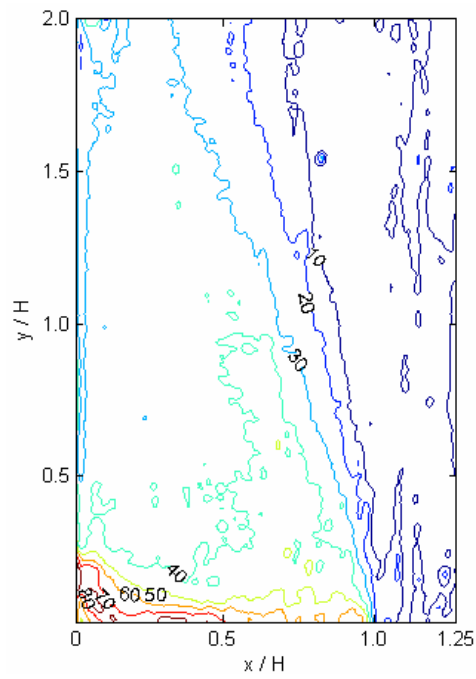
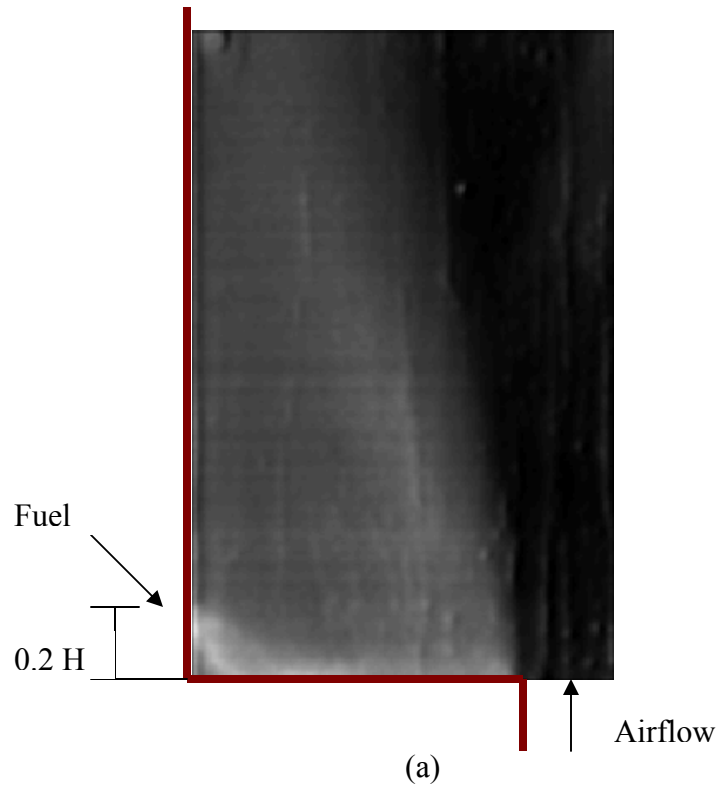


Figure 3-7. PLIF measurement for base injection of helium (a) image (b) X_{He} distribution (%). $P_{0\text{He}} = 12.0 \text{ atm}$, $P_{0\text{air}} = 4.8 \text{ atm}$, $M_{\text{air}} = 1.6$.

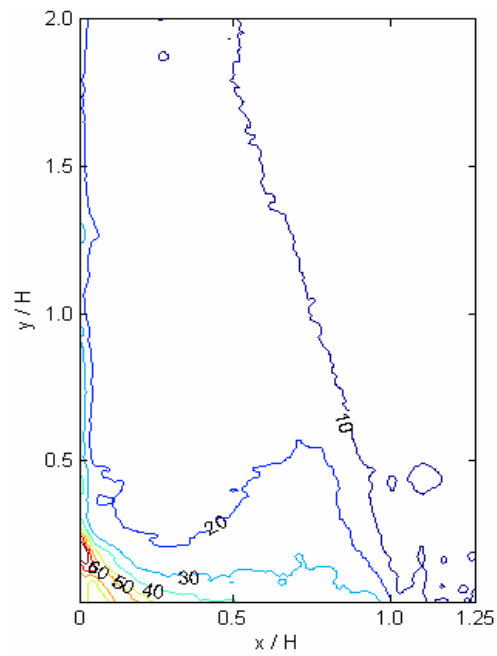
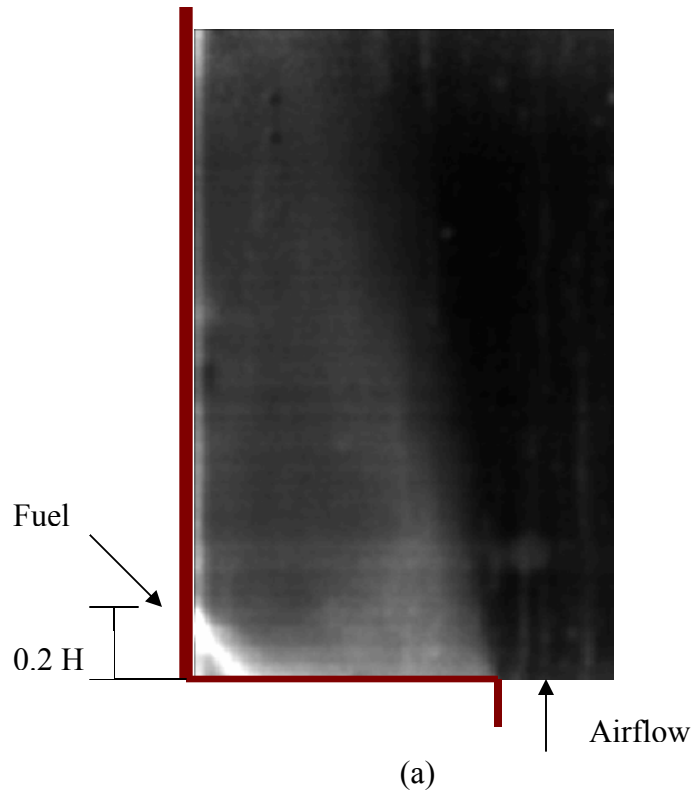


Figure 3-8. PLIF measurement for base injection of argon (a) image (b) X_{Ar} distribution (%). $P_{0Ar} = 5.4$ atm, $P_{0air} = 4.8$ atm, $M_{air} = 1.6$.

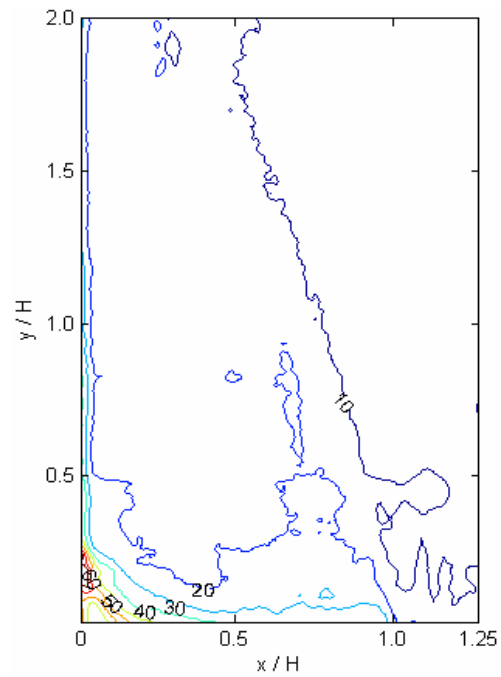
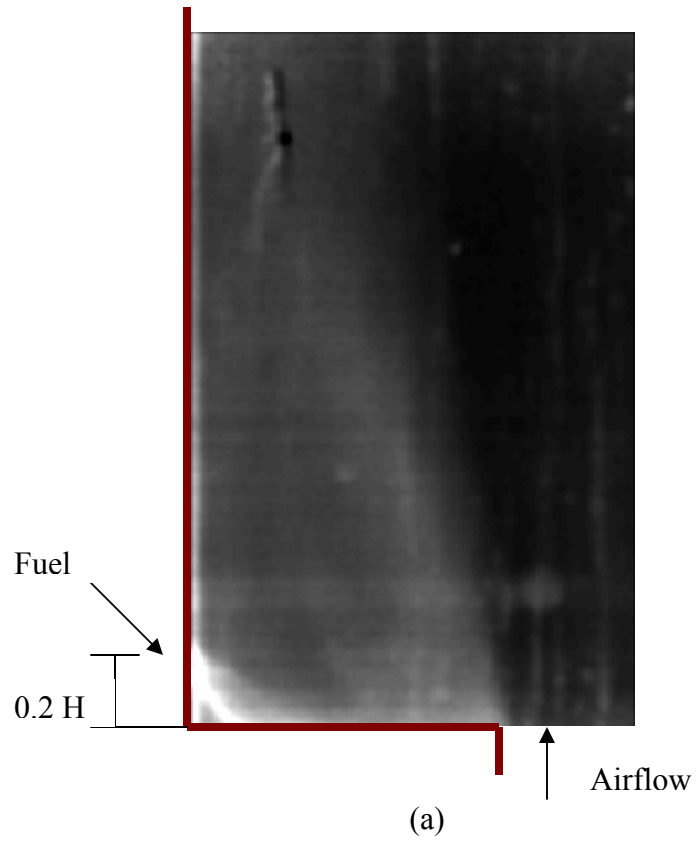
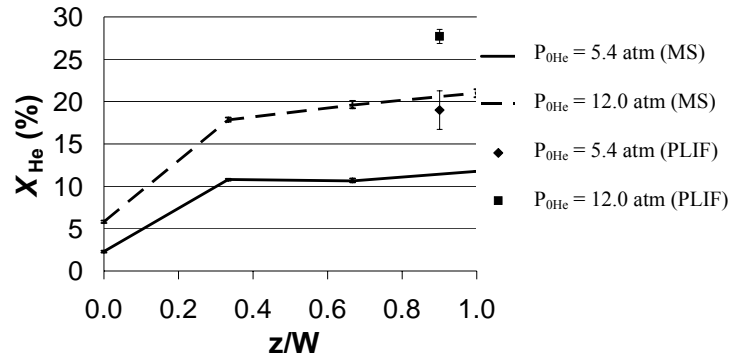
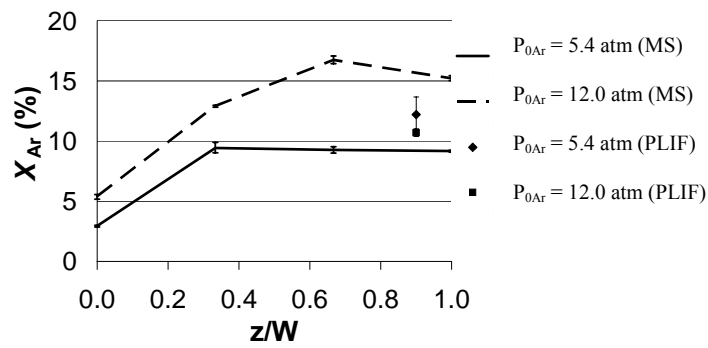


Figure 3-9. PLIF measurement for base injection of argon (a) image (b) X_{Ar} distribution (%). $P_{0Ar} = 12.0$ atm, $P_{0air} = 4.8$ atm, $M_{air} = 1.6$.



(a)



(b)

Figure 3-10. Comparison between MS and PLIF data for base fuel injection of (a) helium (b) argon.

CHAPTER 4 RESULTS: REACTING FLOW

The study included reacting cases with the air conditions maintained at $M = 1.6$, $T_{0\text{air}} = 300 \text{ K}$, $P_{0\text{air}} = 4.5 \text{ atm}$. Hydrogen was injected as fuel at two different pressures from the base of the step and from a location upstream of the step; the configuration is described in Chapter 2. The results are described below.

Base Injection: Hydrogen

Combustion experiments were performed with hydrogen injected at the base of the step. Mass sampling of the recirculation region species was done along the wall in the x -direction. Hydrogen was injected at two stagnation pressures: $P_{0\text{H}_2} = 4.5 \text{ atm}$ and $P_{0\text{H}_2} = 8.2 \text{ atm}$, the air stagnation pressure was $P_{0\text{air}} = 4.5 \text{ atm}$. These corresponded to global ϕ_{H_2} of 0.04 and 0.08 respectively. The wall pressure distribution for the two $P_{0\text{H}_2}$ is shown in Figure 4-1. For $P_{0\text{H}_2} = 4.5 \text{ atm}$, the expansion of airflow approaching the step is reduced due to heat released from combustion and pressure rise at the step base. Hence the recirculation region length is more than the corresponding non-reacting case. For $P_{0\text{H}_2} = 8.2 \text{ atm}$, the rather uniform pressure distribution due to more heat release implies an even longer recirculation region and probably no reattachment point for the shear layer. Figure 4-2 (a) shows the wall distribution of local ϕ_{H_2} in the recirculation region for $P_{0\text{H}_2} = 4.5 \text{ atm}$. Figure 4-3 (a) shows the corresponding plot for $P_{0\text{H}_2} = 8.2 \text{ atm}$. The local ϕ_{H_2} was deduced from the mole fractions of hydrogen and water in the product mixture. The fuel injection location is indicated on the horizontal axis in the plots. A highly non-uniform ϕ_{H_2} distribution is observed in the recirculation region with a maximum around $2.2H$. The

local ϕ_{H_2} goes up to 0.7 at $P_{\text{O}_2} = 4.5$ atm and up to 1.3 at $P_{\text{O}_2} = 8.2$ atm, showing a proportional increase due to an increase in P_{O_2} .

The wall distribution of products from hydrogen combustion for the two P_{O_2} is shown in Figures 4-2 (b) and 4-3 (b). X_{N_2} has not been included in the plots. Concurrent with the earlier observation of a fuel-rich mixture existing in the recirculation region, the combustion product composition shows a significant proportion of unburned hydrogen. $X_{\text{H}_2\text{O}}$ increases as we move downstream of the step. However a significant proportion of unburned oxygen and only a small proportion of water are a reflection of the limitation of sampling at the wall where the combustion radicals get quenched and hence the composition can be quite different from elsewhere in the flow.

Inflow mass sampling of the recirculation region species was done for the same airflow and fuel injection conditions as in wall sampling. Figures 4-4 and 4-5 show the distribution of local ϕ_{H_2} and product mole fractions in the recirculation region for $P_{\text{O}_2} = 4.5$ atm and $P_{\text{O}_2} = 8.2$ atm respectively. The experimental conditions were not identical over the repeated tests, both P_{O_2} and P_{O_2} varied by 0.3 atm. Hence the high standard deviations observed in the plots could be attributed to the change in recirculation region mixture composition due to changes in airflow and fuel injection conditions. The local ϕ_{H_2} distributions in Figures 4-4 (a) and 4-5 (a) show a decreasing amount of fuel as we go downstream of the fuel injection location. The local ϕ_{H_2} does not increase proportionally with the increase in P_{O_2} . As P_{O_2} increased, the local ϕ_{H_2} increased unevenly in the recirculation region; the region close to the injection location experienced a lower increase in ϕ_{H_2} than the region farther away in the x -direction. Thus, increasing P_{O_2} led to a reduction of local gradients in the recirculation region. The product mole fraction

distributions in Figures 4-4 (b) and 4-5 (b) show a fuel rich mixture in the recirculation region with plenty of unburned hydrogen and almost no oxygen. The proportion of unburned hydrogen drops rapidly as we go downstream in the recirculation region. For low P_{0H_2} , once the hydrogen was completely consumed, the oxygen mole fraction increased. For high P_{0H_2} , hydrogen was still present at the last sampling port and oxygen was virtually nonexistent. The temperature drop of the sampled mixture while passing through the cooling jacket resulted in condensation of water vapor and much of it could not reach the mass spectrometer. Hence the corrected X_{H_2O} was deduced from the oxygen deficit in the product mixture. Both corrected and uncorrected X_{H_2O} are plotted in the figures. Unlike the wall sampling experiments, significant amount of water was produced and X_{H_2O} increases as we go downstream in the recirculation region.

The local and global ϕ_{H_2} for the two P_{0H_2} obtained from wall and inflow samplings are compared in Table 4-1. As in the non-reacting flow test results discussed earlier, more fuel is observed away from the wall. For both P_{0H_2} , the local ϕ_{H_2} is an order of magnitude higher than the suggested global value.

Upstream Injection: Hydrogen

Hydrogen was injected upstream of the step for identical airflow conditions as base injection. Hydrogen was injected at two stagnation pressures: $P_{0H_2} = 2.5$ atm and $P_{0H_2} = 8.2$ atm. The corresponding dynamic pressure ratios [$P_{dynamic} = \rho_{H_2} V_{H_2}^2 / \rho_{air} V_{air}^2$] are 0.5 and 1.6 respectively. However, a flame could not be established for both P_{0H_2} , which is in line with the predictions of non-reacting flow experiments with helium injected upstream of the step. Mass sampling of the recirculation region species along the wall in x -direction showed a fuel-lean mixture with no water formed as a byproduct of combustion.

A change in the injection configuration, e.g., number of orifices, angled injection, etc., may lead to possibly holding the flame.

Table 4-1. Base fuel injection: global and local Φ_{H_2}

P_{0H_2} (atm)	local Φ_{H_2}	global Φ_{H_2}	local/global Φ_{H_2}
Wall sampling			
4.5	0.1-0.7	0.04	1.8-18.3
8.2	0.2-1.3	0.08	2.6-16.4
Inflow sampling			
4.5	0.8-2.7	0.04	21.0-66.5
8.2	1.5-2.8	0.08	18.5-35.0

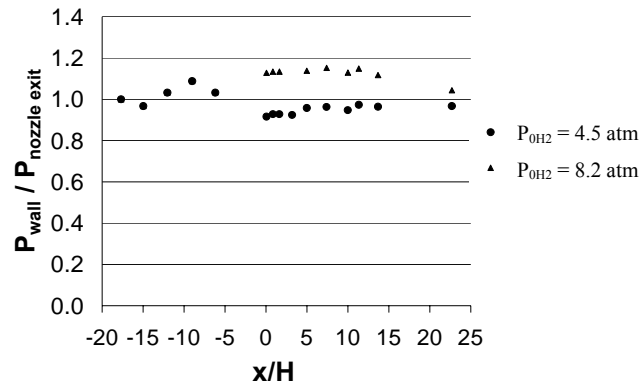
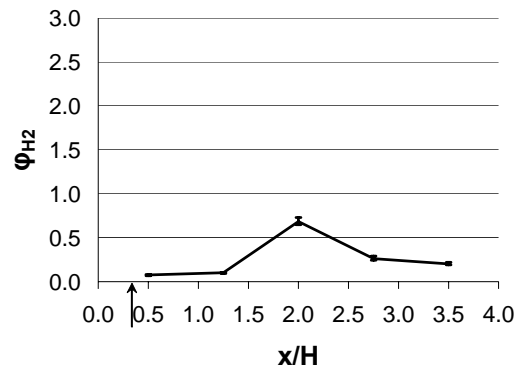
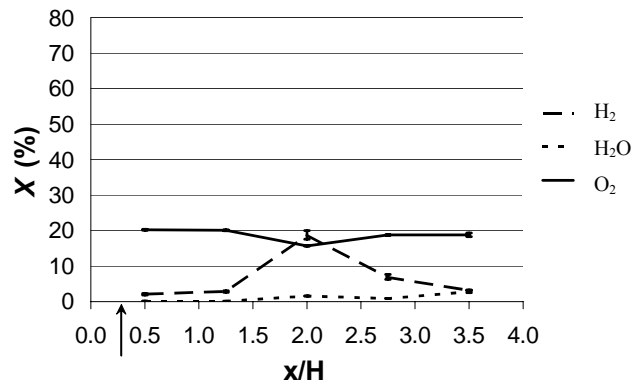


Figure 4-1. Wall pressure distribution for hydrogen combustion tests. $P_{\text{Oair}} = 4.5 \text{ atm}$, $M_{\text{air}} = 1.6$.



(a)



(b)

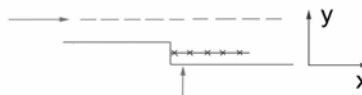
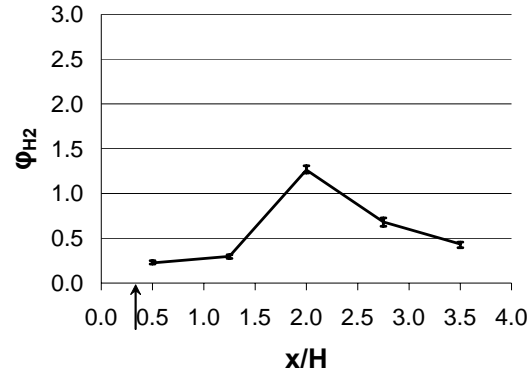
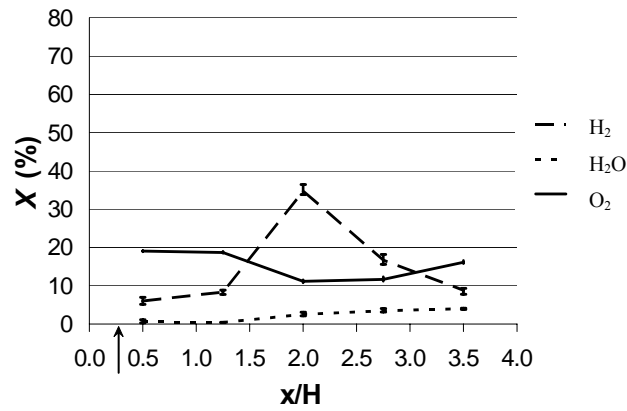


Figure 4-2. Base fuel injection: Wall sampling results for (a) hydrogen equivalence ratio distribution in the recirculation region (b) combustion species mole fraction distribution. $P_{O_{H_2}} = 4.5$ atm, $P_{O_{air}} = 4.5$ atm, $M_{air} = 1.6$.



(a)



(b)

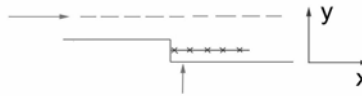


Figure 4-3. Base fuel injection: Wall sampling results for (a) hydrogen equivalence ratio distribution in the recirculation region (b) combustion species mole fraction distribution. $P_{O_{H_2}} = 8.2$ atm, $P_{O_{air}} = 4.5$ atm, $M_{air} = 1.6$.

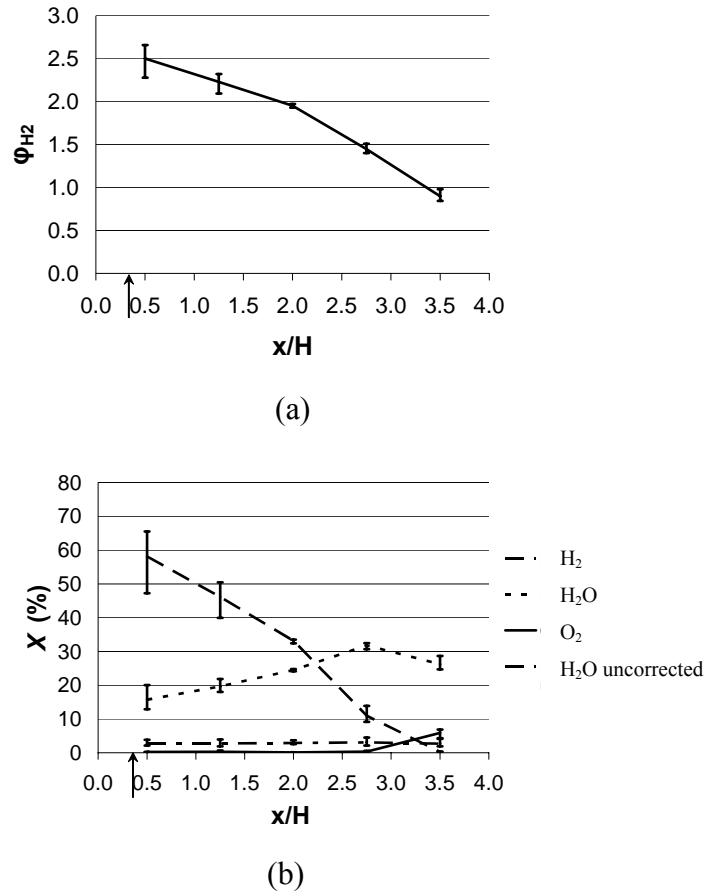
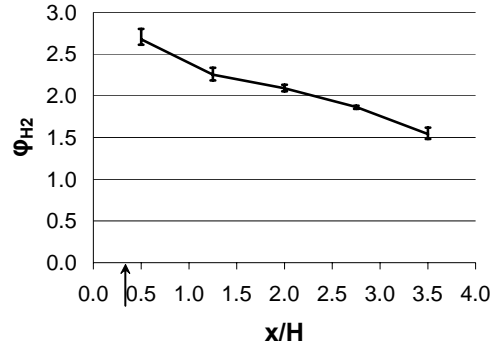
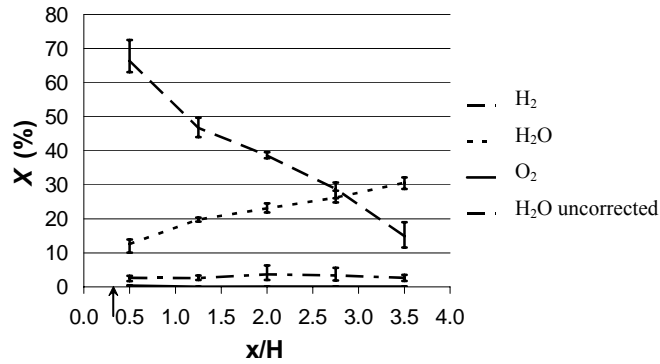


Figure 4-4. Base fuel injection: Inflow sampling results for (a) hydrogen equivalence ratio distribution in the recirculation region (b) combustion species mole fraction distribution. $P_{O_{H_2}} = 4.5$ atm, $P_{O_{air}} = 4.5$ atm, $M_{air} = 1.6$.



(a)



(b)

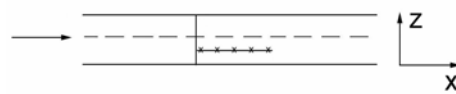


Figure 4-5. Base fuel injection: Inflow sampling results for (a) hydrogen equivalence ratio distribution in the recirculation region (b) combustion species mole fraction distribution. $P_{O_{H_2}} = 8.2$ atm, $P_{O_{air}} = 4.5$ atm, $M_{air} = 1.6$.

CHAPTER 5 CONCLUSIONS

Mass spectrometry (MS) and planar laser induced fluorescence (PLIF) were used to determine the species concentration distribution in the flameholding recirculation region and free shear layer formed behind a rectangular step in supersonic flow. Non-reacting and combustion tests were conducted and fuel related parameters such as the injection location, injection pressure and fuel type were varied. The conclusions are summarized below.

Fuel injection location:

- Fuel injection at the base of the step was effective in supplying fuel directly into the flameholding region. Stable flames were achieved in combustion tests.
- Fuel injection upstream of the step was not effective in supplying sufficient amount of fuel to the recirculation region, hence a flame could not be sustained in combustion tests. An injection configuration change, such as increasing the number of injection holes, could improve flameholding for upstream injection.

Fuel concentration in the recirculation region:

Base injection:

- The local fuel concentration in the recirculation region was an order of magnitude higher than the suggested global fuel mole fraction since only a small part of the main airflow entered the recirculation region. For combustion tests with hydrogen, the recirculation region was predominantly fuel-rich in composition even for quite low global ϕ_{H_2} .

- The above observation implies that for the same global equivalence ratio, the flameholding region is richer in fuel composition for non-premixed case compared to premixed case. As the global equivalence ratio is increased, the non-premixed case will flood the recirculation region with fuel and hence have worse fuel-rich flame stability limit than the premixed case. On the other hand, as the global equivalence ratio is reduced, the non-premixed case will still have sufficient fuel in the recirculation region and hence have a better fuel-lean stability limit than the premixed case.
- Non-reacting flow experiments indicated a leaner composition of the recirculation region than the combustion tests. It could be due to higher air entrainment rate into the recirculation region through the main airflow shear layer for non-reacting flow tests than combustion tests.
- For non-reacting and reacting flow tests, higher fuel concentration was measured inflow in the recirculation region than at the test section wall.

Fuel injection pressure:

Base injection:

- For non-reacting flow tests, fuel remained in the recirculation region and shear layer for both injection pressures. The fuel injection holes are inclined relative to the step base; such a configuration helps the fuel remain and mix within the recirculation region. Fuel distribution in the recirculation region was more non-uniform for higher fuel injection pressure.
- For combustion tests, increasing the fuel injection pressure resulted in reducing the fuel distribution gradient inflow in the recirculation region.

Upstream injection:

- The lighter gas, i.e. helium, penetrated through the airflow boundary layer along the wall for both injection pressures; the fuel quantity detected in the recirculation region was less than the suggested global value.
- At higher injection pressure for the heavier gas, i.e. argon, the jet penetrated through the airflow boundary layer and less of it was carried into the recirculation region. However, for both argon injection pressures, more fuel was detected in the recirculation region than the indicated global value.

*Fuel type:**Base injection:*

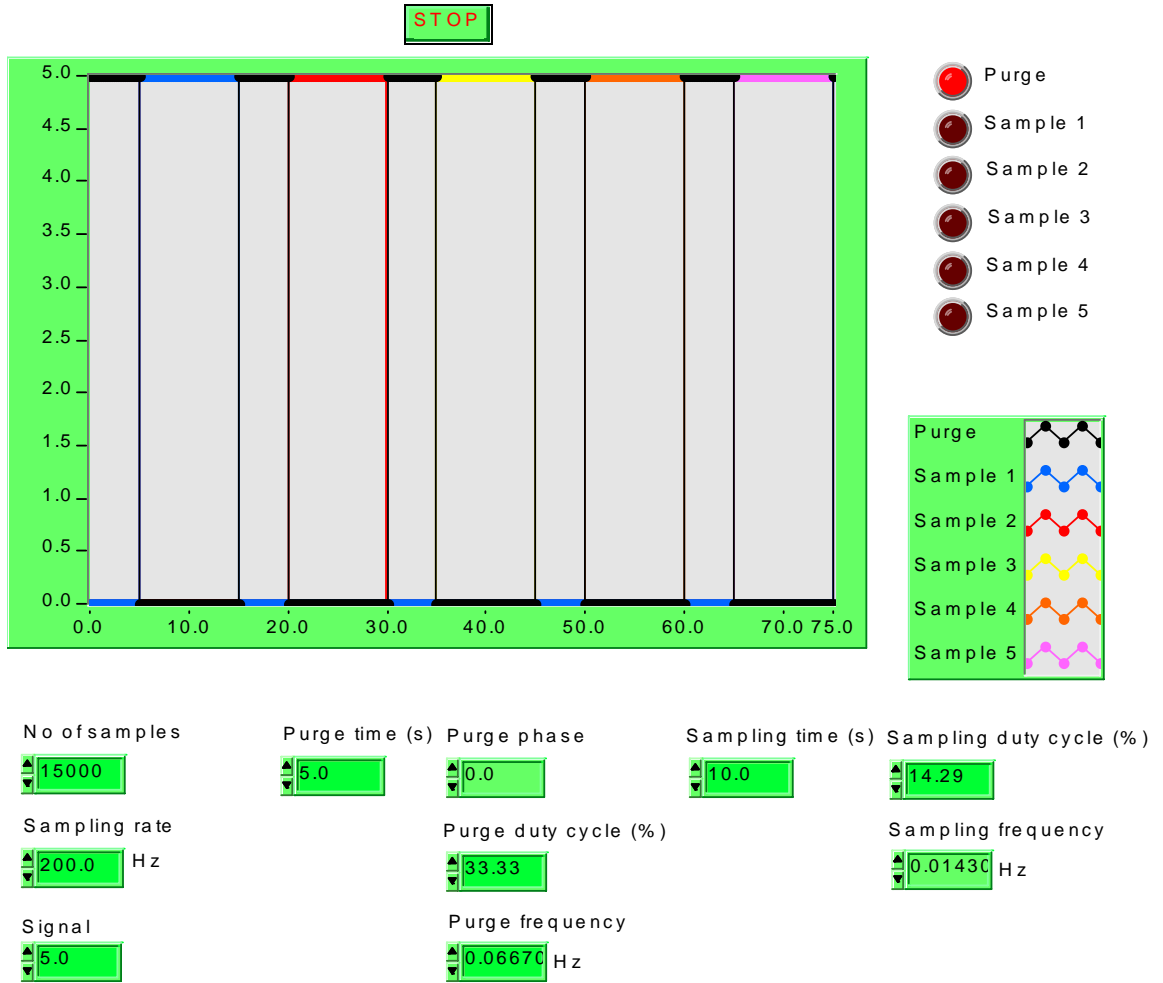
- The fuel distribution pattern in the recirculation region was similar for helium and argon. However, argon concentration in the recirculation region was higher than helium for a unit mole fraction of fuel injected in the test section. It could be due to slower diffusion rate of argon in air than that of helium in air.
- The above observation implies that as the fuel injection pressure is increased, the heavier fuel will have higher fuel mole fraction in the recirculation region, and hence have a worse fuel-rich flame stability limit, than the lighter fuel. For the same reason, as the injection pressure is decreased, the heavier fuel will still have enough fuel mole fraction in the recirculation region, and hence have a better fuel-lean flame stability limit, compared to the lighter fuel. This analysis is in addition to the fact that a heavier fuel such as propane has a much smaller flame stability curve than a lighter fuel such as hydrogen.

Comparison of MS and PLIF data:

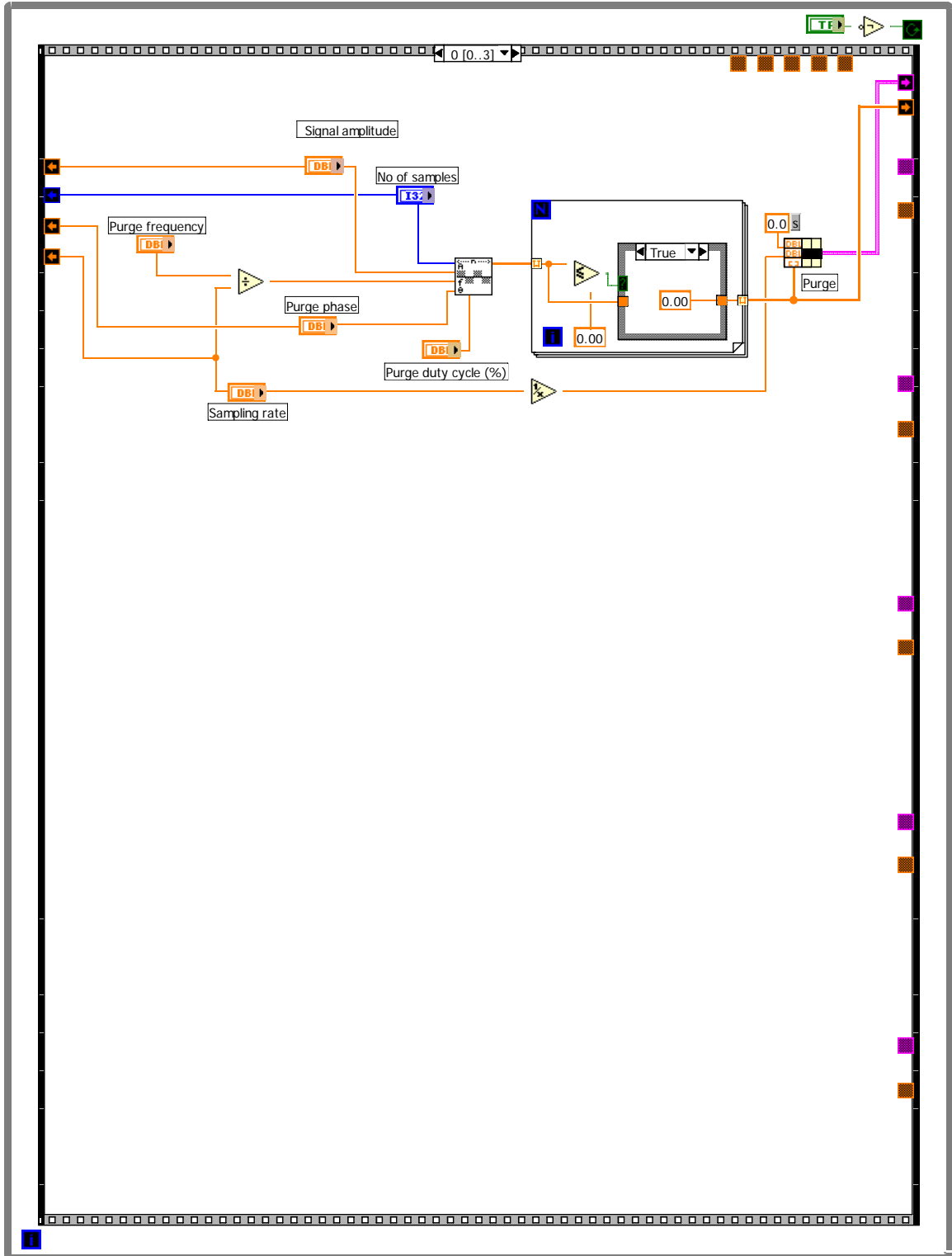
- The data from MS and PLIF at the common point in the recirculation region do not overlap with each other. This is in part due to the intrusive nature of mass sampling for MS measurements; the local flow fields in MS and PLIF experiments are not identical. Further, acetone PLIF over-estimates fuel mole fraction for helium compared to argon.

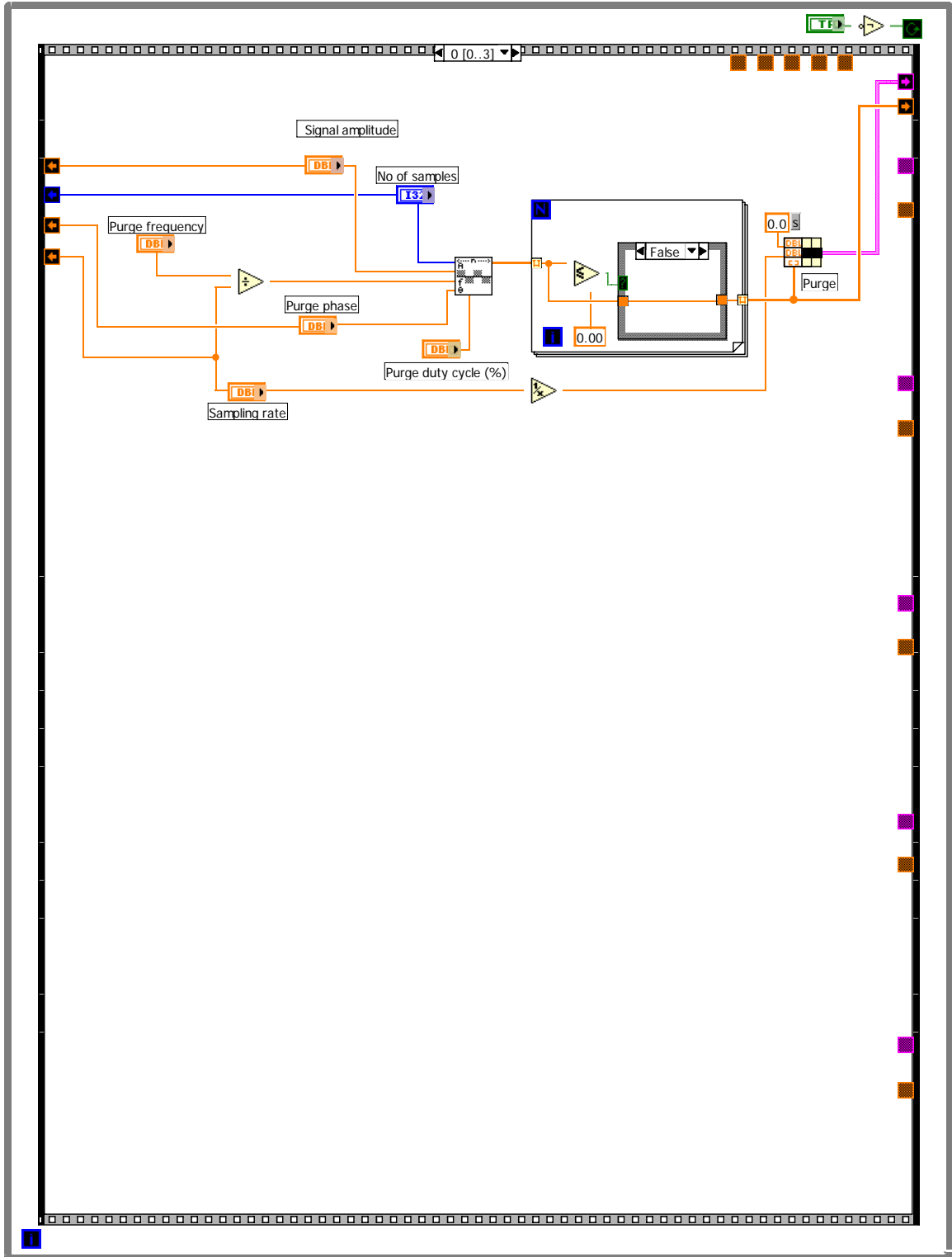
APPENDIX A LABVIEW PROGRAM FOR MASS SAMPLING SEQUENCING

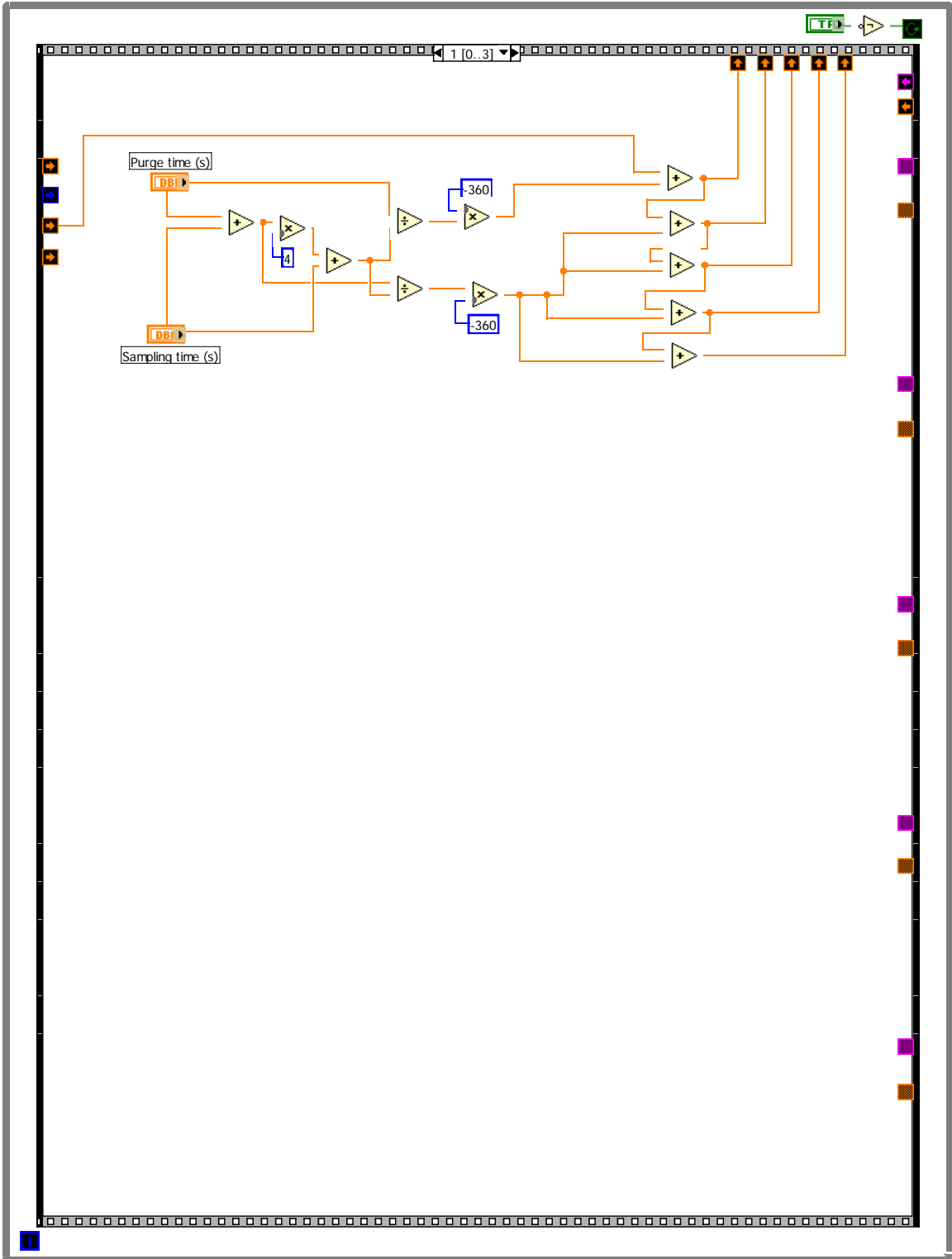
Front Panel

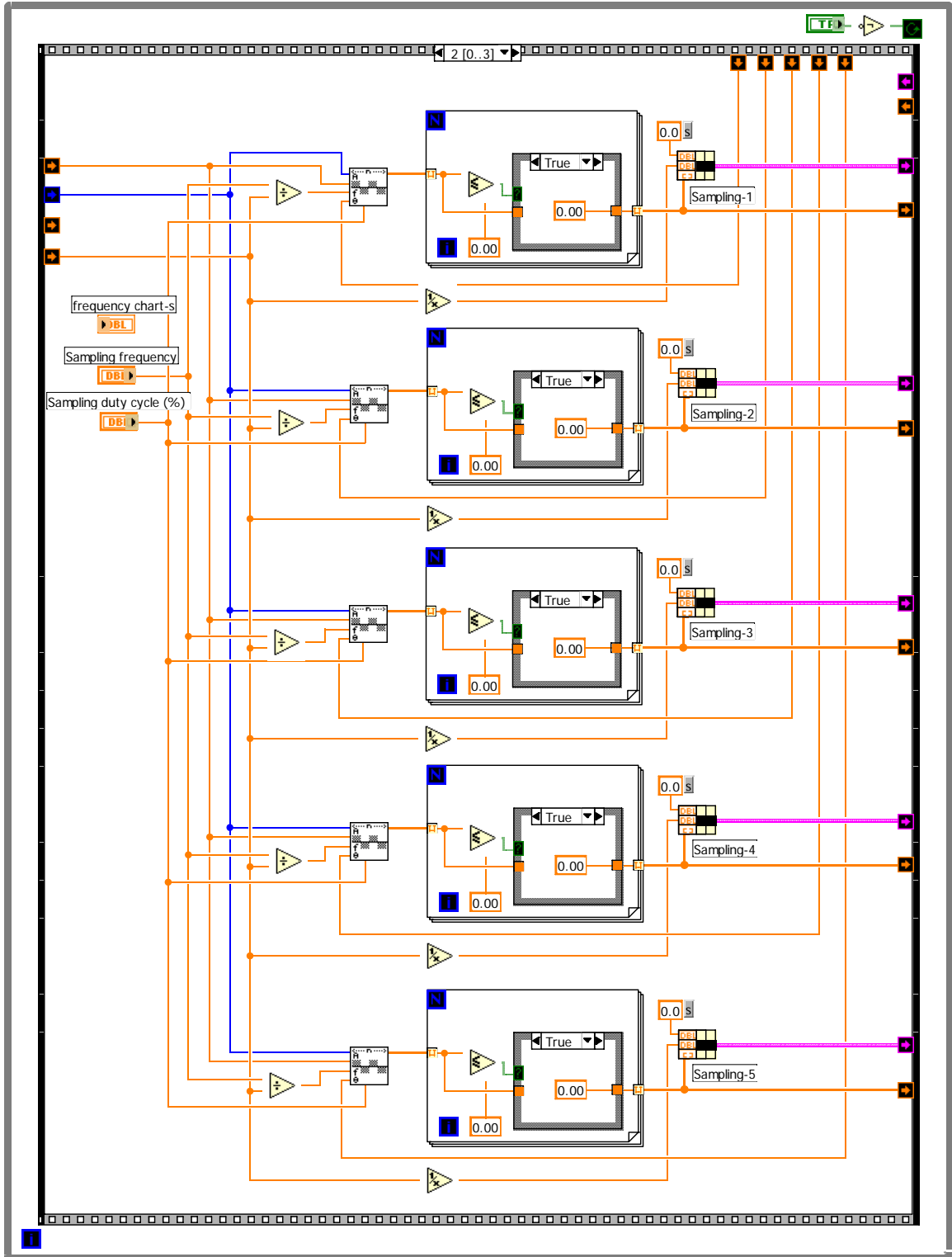


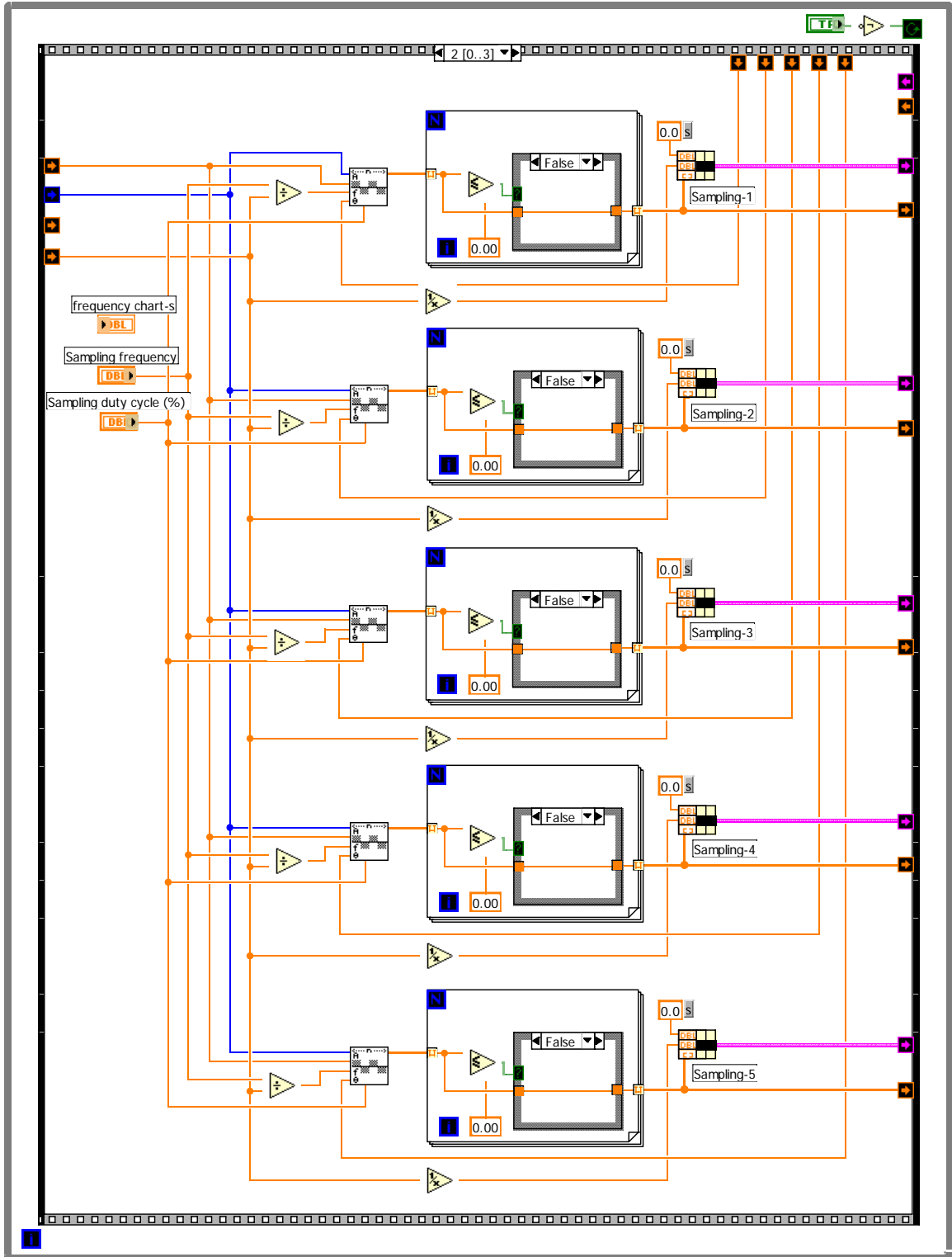
Block Diagram

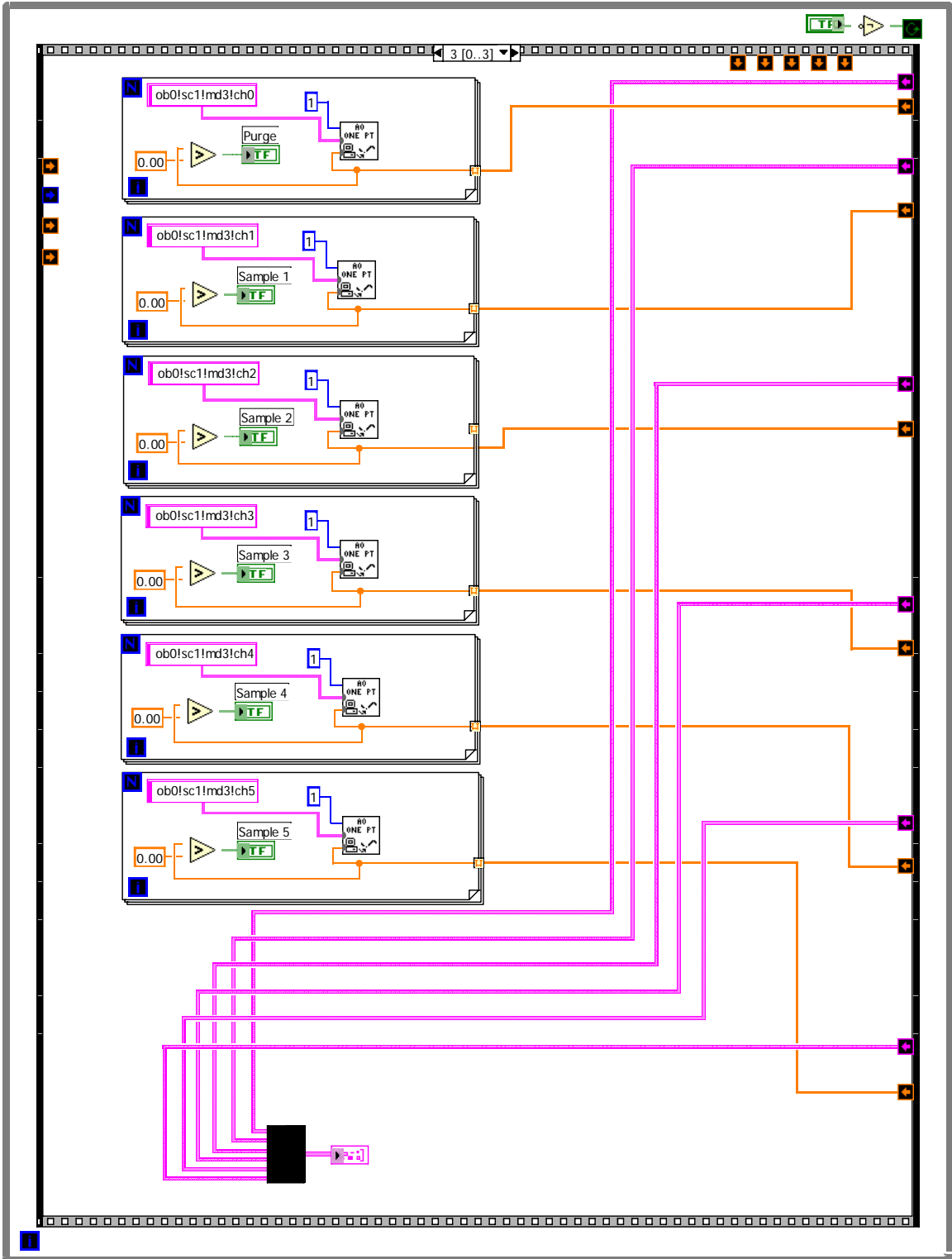












APPENDIX B
MATLAB PROGRAM FOR PLIF IMAGE PROCESSING

imbatchread.m

```
function [immean]=imbatchread(flnhdr)

%time averaging of a set of images

d=dir([flnhdr '*.tif']);

nFiles=length(d);

disp(['reading ' flnhdr ' batch - ' num2str(nFiles) ' files']);

imtot=double(imread(d(1).name));

for i=2:nFiles,

    im=double(imread(d(i).name));

    imtot=imtot+im;

    if floor(i/10)==i/10,

        disp(['read ' num2str(i) ' files']);

    end;

end;

immean=imtot/nFiles;

%image axes origin shift from top-left to bottom-left corner

[m,n]=size(immean);

for i=1:m/2,

    temp=immean(m-i+1,:);

    immean(m-i+1,:)=immean(i,:);
```

```
    immean(i,:)=temp;

end;

imageprocessing.m

%imageprocessing.m

%Image processing for DiCamPro image batches

laser='110805a'; %file name header of laser sheet file to use

run_A='110505h'; %file name header of experiment file to use

bgnd_A='110505i'; %file name header of background file to use

run_B='110505j'; %file name header of experiment file to use

bgnd_B='110505k'; %file name header of background file to use

run_C='110505l'; %file name header of experiment file to use

bgnd_C='110505m'; %file name header of background file to use

%time averaging of a set of images

[laserman]=imbatchread(laser);

[runmean_A]=imbatchread(run_A);

[bgndmean_A]=imbatchread(bgnd_A);

[runmean_B]=imbatchread(run_B);

[bgndmean_B]=imbatchread(bgnd_B);

[runmean_C]=imbatchread(run_C);

[bgndmean_C]=imbatchread(bgnd_C);

%background subtraction

runcorr1_A=runmean_A-bgndmean_A;

runcorr1_B=runmean_B-bgndmean_B;
```

```
runcorr1_C=runmean_C-bgndmean_C;

%laser sheet profile correction

[m,n]=size(runcorr1_A);

for i=1:n,

    runcorr2_A(:,i)=runcorr1_A(:,i)/lasermean(:,170)*max(lasermean(:,170));

end;

[m,n]=size(runcorr1_B);

for i=1:n,

    runcorr2_B(:,i)=runcorr1_B(:,i)/lasermean(:,170)*max(lasermean(:,170));

end;

[m,n]=size(runcorr1_C);

for i=1:n,

    runcorr2_C(:,i)=runcorr1_C(:,i)/lasermean(:,170)*max(lasermean(:,170));

end;

%fuel mole fraction distribution

%I1=861;%80psi

%I2=965;%80psi

%I3=905;%80psi

I1=669;%176psi

I2=718;%176psi

I3=523;%176psi

relconc_A=100*runcorr2_A/I1;

relconc_B=100*runcorr2_B/I2;
```

```
relconc_C=100*runcorr2_C/I3;
```

```
%plotting
```

```
figure(11);
```

```
Z=relconc_A;
```

```
contour(Z,10);
```

```
[C,h]=contour(Z,10);
```

```
clabel(C,h,'manual');
```

```
axis xy;
```

```
axis equal;
```

```
axis tight;
```

```
figure(12);
```

```
image(runcorr2_A/10);
```

```
colormap gray;
```

```
axis xy;
```

```
axis equal;
```

```
axis tight;
```

```
axis off;
```

```
figure(21);
```

```
Z=relconc_B;
```

```
contour(Z,10);
```

```
[C,h]=contour(Z,10);
```

```
clabel(C,h,'manual');
```

```
axis xy;
```

```
axis equal;
axis tight;
figure(22);
image(runcorr2_B/10);
colormap gray;
axis xy;
axis equal;
axis tight;
axis off;
figure(31);
Z=relconc_C;
contour(Z,10);
[C,h]=contour(Z,10);
clabel(C,h,'manual');
axis xy;
axis equal;
axis tight;
figure(32);
image(runcorr2_C/10);
colormap gray;
axis xy;
axis equal;
axis tight;
```

```

axis off;

%averaging, standard deviation of three repeatability tests

N=3;

Iavg=(I1+I2+I3)/N;

average=Iavg/100*(relconc_A+relconc_B+relconc_C)/N;

stddev=Iavg*(((average/Iavg-relconc_A/100).^2+(average/Iavg-
relconc_B/100).^2+(average/Iavg-relconc_C/100).^2)/(N-1)).^0.5;

stddev1=stddev./average;

stddev_av=100*mean(mean(stddev1(:,1:150)));

uncertainty=stddev_av*4.3/N^0.5;%95 percent confidence level

%fuel mole fraction at mass sampling location (x/H = 2.0, y/H = 0.3)

x=300;

y=45;

fuelmolefr=mean(mean(average(x-3:x+3,y-3:y+3)))/Iavg*100;

fuelmolefr_stddev=mean(mean(stddev1(x-3:x+3,y-3:y+3)))*100;

%filtering

filter=ones(3,3)/9;

average1=conv2(average,filter);

%fuel mole fraction distribution

%I_filtered=839;%80psi

I_filtered=564;%176psi

relconc=100*average1/I_filtered;

%plotting

```

```
figure(1);  
Z=relconc;  
[C,h]=contour(Z,[10 20 30 40 50 60 70 80]);  
clabel(C,h,'manual');  
axis xy;  
axis equal;  
axis tight;  
xlim([3 190]);  
ylim([3 300]);  
set(gca,'XTick',[3 75 150 190]);  
set(gca,'XTickLabel',{'0','0.5','1.0','1.25'});  
set(gca,'YTick',75:75:300);  
set(gca,'YTickLabel',{'0.5','1.0','1.5','2.0'});  
xlabel('x / H');  
ylabel('y / H');  
figure(2);  
image(average1/10);  
colormap gray;  
axis xy;  
axis equal;  
axis tight;  
axis off;  
figure(3);
```

```
image(average/10);
```

```
colormap gray;
```

```
axis xy;
```

```
axis equal;
```

```
axis tight;
```

```
axis off;
```

lasercharacterization.m

```
%lasercharacterization.m
```

```
laser_0min='012006a';
```

```
laser_40min='012006b';
```

```
laser_85min='012006c';
```

```
laser_0min_1='012006d';
```

```
%time averaging of a set of images
```

```
[lasermean_0min]=imbatchread(laser_0min);
```

```
[lasermean_40min]=imbatchread(laser_40min);
```

```
[lasermean_85min]=imbatchread(laser_85min);
```

```
[lasermean_0min_1]=imbatchread(laser_0min_1);
```

```
%laser sheet profile
```

```
[m,n]=size(lasermean_0min);
```

```
for i=1:m,
```

```
    lasermean_0min_1D(i)=lasermean_0min(i,175)/max(lasermean_0min(:,175));
```

```
end;
```

```
[m,n]=size(lasermean_40min);
```

```

for i=1:m,
    lasermean_40min_1D(i)=lasermean_40min(i,175)/max(lasermean_40min(:,175));
end;

[m,n]=size(lasermean_85min);
for i=1:m,
    lasermean_85min_1D(i)=lasermean_85min(i,175)/max(lasermean_85min(:,175));
end;

[m,n]=size(lasermean_0min_1);
for i=1:m,
    lasermean_0min_1_1D(i)=lasermean_0min_1(i,175)/max(lasermean_0min_1(:,175));
end;

%average, standard deviation
N=3;
average=(lasermean_0min_1D+lasermean_40min_1D+lasermean_85min_1D)/N;
stddev=(((average-lasermean_0min_1D).^2+(average-
lasermean_40min_1D).^2+(average-lasermean_85min_1D).^2)/(N-1)).^0.5;
stddev1=stddev./average;
stddev_av=100*mean(stddev1);

%plotting
figure(1);
plot(lasermean_0min_1D,'r');
hold on;
plot(lasermean_40min_1D,'b');

```

```
hold on;

plot(laserman_85min_1D,'g');

hold on;

plot(laserman_0min_1_1D,'k');

axis xy;

xlim([1 320]);

ylim([0 1]);

xlabel('x / H');

ylabel('I / I max');

set(gca,'XTick',0:80:320);

set(gca,'XTickLabel',{'0','0.5','1.0','1.5','2.0'});

legend('t = 0min','t = 40min','t = 85min','t = 0min (repeat)');
```

LIST OF REFERENCES

- ¹ Curran E. T., "Scramjet engines: the first forty years," *Journal of Propulsion and Power*, Vol. 17 (6), pp. 1138-1148, 2001.
- ² Billig F. S., "Research on supersonic combustion," *Journal of Propulsion and Power*, Vol. 9 (4), pp. 499-514, 1993.
- ³ Marren D., Lewis M. and Maurice L. Q., "Experimentation, test and evaluation requirements for future air breathing hypersonic systems," *Journal of Propulsion and Power*, Vol. 17 (6), pp. 1361-1365, 2001.
- ⁴ Kumar A., Drummond J. P., McClinton C. R. and Hunt J. L., "Research in hypersonic airbreathing propulsion at the NASA Langley research center," *15th International Symposium on Airbreathing Engines*, ISABE-2001-1007, 2001.
- ⁵ Rodriguez C. G., "Computational fluid dynamics analysis of the Central Institute of Aviation Motors/NASA scramjet," *Journal of Propulsion and Power*, Vol. 19 (4), pp. 547-555, 2003.
- ⁶ Ben-Yakar A. and Hanson R. K., "Cavity flame-holders for ignition and flame stabilization in scramjets: an overview," *Journal of Propulsion and Power*, Vol. 17 (4), pp. 869-877, 2001.
- ⁷ Gruber M. R., Baurle R. A., Mathur T. and Hsu K. Y., "Fundamental studies of cavity-based flameholder concepts for supersonic combustors," *Journal of Propulsion and Power*, Vol. 17 (1), pp. 146-153, 2001.
- ⁸ Ali M. C. and Kurian J., "Cavity-based injections into supersonic flow," *Journal of Propulsion and Power*, Vol. 21 (6), pp. 1130-1132, 2005.
- ⁹ Mathur T., Gruber M., Jackson K., Donbar J., Donaldson W., Jackson T. and Billig F., "Supersonic combustion experiments with a cavity-based fuel injector," *Journal of Propulsion and Power*, Vol. 17 (6), pp. 1305-1312, 2001.
- ¹⁰ Yu K. H., Wilson K. J. and Schadow K. C., "Effect of flame-holding cavities on supersonic combustion performance," *Journal of Propulsion and Power*, Vol. 17 (6), pp. 1287-1295, 2001.

- ¹¹ Yu G., Li J. G., Chang X. Y., Chen L. H. and Sung C. J., "Fuel injection and flame stabilization in a liquid-kerosene-fueled supersonic combustor," *Journal of Propulsion and Power*, Vol. 19 (5), pp. 885-893, 2003.
- ¹² Owens M. G., Tehranian S., Segal C. and Vinogradov V. A., "Flameholding configurations for kerosene combustion in a Mach 1.8 airflow," *Journal of Propulsion and Power*, Vol. 14 (4), pp. 456-461, 1998.
- ¹³ Davis D. L. and Bowersox R. D., "Stirred reactor analysis of cavity flameholders for scramjets," *AIAA Paper*, AIAA-1997-3274, 1997.
- ¹⁴ Brandstetter A., Denis S. R., Kau H. P. and Rist D., "Flame stabilization in supersonic combustion," *AIAA Paper*, AIAA-2002-5224, 2002.
- ¹⁵ Northam G. B., Trexler C. A. and McClinton C. R., "Flameholding characteristics of a swept-strut H₂ fuel-injector for scramjet applications," *17th JANNAF Combustion Meeting*, pp. 489-507, 1980.
- ¹⁶ Lyubar A., Sander T. and Sattelmayer T., "Novel two stage injector for hydrogen flame stabilization in supersonic airflow," *AIAA Paper*, AIAA-2002-17_5229, 2002.
- ¹⁷ Gerlinger P. and Bruggermann D., "Numerical investigation of hydrogen strut injections into supersonic airflows," *Journal of Propulsion and Power*, Vol. 16 (1), pp. 22-28, 2000.
- ¹⁸ Tabejamaat S., Kobayashi H. and Niioka T., "Numerical and experimental studies of injection modeling for supersonic flameholding," *Journal of Propulsion and Power*, Vol. 21 (3), pp. 504-511, 2005.
- ¹⁹ Gruenig C., Avrashkov V. and Mayinger F., "Fuel injection into a supersonic airflow by means of pylons," *Journal of Propulsion and Power*, Vol. 16 (1), pp. 29-34, 2000.
- ²⁰ Gruenig C., Avrashkov V. and Mayinger F., "Self-ignition and supersonic reaction of pylon-injected hydrogen fuel," *Journal of Propulsion and Power*, Vol. 16 (1), pp. 35-40, 2000.
- ²¹ Huh H. and Driscoll J. F., "Shock wave enhancement of the mixing and the stability limits of supersonic hydrogen-air jet flames," *26th Symposium on Combustion / The Combustion Institute*, pp. 2933-2939, 1996.
- ²² Dimotakis P. E., "Turbulent free shear layer mixing and combustion," *High-speed Flight Propulsion Systems - Progress in Aeronautics and Astronautics*, Vol. 137, pp. 265-340, 1991.
- ²³ Pitz R. W. and Daily J. W., "Combustion in a turbulent mixing layer formed at a rearward-facing step," *AIAA Journal*, Vol. 21 (11), pp. 1565-1570, 1983.

- ²⁴ Ozawa R. I., Survey of basic data on flame stabilization and propagation for high speed combustion systems, *Airforce Technical Report*, AFAPL-TR-70-81, The Marquardt Company, 1971.
- ²⁵ Huellmantel L. W., Ziemer R. W. and Cambel A. B., "Stabilization of premixed propane-air flames in recessed ducts," *Journal of Jet Propulsion*, pp. 31-43, Jan 1957.
- ²⁶ Baxter M. R. and Lefebvre A. H., "Flame stabilization in high-velocity heterogeneous fuel-air mixtures," *Journal of Propulsion and Power*, Vol. 8 (6), pp. 1138-1143, 1992.
- ²⁷ Baxter M. R. and Lefebvre A. H., "Weak extinction limits of large-scale flameholders," *Journal of Engineering for Gas Turbines and Power – Transactions of the ASME*, Vol. 114, pp. 776-782, 1992.
- ²⁸ Niioka T., Terada K., Kobayashi H. and Hasegawa S., "Flame stabilization characteristics of strut divided into two parts in supersonic flow," *Journal of Propulsion and Power*, Vol. 11 (1), pp. 112-116, 1995.
- ²⁹ Zakkay V., Sinha R. and Meddecki H., "Residence time within a wake recirculation region in an axisymmetric supersonic flow," *Astronautica Acta*, Vol. 16, pp. 201-216, 1971.
- ³⁰ Driscoll J. F. and Rasmussen C. C., "Correlation and analysis of blowout limits of flames in high-speed airflows," *Journal of Propulsion and Power*, Vol. 21 (6), pp. 1035-1044, 2005.
- ³¹ Rasmussen C. C., Driscoll J. F., Hsu K. Y., Donbar J. M., Gruber M. R. and Carter C. D., "Stability limits of cavity-stabilized flames in supersonic flow," *Proceedings of the Combustion Institute*, Vol. 30, pp. 2825-2833, 2005.
- ³² Winterfeld G., "Stabilization of hydrogen-air flames in supersonic flow," *Modern Research Topics in Aerospace Propulsion*, pp. 37-47, 1991.
- ³³ Rasmussen C. C., Driscoll J. F., Carter C. D. and Hsu K. Y., "Characteristics of cavity-stabilized flames in a supersonic flow," *Journal of Propulsion and Power*, Vol. 21 (4), pp. 765-768, 2005.
- ³⁴ Hsu K. Y., Carter C., Crafton J., Gruber M., Donbar J., Mathur T., Schommer D. and Terry W., "Fuel distribution about a cavity flameholder in supersonic flow," *AIAA Paper*, AIAA-2000-3585, 2000.
- ³⁵ Gruber M. R., Donbar J. M., Carter C. D. and Hsu K. Y., "Mixing and combustion studies using cavity based flameholders in a supersonic flow," *Journal of Propulsion and Power*, Vol. 20 (5), pp. 769-778, 2004.

- ³⁶ Uchiumi M., Kobayashi H., Hasegawa S. and Niioka T., "Experiments on the flameholding mechanism of a newly devised strut in supersonic airflow," *IUTAM Symposium on Combustion in Supersonic Flows*, pp. 135-144, 1997.
- ³⁷ Zamma Y., Shiba H., Masuya G., Tomioka S., Hiraiwa T. and Mitani T., "Similarity parameters of pre-ignition flowfields in a supersonic combustor," *AIAA Paper*, AIAA-1997-2890, 1997.
- ³⁸ Tomioka S., Hiraiwa T., Mitani T., Zamma Y., Shiba H. and Masuya G., "Auto ignition in a supersonic combustor with perpendicular injection behind backward-facing step," *AIAA Paper*, AIAA-1997-2889, 1997.
- ³⁹ Masuya G., Kudou K., Murakami A., Komuro T., Tani K., Kanda T., Wakamatsu Y., Chinzei N., Sayama M., Ohwaki K. and Kimura I., "Some governing parameters of plasma torch igniter/flameholder in a scramjet combustor," *Journal of Propulsion and Power*, Vol. 9 (2), pp. 176-181, 1993.
- ⁴⁰ Thayer W. J. and Corlett R. C., "Gas dynamic and transport phenomena in the two-dimensional jet interaction flowfield," *AIAA Journal*, Vol. 10 (4), pp. 488-493, 1972.
- ⁴¹ McDaniel J., Fletcher D., Hartfield R. and Hollo S., "Staged transverse injection into Mach 2 flow behind a rearward-facing step: a 3-D compressible test case for hypersonic combustor code validation," *AIAA Paper*, AIAA-1991-5071, 1991.
- ⁴² Strokin V. and Grachev V., "Possible scheme of flameholding in hydrogen fueled scramjet combustors," *Proceeding of 1st International Aerospace Congress*, Vol. 1, pp. 630-633, 1997.
- ⁴³ Ogorodnikov D. A., Vinogradov V. A., Shikhman Y. M. and Strokin V. Y., "Russian research on experimental hydrogen-fueled dual-mode scramjet: conception and preflight tests," *Journal of Propulsion and Power*, Vol. 17 (5), pp. 1041-1048, 2001.
- ⁴⁴ Morrison C. Q., Campbell R. L., Edelman R. B. and Jaul W. K., "Hydrocarbon fueled dual mode ramjet/scramjet concept evaluation," *Proceedings of the International Society for Air-breathing Engines*, ISABE-1997-7053, pp. 348-356, 1997.
- ⁴⁵ Kim C. K., Yu S. T. and Zhang Z. C., "Cavity flow in scramjet engine by space-time conservation and solution element method," *AIAA Journal*, Vol. 42 (5), pp. 912-919, 2004.
- ⁴⁶ Correa S. M. and Warren R. E., "Supersonic sudden-expansion flow with fluid injection: an experimental and computational study," *AIAA Paper*, AIAA-1989-0389, 1989.

- ⁴⁷ Glawe D. D., Donbar J. M., Nejad A. S., Sekar B., Chen T. H., Samimy M. and Driscoll J. F., "Parallel fuel injection from the base of an extended strut into supersonic flow," *AIAA Paper*, AIAA-1994-0711, 1994.
- ⁴⁸ Mitani T., Takahashi M., Tomioka S., Hiraiwa T. and Tani K., "Analyses and application of gas sampling to scramjet engine testing," *Journal of Propulsion and Power*, Vol. 15, No. 4, 1999.
- ⁴⁹ Chinzei N., Komuro T., Kudou K., Murakami A., Tani K., Masuya G. and Wakamatsu Y., "Effects of injector geometry on scramjet combustor performance," *Journal of Propulsion and Power*, Vol. 9 (1), pp. 146-152, 1993.
- ⁵⁰ Masuya G., Komuro T., Murakami A., Shinozaki N., Nakamura A., Murayama M. and Ohwaki K., "Ignition and combustion performance of scramjet combustors with fuel injection struts," *Journal of Propulsion and Power*, Vol. 11 (2), pp. 301-307, 1995.
- ⁵¹ Ciezki H. K., Scheel F. and Kwan W., "Investigation of the combustion process in a scramjet model combustor with a sampling probe system," *AIAA Paper*, AIAA-2004-4166, 2004.
- ⁵² Rogers R. C., "A study of the mixing of hydrogen injected normal to a supersonic airstream," *NASA Technical Note*, NASA TN D-6114, 1971.
- ⁵³ Ng W. F., Kwok F. T. and Ninnemann T. A., "A concentration probe for the study of mixing in supersonic shear flows," *AIAA Paper*, AIAA-1989-2459, 1989.
- ⁵⁴ Cox S. K., Fuller R. P., Schetz J. A. and Walters R. W., "Vortical interactions generated by an injector array to enhance mixing in supersonic flow," *AIAA Paper*, AIAA-1994-0708, 1994.
- ⁵⁵ Hanson R. K., Seitzman J. M. and Paul P. H., "Planar laser-fluorescence imaging of combustion gases," *Applied Physics B*, Vol. 50, pp. 441-454, 1990.
- ⁵⁶ Schulz C. and Sick V., "Tracer-LIF diagnostics: quantitative measurement of fuel concentration, temperature and fuel-air ratio in practical combustion systems," *Progress in Energy and Combustion Science*, Vol. 31, pp. 75-121, 2005.
- ⁵⁷ Fox J. S., Houwing A. F., Danehy P. M., Gaston M. J., Mudford N. R. and Gai S. L., "Mole fraction-sensitive imaging of hypermixing shear layers," *Journal of Propulsion and Power*, Vol. 17 (2), pp. 284-292, 2001.
- ⁵⁸ Hartfield R. J., Abbitt J. D. and McDaniel J. C., "Injectant mole fraction imaging in compressible mixing flows using planar laser induced iodine fluorescence," *Optics Letters*, Vol. 14 (16), pp. 850-852, 1989.

- ⁵⁹ Abbitt J. D., Hartfield R. J. and McDaniel J. C., "Mole fraction imaging of transverse injection in a ducted supersonic flow," *AIAA Journal*, Vol. 29 (3), pp. 431-435, 1991.
- ⁶⁰ Hollo S. D., McDaniel J. C. and Hartfield R. J., "Quantitative investigation of compressible mixing: staged transverse injection into Mach 2 flow," *AIAA Journal*, Vol. 32 (3), pp. 528-534, 1994.
- ⁶¹ Hartfield R. J., Hollo S. D. and McDaniel J. C., "Experimental investigation of a supersonic swept ramp injector using laser induced iodine fluorescence," *Journal of Propulsion and Power*, Vol. 10 (1), pp. 129-135, 1994.
- ⁶² Lozano A., Yip B. and Hanson R. K., "Acetone: a tracer for concentration measurements in gaseous flows by planar laser-induced fluorescence," *Experiments in Fluids*, Vol. 13, pp. 369-376, 1992.
- ⁶³ Bryant R. A., Donbar J. M. and Driscoll J. F., "Acetone LIF for flow visualization at temperatures below 300K," *AIAA Paper*, AIAA-1997-0156, 1997.
- ⁶⁴ Thurber M. C., Grisch F., Kirby B. J., Votsmeier M. and Hanson R. K., "Measurements and modeling of acetone laser-induced fluorescence with implications for temperature-imaging diagnostics," *Applied Optics*, Vol. 37 (21), pp. 4963-4978, 1998.
- ⁶⁵ VanLerberghe W. M., Santiago J. C., Dutton J. C. and Lucht R. P., "Mixing of a sonic transverse jet injected into a supersonic flow," *AIAA Journal*, Vol. 38 (3), pp. 470-479, 2000.
- ⁶⁶ Hartfield R. J., Hollo S. D. and McDaniel J. C., "Planar measurement technique for compressible flows using laser-induced iodine fluorescence," *AIAA Journal*, Vol. 31 (3), pp. 483-490, 1993.
- ⁶⁷ O'Byrne S., Danehy P. M. and Cutler A. D., "Dual-pump CARS thermometry and species concentration measurements in a supersonic combustor," *AIAA Paper*, AIAA-2004-0710, 2004.
- ⁶⁸ Cutler A. D., Danehy P. M., O'Byrne S., Rodriguez C. G. and Drummond J. P., "Supersonic combustion experiments for CFD model development and validation," *AIAA Paper*, AIAA-2004-0266, 2004.
- ⁶⁹ Kasal P., Gerlinger P., Walther R., Wolfersdorf J. and Weigand B., "Supersonic combustion: fundamental investigations of aerothermodynamic key problems," *AIAA Paper*, AIAA-2002-5119, 2002.
- ⁷⁰ Owens M. and Segal C., "Development of a hybrid-fuzzy air temperature controller for a supersonic combustion test facility," *Experiments in Fluids*, Vol. 31, no. 1, pp. 26-33, 2001.

BIOGRAPHICAL SKETCH

Amit Thakur was born in 1976, in India. He was raised in Bhilai, a town in central India, known for the steel manufacturing plant located there. In 1994, he enrolled at the Indian Institute of Technology-Kharagpur, considered one of the best engineering colleges in India, and received a Bachelor of Technology in ocean engineering and naval architecture in 1998. Thereafter until 2000, he worked at Zentech in Bombay-India, a company headquartered in Houston-USA and offering engineering consultancy services to the offshore-oil drilling and production industry. In 2000, he enrolled at the University of Iowa, Iowa City-USA, and in 2002 he received a Master of Science in mechanical engineering with specialization in experimental fluid mechanics. In 2003, he enrolled in the PhD program in aerospace engineering at the University of Florida. At the combustion laboratory, he worked on scramjet engines and gained valuable practical experience ranging from setting up, performing and analyzing scientific experiments to writing technical papers and delivering presentations at international conferences. His research interest is in experimental fluid mechanics.